

**THREE PHASE EROSION TESTING AND CFD ANALYSIS OF
A HELICO AXIAL PUMP**

A Dissertation

by

YI CHEN

Submitted to the Office of Graduate and Professional Studies of
Texas A&M University
in partial fulfillment of the requirements for the degree of

DOCTOR OF PHILOSOPHY

Chair of Committee,	Gerald L. Morrison
Committee Members,	Andrea Strzelec
	Je-Chin Han
	Robert E. Randall
Head of Department,	Andreas A. Polycarpou

August 2017

Major Subject: Mechanical Engineering

Copyright 2017 Yi Chen

ABSTRACT

Electrical Submersible Pumping (ESP) has been developed to be an indispensable artificial lifting method in industry due to its high productivity. However, the reliability of an ESP system is a disadvantage when being compared with other approaches.

Erosion is one of the leading factors that causes the reduction of productivity and failure of an ESP system. In order to guarantee the longevity of the system and reduce the cost, it is necessary to perform erosion tests on a new pump before being installed in an oil well.

This study explores the erosion on a Helico-Axial (Poseidon) ESP manufactured by Schlumberger. The erosion test rig was built at Turbomachinery Laboratory at Texas A&M University. A 200-hour erosion test with 0.24% sand concentration by weight has been operating at 3600 RPM with a liquid flow rate of 880 GPM and 20% inlet Gas Volume Fraction (GVF) has been performed. During these 200 hours, 7 performance tests were made to acquire the performance maps of the ESP by varying liquid flow rate (600-1100 GPM) and GVF (0-45%). Meanwhile, the vibration characteristics corresponding to each operating condition were collected simultaneously. After 200 hours, a combined analysis of components wear measurement, performance and vibration are used to investigate the effect of 200 hours of wearing on this pump. In order to evaluate the volume of metal loss by this ESP, 3D scan technology is applied,

allowing comparison of the original and eroded impellers. Furthermore, CFD simulations on both the original and eroded pump geometries are developed in ANSYS-FLUENT to evaluate the performance variation. An erosion model for predicting erosion rate is introduced to the result of simulation and calibrated by the loss of thickness of the impeller that measured.

DEDICATION

For the glory of God

ACKNOWLEDGEMENTS

I wish to express my great respect for my advisor Dr. Gerald Morrison. I appreciate his kindness and patience which encouraged me to explore the unknown. He provided a wonderful place for all of us to learn how to enjoy the work as well as how to enjoy the life.

I also want to express my thanks to Dr. Strzelec, Dr. Delgado, Dr. Han, and Dr. Randall for spending their time and providing helpful advices for my Ph.D. program.

I want to appreciate all the turbolab family including faculty, lab manager, staff, and lab mates, for making me a family member of Turbomachinery Laboratory. Thanks to Ray for training me to drive the forklift and use the machine shop, and giving the biggest tolerance to my dirty sand. Thanks to my partners, Daniel, for being my role model as a perfect project manager and engineer; Sujan, for the great help in CFD meshing and simulation; Abhay, for teaching me how to think as an engineer in a mature way; Dezhi, for teaching me how to work in a team with great diversity; Sahand, for helping me troubleshooting the instrument for signal processing and programming in LabVIEW; Yiming for helping me in the Poseidon ESP project; Changrui, for the help in G400 ESP project and bearing part; Joey, for bring the endless joy and selfless help. I also want to thank to Scott, Klayton, Yintao, Wenfei, Peng, Yong, Nick, Chokote, Ke, Srinivas, Yusuf, Andrew Johnson, Andrew Crisafulli, Chase, Ted, Wenjie, Burak, Bahadir, Craig.

Thank you for giving the advices, helping me with the erosion test, and suffering and enjoying the project together with me.

I want to thank Shell and Chinese Scholarship Council for the sponsorship which supported my research and my life during the Ph.D. program.

I want to thank my dear roommate, Chao-Cheng Shiau, for his encouragement and support in my difficult time and guiding me to solve the problem with more patience and endurance. Thanks to all my friends, brothers and sisters at Grace Bible Mandarin Church for being an important part of my life in United States.

I would like to thank my parents and grandparents for their unfailing love and unconditional support of all my life.

Most importantly, I would like to thank our Lord. Without his guide, I cannot be here, 7000 miles away from my hometown, and complete this program. Without his work, I will not be able to meet with those great persons I mentioned or I did not mention. Without his love, I cannot find my way to the truth and the new life.

CONTRIBUTORS AND FUNDING SOURCES

Contributors

This work was supervised by a dissertation committee consisting of Professor Gerald Morrison [advisor], Dr. Andrea Strzelec, Dr. Adolfo Delgado [substitute for Dr. Andrea Strzelec in the defense], and Dr. Je-Chin Han of the Department of Mechanical Engineering, and Dr. Robert Randall of the Department of Civil Engineering.

The CFD mesh for the new impeller and diffuser in Chapter 4 was provided by Dr. Sujan Reddy. For the experimental test, I was helped by many individuals mentioned in Acknowledgements. All other work conducted for the dissertation was completed by the student independently.

Funding Sources

Graduate study was supported by a teaching assistantship from Texas A&M University.

Graduate study was also supported by a research assistantship from the Texas A&M Engineering Experimental Station, which is from the project sponsored by Shell.

Graduate study was also supported by a scholarship from the Chinese Scholarship Council.

NOMENCLATURE

BHP	Brake Horsepower
BPD	Barrels Per Day
CFD	Computational Fluid Dynamics
ESP	Electrical Submersible Pumps
EF	Erosion Factor
ER	Erosion Rate
FFT	Fast Fourier Transform
GPM	Gallon Per Minute
GVF	Gas Volume Fraction
Head	Equal to pressure rise(Unit: Psi)
NPSHR	Net Positive Suction Head Required
P&ID	Piping and Instrumentation Diagram
Q	Volume Flow Rate
RPM	Rotational speed in revolutions per minute
VFD	Variable Frequency Drive

TABLE OF CONTENTS

	Page
ABSTRACT	ii
DEDICATION	iv
ACKNOWLEDGEMENTS	v
CONTRIBUTORS AND FUNDING SOURCES	vii
NOMENCLATURE.....	viii
TABLE OF CONTENTS	ix
LIST OF FIGURES.....	xi
LIST OF TABLES	xix
1. INTRODUCTION.....	1
1.1 Artificial Lift & ESP	1
1.1.1 Artificial Lift for Oil and Gas	1
1.1.2 What is ESP: ESP Configuration	3
1.2 Literature Review	6
1.2.1 ESP Reliability	6
1.2.2 Erosion Theory.....	10
1.2.3 Erosion Study on Pump.....	21
2. OBJECTIVE	33
3. METHODOLOGY	35
3.1 Experimental Setup	35
3.1.1 Test Rig	35
3.1.2 Poseidon ESP	40
3.1.3 Operating Condition.....	42
3.1.4 Sand Property	42

3.1.5 Performance Measurement.....	45
3.1.6 Vibration Measurement.....	46
3.2 Test Procedure.....	49
3.2.1 Introduction of Comprehensive Performance Test	49
3.2.2 Practical Issues in Data Trueness and the Solutions	50
3.3 Record of Geometry Change.....	51
3.3.1 3D Laser Scanner	51
3.3.2 Image Process.....	54
3.3.3 Impeller Recorded by Camera and 3-D Scanner.....	56
3.4 Numerical Simulation	59
3.4.1 Two Ways to Investigate Erosion	59
3.4.2 Geometry and Mesh for 1 st Stage Performance	60
3.4.3 Time/ Grid Independence Study	63
4. RESULTS AND ANALYSIS	68
4.1 Metal Loss of the Pump	68
4.1.1 Overview of the Wear	68
4.1.2 Contour of Wear on the Impellers: 3D scan.....	71
4.1.3 Tip Clearance Increase	73
4.1.4 Wear of the Leading Edges	78
4.1.5 Weight Loss of Each Stage	79
4.2 Pump Performance Change.....	81
4.2.1 Overview of the ESP Performance Change at Erosion Condition ..	81
4.2.3 Performance Curves Movement in 200 Hours.....	84
4.3 Numerical Simulation on the Pump	94
4.3.1 Performance Map (Single-Phase).....	94
4.3.2 GVF Distribution at the Interfaces (Two-Phase).....	99
4.3.3 Erosion Model for Predicting Erosion Rates (Three-Phase).....	104
4.4 Bearings and Vibration.....	122
4.4.1 Orbits and FFT at Operation Condition	122
4.4.2 Waterfall Plots in RPM Test	129
4.4.3 Bearing Wear.....	134
5. CONCLUSIONS AND SUGGESTIONS.....	138
REFERENCES.....	140
APPENDIX A	147
APPENDIX B	150
APPENDIX C	153

LIST OF FIGURES

	Page
Figure 1: General Types of Artificial Lift Method [2]	2
Figure 2: Conventional ESP System [1].....	4
Figure 3: Artificial Lifting Market in 2010, 2011 and 2012. By Dover [6][7][8]	6
Figure 4: General Conditions and ESP Downhole Failures in Three Reservoirs [11].....	8
Figure 5: Subsystem Failures of ESPs in DZ[46]	9
Figure 6: Schematic of Ideal Cutting [14].....	11
Figure 7: Predicted Variation of Volume Removal with Angle for a Single Abrasive Grain (Solid Line); Experimental Points for Erosion By Different Grains [14]	13
Figure 8: Volume Removal at Difference Impingement Angle(Particle Rotation Considered) [13]	15
Figure 9: Erosion Curves in Brittle and Ductile Erosion Mechanism for Different Impingement Angles [48]	17
Figure 10: Erosion of Copper from Experimental Data Explained by Bitter’s Erosion Model [16].....	17
Figure 11: Particle Paths for Two In-Line Tubes Showing the Effect of the Particle Response Time on Collisions with the Downstream Tube [27].....	20
Figure 12: A Comparison of Particle Paths for Two In-Line Tubes Showing the Effect of Different Values of λ on the Particle Response to the Turbulent Fluctuations [27]	21
Figure 13: Inclined and Perpendicular Impact Testers[41]	23

Figure 14: Erosion Rate Contours for the Impeller and Diffuser Shroud for Different Size Particles (27 μm , 60 μm) [41]	23
Figure 15: Streamwise Erosion Rates for the Impeller Using Different Coating Materials Which Are Calculated by CFD[41]	24
Figure 16: Erosion Rates for the Diffuser Using Different Coating Materials Which Are Calculated by CFD [41].....	24
Figure 17: Original (Red) and Eroded (Green) Impeller and Profiles of Them in Best Fit [30]	25
Figure 18: Key Erosion Parameters for Initial (Upper) and Eroded (Lower) Impeller's Leading Edge(left) and Trailing Edge(right) [30].....	26
Figure 19: PP1 Shaft Waterfall at 117 and 185 Hours [36]	28
Figure 20: Pump Performance Curve with Pure Water at 0-117-185 Hours [36]	28
Figure 21: Performance Degradation with Pure Water [36]	29
Figure 22: Wear Marks on Different Stages [36].....	29
Figure 23: Scoring Wear and Hair Crack [36]	30
Figure 24: Erosion Rate for the Computed Erosion Factor Values[32]	31
Figure 25: Comparison between the Computed Erosion Rates with the Eroded Locations in the First 2 Impellers [32]	32
Figure 26: Experimental Setup Diagram.[37]	35
Figure 27: P&ID for Poseidon ESP Erosion Test Rig	37
Figure 28: Erosion Loop Indoor Parts.....	38
Figure 29: Poseidon Pump Installed in a Derrick(SolidWorks).....	39
Figure 30: Impeller of Poseidon ESP	40
Figure 31: Diffuser of Poseidon ESP	40

Figure 32: Sectional View of a Stage of Poseidon ESP[43]	41
Figure 33: Journal of the Poseidon ESP	41
Figure 34: Sand Analysis(size distribution)	43
Figure 35: Microscopic View of New Sand.....	44
Figure 36: Operating Interface, Test Rig Control and Performance Data Capturing	45
Figure 37: Monitor Interface, Vibration Data Capturing.	46
Figure 38: Proximity Probes Location at 1st Diffuser	47
Figure 39: Locations of Proximity Probe(red) and Pressure Sensor(green) at 1st Diffuser (Solidworks)	47
Figure 40: Schematic View of the Vibration Measuring Locations.....	48
Figure 41: Comprehensive Performance Tests Scheduled During Erosion Test.	50
Figure 42: Instrument for 3D Scan.....	52
Figure 43: NDI PRO CMM Model 1000	53
Figure 44: NDI ScanTRAK.....	53
Figure 45: 3-D Scan Interface in Geomagic Studio (1 st eroded impeller, points).....	54
Figure 46: Preliminary Processed Image of the Original Impeller(polygons).	54
Figure 47: Preliminary Processed Image of 1 st Eroded Impeller(polygons)	55
Figure 48: Finally Processed Image of 1 st Eroded Impeller(surfaces)	55
Figure 49: 1 st Impeller(Eroded and Original) Captured by Camera(left) and 3-D Scanner(right).....	57
Figure 50: Comparison of Original and Eroded Impellers When Aligned Together	58

Figure 51: Geometry and Mesh of Original Impeller of the Pump[43]	60
Figure 52: Geometry and Mesh of Original Diffuser of Poseidon Pump [43]	60
Figure 53: Geometry and Mesh of Eroded Impeller of 1st Stage	61
Figure 54: Geometry of Eroded Impeller of 1 st Stage-Sectional View	62
Figure 55: Geometry of Eroded Impeller of 1 st Stage-Detail of the Tip Clearance	62
Figure 56: Torque Ratio in Time Independence Study	64
Figure 57: Head ratio in Time Independence Study, Logarithmic Scale in X-Axis	65
Figure 58: Torque Ratio in Grid Independence Study	67
Figure 59: Head Ratio in Grid Independence Study	67
Figure 60: New and Eroded Diffuser of the 1 st Stage	68
Figure 61: New and Eroded Diffuser of the 2 nd Stage	69
Figure 62: New and Eroded Impellers of the 1 st Stage (Left) and 2 nd Stage(Right)	70
Figure 63: Surface Distance between New and Eroded Impeller 1 (Unit: inch).....	71
Figure 64: Surface Distance between New and Eroded Impeller 2 (Unit: inch).....	72
Figure 65: Boundary Dividing Wear Area on the Blade Tip of Impeller 1 (Unit: inch)	73
Figure 66: Measurement of the Wear on the Aligned Impeller Profile.....	74
Figure 67: Measurement of the Wear on the Aligned Impellers.....	74
Figure 68: Measurement of the Thickness of Impeller Housing.....	75
Figure 69: Sectional View of the 1 st Stage Assembled	76

Figure 70: Measurement of the Wear at the Blade Tip and Impeller Housing	77
Figure 71: Distance between Leading Edges of the New and Eroded Impellers.....	78
Figure 72: Weight Loss of Each Impeller Housing.....	79
Figure 73: Weight Loss of Each Impeller	80
Figure 74: Weight Loss of Each Diffuser	80
Figure 75: Static Pressure Measured at Different Location during the 200-Hour Test.....	82
Figure 76: Pressure Rise of Each Stage during the 200-Hour Test.....	83
Figure 77: Normalized Pressure Rise during the 200-Hour Test	84
Figure 78: Total Pressure Rise at the 0 th and 200 th Hour	85
Figure 79: ESP Efficiency at the 0 th and 200 th Hour.....	86
Figure 80: 1 st Stage Pressure Rise at the 0 th and 200 th Hour	86
Figure 81: 2 nd Stage Pressure Rise at the 0 th and 200 th Hour	87
Figure 82: 3 rd Stage Pressure Rise at 0 th and 200 th Hour.....	87
Figure 83: Performance Map, 1 st Stage Pressure Rise Ratio at the 200 th Hour.....	89
Figure 84: Performance Map, 2 nd Stage Pressure Rise Ratio at the 200 th Hour.....	89
Figure 85: Performance Map, 3 rd Stage Pressure Rise Ratio at the 200 th Hour.....	90
Figure 86: Performance Map, Efficiency Ratio at the 200 th Hour	90
Figure 87: Performance Curves of the Head at 1 st Stage Every 50 Hours.	92
Figure 88: Performance Curves of the Head at 2 nd Stage Every 50 Hours.	92

Figure 89: Performance Curves of the Head at 3 rd Stage Every 50 Hours.....	93
Figure 90: Grid for 1 st Stage Performance Simulation.....	95
Figure 91: Comparison of the Head-Q Curves for the 1 st Stage	96
Figure 92: Schematic View of the Axial Location on the 1 st Stage	97
Figure 93: Axial Pressure Distribution in the New and Eroded Pump in CFD Simulation.....	98
Figure 94: Axial Pressure Loss in the New and Eroded Pump in CFD Simulation	98
Figure 95: Front View of the Whole Geometry	99
Figure 96: Mesh of the 1 st Stage with the Bottom Tee Connected	100
Figure 97: GVF Distribution at Certain Cross-Sections, 20% GVF Inlet.....	101
Figure 98: Blade to Blade Pressure Distribution of 2 nd Impeller at Span=0.98.....	103
Figure 99: Blade Loading of 2 nd Impeller for Pressure at Span=0.98.....	104
Figure 100: Grid for the 3-Phase Simulation Inspecting the 2 nd Impeller	105
Figure 101: Points at the Leading Edge of Impeller Picked for Calibration (exclude two ends)	108
Figure 102: Contours of the Impact Angle (unit: degree), 120-Degree Averaged	109
Figure 103: Contours of the Impact Angle Function, 120-Degree Averaged	109
Figure 104: Contours of the Impact Velocity, 120-Degree Averaged	110
Figure 105: Contours of the Sand Flush Rate, 120-Degree Averaged (Logarithmic Scale).....	110
Figure 106: Calibration for the Erosion Model from 40-Degree Averaged Simulation	111

Figure 107: Calibration for the Erosion Model from 80-Degree Averaged Simulation	112
Figure 108: Calibration for the Erosion Model from 120-Degree Averaged Simulation.....	112
Figure 109: Erosion Rate near 2 nd Impeller Inlet, Logarithmic Scale (unit, mm/s).....	114
Figure 110: Erosion Rate near 2 nd Impeller Inlet, Linear Scale (Unit, mm/s).....	114
Figure 111: Wear on near the 2 nd Impeller for 200 Hours, Linear Scale (Unit, mm).....	115
Figure 112: Eroded 1 st Diffuser and Eroded 2 nd Impeller	116
Figure 113: Water Streamline in 3-Phase Simulation without 1 st Imp	117
Figure 114: Water Streamline in 2-Phase Simulation with 1 st Imp.....	118
Figure 115: Orbit at the 1 st Diffuser	122
Figure 116: Orbit at the 2 nd Diffuser	123
Figure 117: Orbit at the 3 rd Diffuser.....	124
Figure 118: Orbits after FFT for the 1 st Diffuser	126
Figure 119: Orbits after FFT for the 2 nd Diffuser.....	127
Figure 120: Orbits after FFT for the 3 rd Diffuser	128
Figure 121: Waterfall of the Orbits at 1 st Diffuser (0th, 25th hour).....	131
Figure 122: Waterfall of the Orbits at 1 st Diffuser (50th, 100th hour).....	132
Figure 123: Waterfall of the Orbits at 1 st Diffuser (150th, 200th hour).....	133
Figure 124: Measurement of the Bushing and Journal Bearing.....	134
Figure 125: New and Eroded Journal Bearings	135

Figure 126: Weight Loss and Diameter Reduction of Journal Bearings.....	137
Figure 127: 1 st Diffuser Comparison, Left: New, Right: Eroded.....	147
Figure 128: 2 nd Diffuser Comparison, Left: New, Right: Eroded.....	148
Figure 129: 3 rd Diffuser Comparison, Left: New, Right: Eroded	148
Figure 130: 4 th Diffuser Comparison, Left: New, Right: Eroded.....	149
Figure 131: Pressure Rise of Each Stage without Modification or Correction.....	154
Figure 132: GVF at the Pump Inlet in 200-Hour	155
Figure 133: Performance Maps at 20% GVF Inlet (Left: Multi-Phase Test Rig; Right: Erosion Test Rig).....	155
Figure 134: Performance Maps at 0% GVF Inlet (Left: Multi-Phase Test Rig; Right: Erosion Test Rig).....	156
Figure 135: Pressure Rise of Each Stage after Correction and Modification	157

LIST OF TABLES

	Page
Table 1: Identification for Items in Figure 26[37]	36
Table 2: ErosionTest Operating Conditions	42
Table 3: Sand Properties	43
Table 4: Performance Test Matrix	49
Table 5: Time Step Independence Study	64
Table 6: Grid Independence Study	66
Table 7: CFD Boundary Condition for Single-Phase Simulations	94
Table 8: Parameters Setting and Model Selection for 2-Phase Simulation	101
Table 9: Boundary Conditions and Other Parameters for 3-phase Simulation	106
Table 10: Coefficients from Least Square Regression Analysis	113
Table 11: Details of the Models for Pump Erosion in Different Studies.	121
Table 12: Microscopic View of the Journal Bearing at the 1 st Diffuser	136

1. INTRODUCTION

1.1 Artificial Lift & ESP

1.1.1 Artificial Lift for Oil and Gas

In the oil and gas industry, if the bottomhole pressure of a well is enough to overcome the total pressure difference and pressure loss along the flowpath and naturally push the oil to the ground, we call it “flowing well”, otherwise, it is “dead well”. The bottomhole pressure of an oil well drops due to the reduction of liquid in the reservoir underground. Hence, the flow rate of the oil will gradually decrease to zero, and finally, the flowing well becomes to be a dead well. In this case, artificial lift is applied to prolong the life and improve the productivity of the oil well by rising the bottomhole pressure or reducing the pressure difference and pressure loss.

According to Gabor Takacs[1], gas lifting and pumping are the main methods of artificial lift in oil and gas industry.

Gas lifting (**Figure 1, 4**) can be divided into the intermittent-flow gas lift and the continuous-flow gas lift. For intermittent-flow gas lift, gas is periodically injected into the tubing string whenever a sufficient length of liquid has accumulated at the pipe bottom. A high-speed gas injection below the liquid column will rise the bottom hole pressure immediately and push the column as a slug to the ground. On the other hand,

continuous-flow gas lift uses high-pressure natural gas injected into the well stream at downhole point to aerate the liquid and reduce the pressure difference and pressure losses along the flow path.

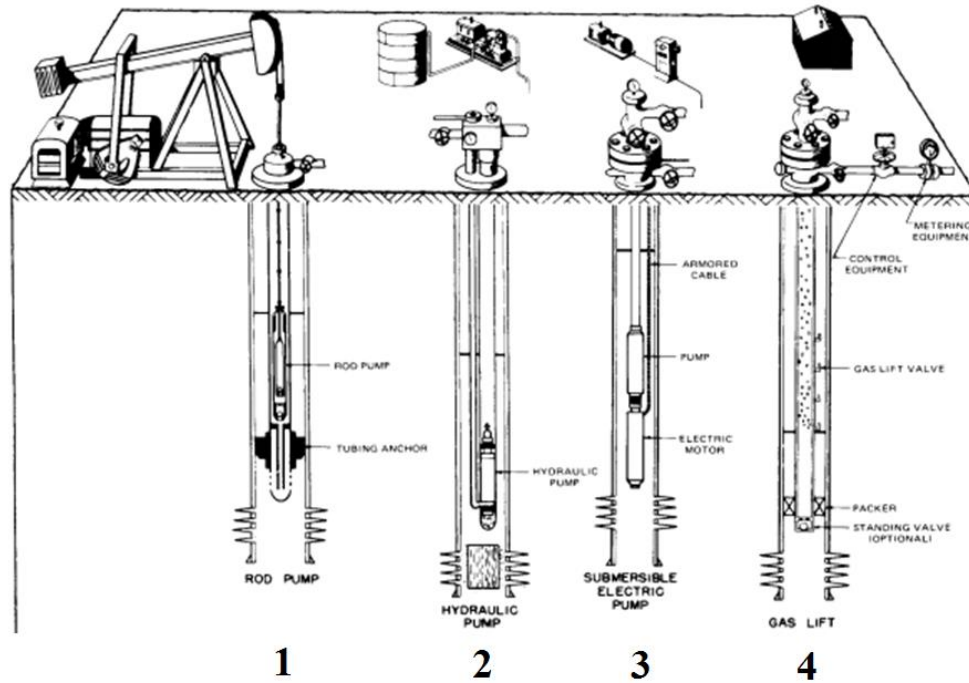


Figure 1: General Types of Artificial Lift Method [2]

Pumping includes rod pumping and rodless pumping. Both types lift liquid by increasing the bottomhole pressure. The rod pump method (**Figure 1, 1**), as the name implies, utilizes a rod string to transport mechanical energy and rise the liquid. For a rodless pump, electric or hydraulic energy is transported to drive the submersible pump. ESP (**Figure 1, 3**) and hydraulic pumps (**Figure 1, 2**) are the two main divisions. Typically,

an ESP is driven by an electrical motor at the bottom hole which is powered by electricity; while a hydraulic pump is driven by pressurized hydraulic fluid injected from the surface.

1.1.2 What is ESP: ESP Configuration

The electrical submersible pumping was invented and developed by Armais Arutunoff in the late 1910s in Russia. The first ESP installation was successfully operated in the El Dorado field in Kansas in 1926.[1]

A systemic view of a standard ESP system with its key components is provided by

Figure 2. The electrical cable connects the power supply on the surface with the electrical motor underground. A protector is installed between motor and pump to absorb the thrust created by the pump. A gas separator will sometimes be added to prevent most of the gas from entering the pump inlet. Most of the components of the system are submerged in the fluid to be pumped and they are cooled by the fluid as well.

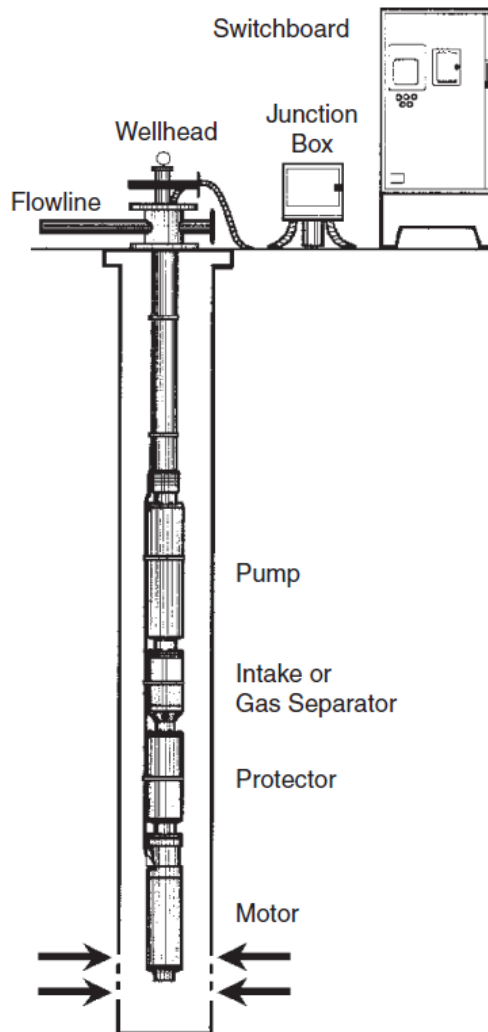


Figure 2: Conventional ESP System [1]

According to Gabor Takacs[1], advantages of using ESP units can be summarized as follows[3][4][5]:

- High productivity from medium depths
- Relatively high energy efficiency (around 50%) for systems producing over 1,000 bpd
- Capable to be deployed and be functional in deviated wells

- Proper installation may allow low maintenance of the ESP system
- Limited surface occupation makes it applicable in urban locations
- Low space requirements make it well suited to the offshore environment
- Corrosion and scale treatments are relatively easy to perform

Disadvantages are listed below:

- A reliable electric power of high voltage is required
- To achieve flexibility of an ESP system operation, a variable speed drive is required
- With a low flexibility, installation design is crucial
- To improve the reliability, costly abrasion-resistant materials are required for an ESP pumping fluid with sand
- Difficulties in repairing the ESP equipment
- High well temperature might require special material for building the ESP system
- Cable suspended or coiled tubing deployed ESP units are required to reduce running and pulling costs

Briefly, the high installation cost and reliability problem caused by the extreme working environment are the two main shortages which have limited the development of the ESP. However, because of its high productivity and limited maintenance requirement, the ESP has a significant presence in the artificial lift market. **Figure 3** is provided by Dover which shows the market shares of all types of artificial lift methods in the world. With the expansion of the market from 2010 to 2012, the ESP had half of the market.

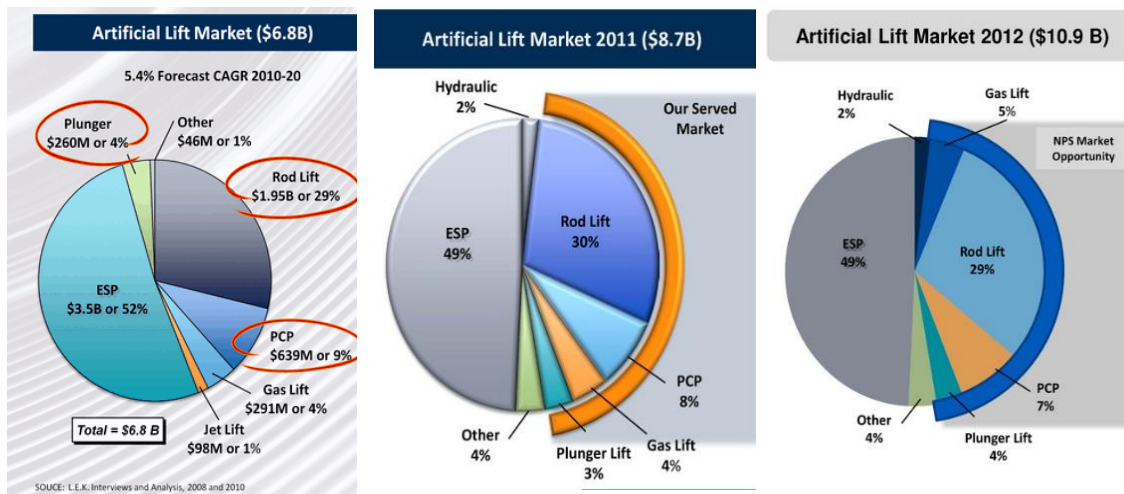


Figure 3: Artificial Lifting Market in 2010, 2011 and 2012. By Dover [6][7][8]

1.2 Literature Review

1.2.1 ESP Reliability

Considering the huge economical profits of the ESP in the global market, to improve the quality and prolong the longevity of an ESP system is very desirable. However, ESP technology was not widely used at its early age, thus, practical examples were not sufficient for analysis until the end of the last century.

Regarding the high cost of ESP installation, Toole and Brien initiated a test program [9] in 1984 which finally resulted in an extensive reduction of ESP failures. They indicated the necessity of pump testing before application to eliminate a defective pump and guarantee the quality of the new pump. Although slight wear on a ESP might be

acceptable by criteria of manufacturer, it will reduce the productive life of the part, so they also insisted that only brand new ESP can be accepted.

However, Divine, Lannom and Johnson (1992) [10] had a different view. They investigated the head, BHP (Brake Horsepower), Efficiency deviation of the ESP to judge if it can be reused, and assumed the used pump can stand long under proper operation. In addition, they elucidated the reason for upthrust and downthrust wear related to best efficiency point (BEP).

Upchurch (1991) [11] analyzed 1149 ESPs' down-hole pumping equipment failures in the East Wilmington Field of California. The main reasons for failure differed case by case. According to the different working environments in 3 zones, he exhibited failures in 12 categories which are shown in **Figure 4** (4 pumping rates for 3 zones). Failures of cable, pothead, pump, motor and seal were identified as 5 major downhole failures. He indicated that higher temperature, bad cooling and particles are the main reasons for such component failures.

GENERAL DESCRIPTION	RANGER TERMINAL U.P.FORD		
	Unconsolidated Sandstone	Poorly Consolidated Sandstone	Moderately Consolidated Sandstone
OIL GRAVITY (°API)	15	20	28
GAS-OIL RATIO (scf/bbl)	175	250	395
AVE. PRESSURE (psi)	1000	1100	1400
AVE. TEMPERATURE (°F)	130	160	210
AVE. WATER CUT (%)	90	73	78

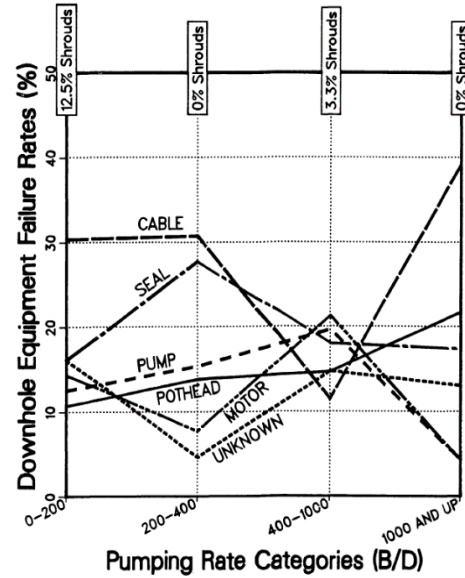
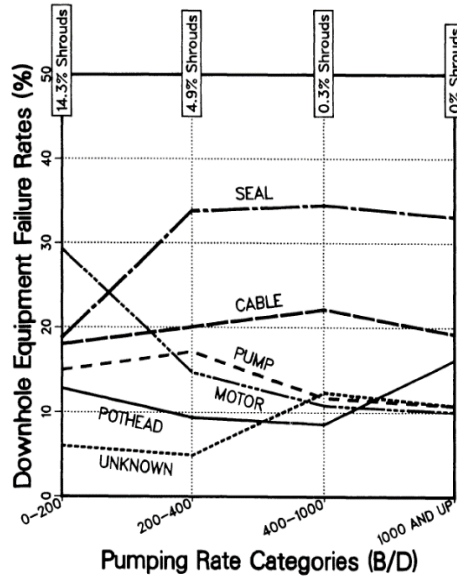
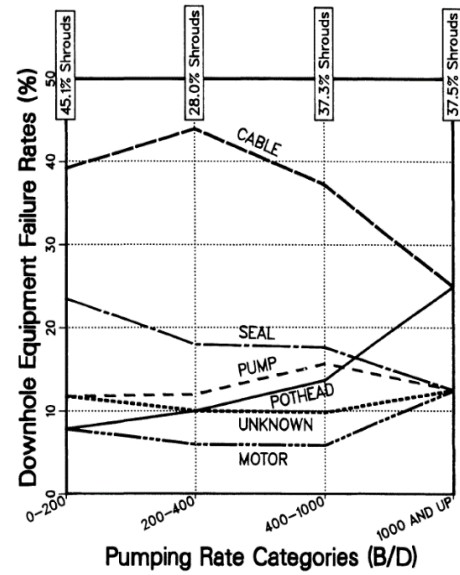


Figure 4: General Conditions and ESP Downhole Failures in Three Reservoirs [11]

Hisham, Farooq and Mehmet (2003)[46] analyzed 501 ESPs which were installed in Divided Zone Kuwait-Saudi Arabia during 1998-2001. **Figure 5** shows the percentage of failed components. Failures of motor, pump, and cable contribute to the primary subsystem failures.

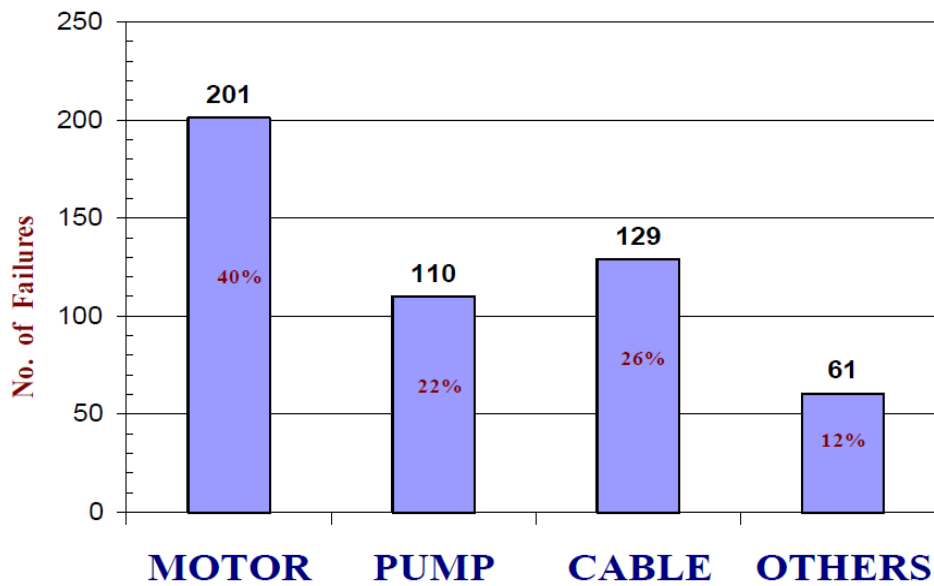


Figure 5: Subsystem Failures of ESPs in DZ[46]

In both studies above, classification of component failures, operating conditions or ESP manufacture are not exactly the same. This makes the percentage of each type of failure differing case by case. However, erosion is always a key factor that directly affects the pump performance and contributes to the failure of an ESP. In addition, the high cost of an ESP installation requires engineers to be very cautious when selecting a pump. Hence, conducting an erosion study on the turbine pump before it is installed in an

abrasive environment can help us to estimate its reliability and guarantee the longevity of an ESP system.

1.2.2 Erosion Theory

According to Finnie[14] and Bitter[15], the earliest studies of erosion originated in Germany. De Haller (1939) [18] observed eroded surfaces under a microscope and found 2 kinds of erosion: one at large impingement angles which causes flattened and highly deformed surface, the other at small impact angles which causes scratched and a less-deformed surface [15]. Holtey (1939)[19] attributed the wear of metal to two phenomena, "shock" wear and "rub" wear. He suggested that soft steel is more resistant to the "shock" condition, while hard steel is better for the "rub" condition. However, he did not elaborate on the influence of material physical properties nor provide any explanation of the material removal mechanism [14]. Wellinger (1949) [17] seemed to be the first person to gather test data under a wide variety of controlled conditions. He carried out multiple erosion tests with different impingement angles on both hard, brittle steel and soft, ductile steel. Through reactions of different material to all range angles, he concluded that not only the impingement angle but also the eroded material properties will determine what type of erosion dominates [15].

Before Finnie, erosion studies mainly relied on practical examples. Most of them were limited by incomplete experiment data, which reduced their ability to predict erosion. In other words, the root problem of erosion had rarely been explored. Finnie's study (1960)

[14] emphasizes learning the fundamentals of the erosion mechanism. Regarding completely different erosion mechanism of different material, he limited the discussion of the sample materials to 2 categories, ductile material and brittle material. One of his significant contributions is the first ductile cutting model for a single particle, which sets the basic pattern for all the single particle erosion models. For his cutting model, he illustrated an ideal erosion process (**Figure 6**). To simplify this process, several assumptions were made: the single particle removes material in mostly the same way as a machine tool does; the surface material deforms plastically; the particle should be much harder than the surface and does not fracture; it has little rotation; displaced volume is equal to the volume removed, contact width and length are much bigger than cutting depth.

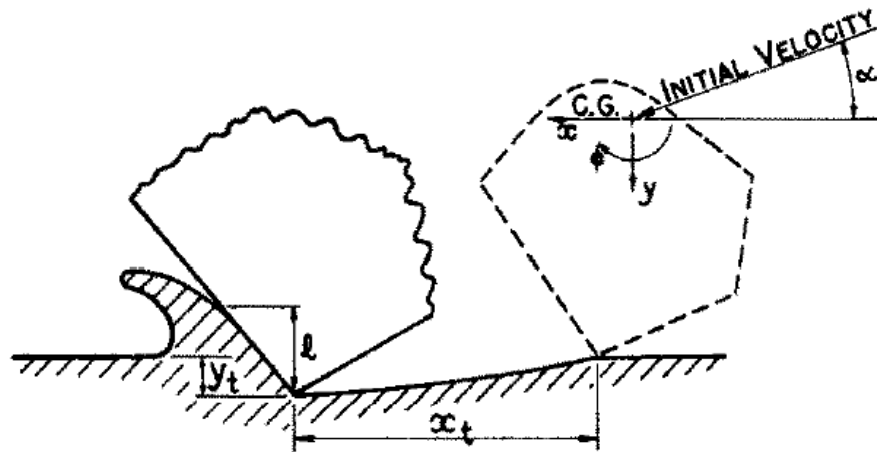


Figure 6: Schematic of Ideal Cutting [14]

The expressions for the cutting process obtained by Finnie are as follows:

$$Q_{ab} = \frac{mV^2}{p\psi K_{cf}} \left(\sin 2\alpha - \frac{6}{K_{cf}} \sin^2 \alpha \right), \tan \alpha \leq \frac{K_{cf}}{6} \quad (1)$$

$$Q_{ab} = \frac{mV^2}{p\psi K_{cf}} \left(\frac{K_{cf}}{6} \cos^2 \alpha \right), \tan \alpha \geq \frac{K_{cf}}{6} \quad (2)$$

$$\psi = \frac{l}{y_t} \quad (3)$$

Q_{ab} is the volume of material removed by a single abrasive of mass, m , velocity, V , and impingement angle, α . K_{cf} is the ratio of the vertical force of the particle to the horizontal force (Cutting Friction). According to his experimental result [12], he assumed that $K_{cf} = 2$ is reasonable. p is the horizontal component of flow pressure. l is the contact area (length), x_t and y_t are the cutting length and depth. Referring to metal cutting experiment [20], $\psi = 2$ is selected.

Two situations are considered to determine when the cutting ceases. If $\tan \alpha \leq \frac{K_{cf}}{6}$, particle will not stop cutting until it leaves the surface. While for $\tan \alpha \geq \frac{K_{cf}}{6}$, cutting will stop when horizontal motion of the particle ceases (before the particle leaves the surface).

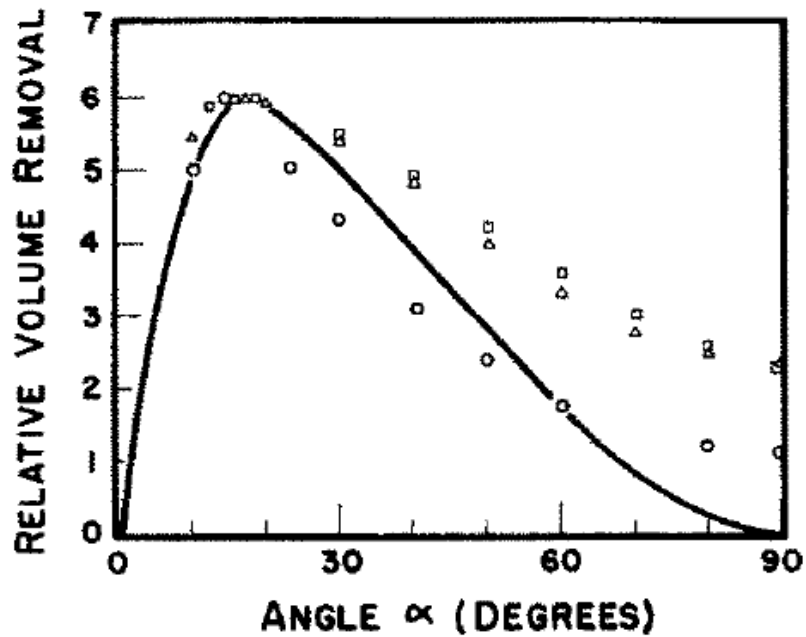


Figure 7: Predicted Variation of Volume Removal with Angle for a Single Abrasive Grain (Solid Line); Experimental Points for Erosion By Different Grains [14]

Regarding the curve given by the model and his experiment data(**Figure 7**), they collapse at lower angles. However, for higher angles, the discrepancy is greater. Especially for the perpendicular case, the model predicts no erosion, while actually erosion exists. Later, Finnie modified his first model by considering the rotation of the particle [13]. He added an extra assumption that there was no particle rotation at the beginning, but during cutting, the horizontal force on the cutting tip will rotate the particle. Equations (4) and (5) include this effect:

$$Q = \frac{c_i m V^2}{4p \left(1 + \frac{mr^2}{I}\right)} \frac{2}{P} \left(\sin 2\alpha - 2 \frac{\sin^2 \alpha}{P} \right), \quad y_t = 0 \quad (4)$$

$$Q = \frac{c_i m V^2}{4p \left(1 + \frac{mr^2}{I}\right)} (\cos^2 \alpha), \quad \dot{x}_t' = 0 \quad (5)$$

$$P = K_{cf} / (1 + mr^2/I) \quad (6)$$

$$\dot{x}_t' = U \cos \alpha - \frac{2U}{P} \sin \alpha \quad (7)$$

c_i : fraction of particles cutting in idealized manner,

I : moment of inertia of particle about its center of gravity,

r : average particle radius,

\dot{x}_t' : horizontal velocity of tip of particle when the cutting ceases.

He claimed that the model will have a better prediction at higher angles if considering the initial angular speed of the particle. Although the curves in **Figure 8** seem more reasonable, this model still does not capture the key point. One basic reason is that his ideal cutting assumptions are not applicable to erosion at big impingement angles.

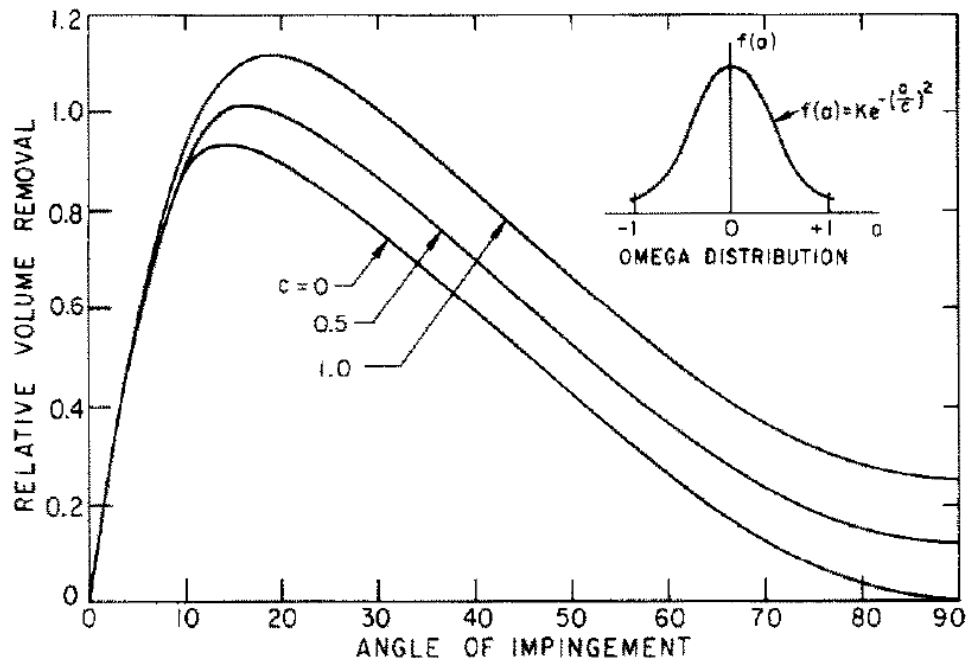


Figure 8: Volume Removal at Difference Impingement Angle(Particle Rotation Considered) [13]

Being inspired by De Haller (1939) [18] and R. Wellinger(1949) [17], Bitter (1962) considered two main contributions of erosion, cutting and deforming in order to extend Finnie’s single particle erosion model. Cutting wear (W_c) is “more likely” to happen when a particle impacts on ductile material surface with a larger horizontal momentum, while deformation wear (W_d) is “more likely” to happen when a particle impacts on brittle material surface with a larger vertical momentum which is regarded as fatigue damage from plastic deformation. **Figure 9** illustrates these 2 types of wear and their corresponding erosion curves. In his model for cutting (W_c) which is expressed in Equation (7)(8), like Finnie, 2 ranges of impact angles are divided by α_0 . In his erosion

model for deformation (W_d) which is expressed in Equation (9), he introduced the threshold velocity, V_T , and the deformation wear factor, ε . Deformation will not happen if the normal velocity of particle is not larger than V_T . ε is related to the amount of energy required to remove a unit volume of material. With the superposition of these two kinds of wear, the erosion model agrees well with his experiment on cooper erosion, even at bigger impact angles (**Figure 10**). [15][16]

$$W = W_c + W_d \quad (8)$$

$$W_d = \frac{0.5M\Delta V^2}{\varepsilon} \quad (9)$$

$$W_c = \frac{2MC\Delta V^2 \left\{ V \cos \alpha - \frac{Cf\Delta V^2}{\sqrt{V \sin \alpha}} \right\}}{\sqrt{V \sin \alpha}}, \quad \alpha < \alpha_0 \quad (10)$$

$$W_c = \frac{0.5M\{V^2 \cos^2 \alpha - K_1\Delta V^{1.5}\}}{f}, \quad \alpha \geq \alpha_0 \quad (11)$$

$$\Delta V = V \sin \alpha - V_T \quad (12)$$

$$K_1 = 0.82y^2 \sqrt[4]{\frac{y_e}{\rho} \left(\frac{I - q_1^2}{E_1} + \frac{I - q_2^2}{E_2} \right)^2} \quad (13)$$

$$C = \frac{0.288}{y_e} \sqrt[4]{\frac{y_e}{\rho}} \quad (14)$$

f : Cutting Wear Factor

ρ : Density

y_e : Elastic Load Limit

M : Mass of solid impacted on wall

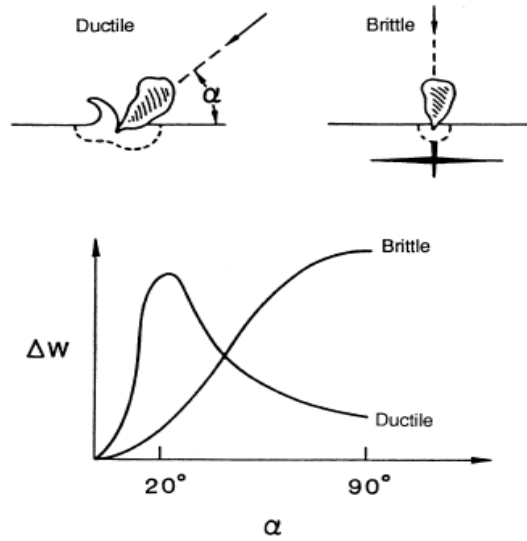


Figure 9: Erosion Curves in Brittle and Ductile Erosion Mechanism for Different Impingement Angles [48]

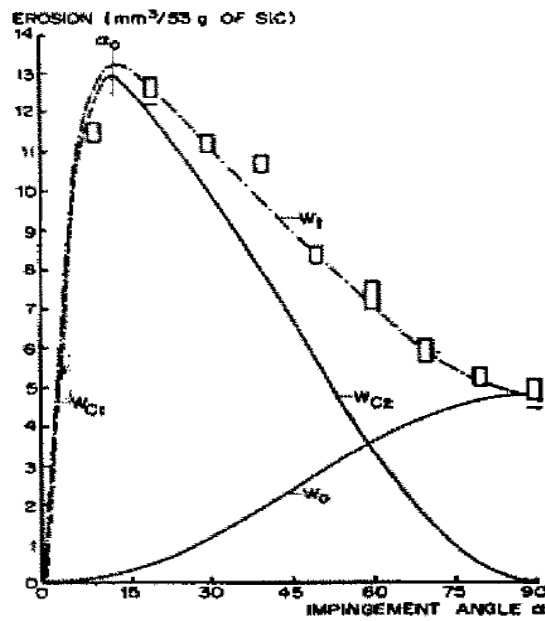


Figure 10: Erosion of Copper from Experimental Data Explained by Bitter's Erosion Model [16]

To simplify the intricate model of Bitter, Neilson, and Gilchrist(1968)[21] postulated a simpler cutting model (W_c) and retained the deformation model (W_d). The modified expressions are shown in equation (15)(16). φ is a cutting wear constant, and n is a constant relate to α_0 .

$$W_c = \frac{MV^2 \cos^2 \alpha \sin n\alpha}{2\varphi}, \quad \alpha < \frac{\pi}{2n} = \alpha_0 \quad (15)$$

$$W_c = \frac{MV^2 \cos^2 \alpha}{2\varphi}, \quad \alpha \geq \frac{\pi}{2n} = \alpha_0 \quad (16)$$

Many erosion models have been developed by different researchers after Finnie and Bitter. The general expression of erosion model is developed empirically as $E_R = c\dot{m}V^n f(\alpha)$. [22] Impact particle mass rate \dot{m} , impact velocity V , impact angle α are the three most commonly considered parameters to affect erosion. Sometimes it might consider the particle diameter, sharpness, materials, and other factors which can be coupled in the coefficient c or represented in the impact angle function $f(\alpha)$. This type of empirical equations is developed from the fundamental mechanism that described by Finnie and Bitter. It has a more accurate prediction for erosion rate and a simpler expression. Therefore, it is adopted by ANSYS-FLUENT in erosion prediction [28]. Tests were also conducted to design erosion resistance equipment. True and Weiner (1976) [31] conducted several tests which were consisted of injecting varying amounts of sand into a compressed air stream flowing at several velocities. They evaluated the effect of flow stream velocity, sand concentration, coating materials and geometry of tested piping (fitting, tee, elbow, and plate) upon the erosion. Regarding their

conclusion, some suggestions were made to optimizing the design of erosion resistant equipment, for example, the velocity reducing chamber and the bull-plugged field tee. Numerical method was developed after computer became accessible, which gradually became a widely applied method which expanded the traditional empirical method for erosion prediction.

Hussei and Tabakoff [25] started the research on the erosion of turbomachines in 1971. They built a special subsonic cascade wind tunnel to analyze the trajectories and velocities of solid particles suspended by air. In 1975, Grant and Tabakoff [24] developed a code to predict 2-D erosion resulting from particles ingested into that wind tunnel using a Monte Carlo simulation. This 2-D model predicts the quantity of material loss from the blades of a turbomachine as well as the erosion location on these blades. Later, Hamed (1982) [34] investigated the particle trajectories for the inlet flow field of a helicopter engine with swirling vanes and particle separator. By using Katsansis and McNally's program (1977) [26], he developed a numerical method for this 3-D erosion problem. Schuh and Humphrey(1990) [27] [33] claimed that most of the study on erosion paid little attention to clarifying the influence of turbulent flow. To predict the wear by particle impact, they stated the significance of the erosion model derived in material science as well as the fluid turbulent model, both of which deliver the liquid-solid interaction. They introduced a momentum equilibration constant, λ , which represents non-dimensional particle response time. Flow simulations were conducted in both turbulence flow and laminar flow to plot trajectories of particles in the particle-

laden flow over 2 in-line tubes for different value of λ (0.1, 0.5 and 10). **Figure 11** and **Figure 12** show an obvious discrepancy in trajectories for $\lambda=0.1$.

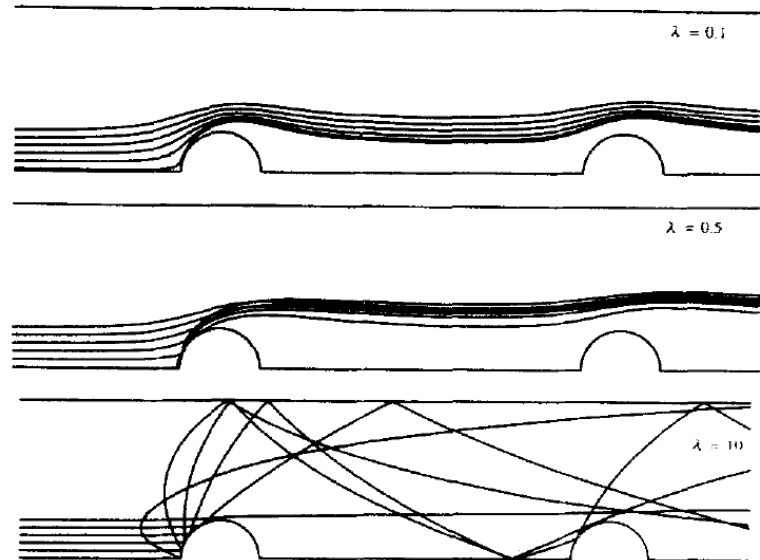


Figure 11: Particle Paths for Two In-Line Tubes Showing the Effect of the Particle Response Time on Collisions with the Downstream Tube [27]

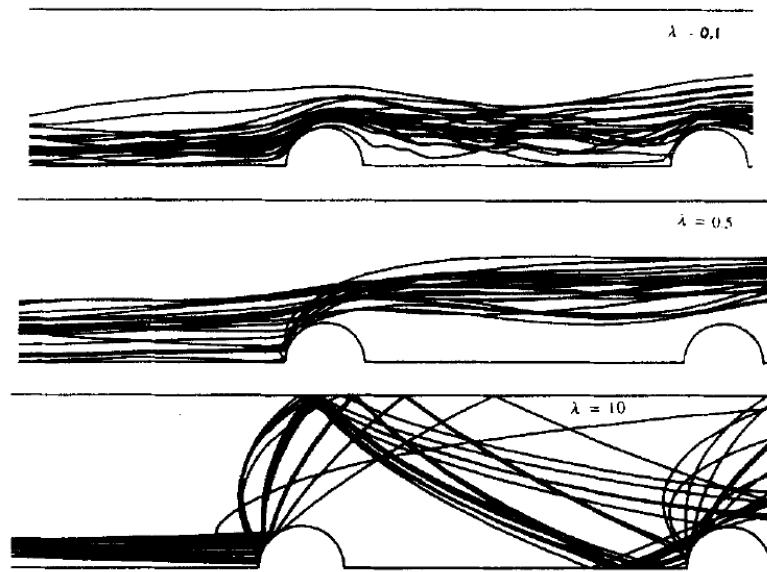


Figure 12: A Comparison of Particle Paths for Two In-Line Tubes Showing the Effect of Different Values of λ on the Particle Response to the Turbulent Fluctuations [27]

Minemura and Uchiyama (1990) [39] developed a 3-D simulation for an inviscid liquid-solid flow in a flow path of a centrifugal pump impeller. The particle diameter varies from 1 mm to 5 mm. Forder, Thew and Harrison (1998) [35] embedded FORTRAN routines in CFX which allowed them to calculate and display the impact angle, velocity and turbulent intensity with the corresponding location on oilfield control valves.

1.2.3 Erosion Study on Pump

Erosion in a pump is quite different with that in a fluidized bed, plate, elbow or any other fixed surface with simple geometry. In addition, centrifugal force is basically a leading

factor of erosion in most pumps, but experiments on fluidized bed or valve cannot simulate this force. Regarding the complicated working condition in an oil well and narrow application of ESP at its early age, to improve the reliability of an ESP in an abrasive working condition was limited to utilizing wearing resistance material and coating technology only. Methods of erosion study on ESP were limited to brief experiments on a slurry pump and the practical data in the field, some of which have been mentioned above. On the other hand, the evolvement of computation power made it possible to perform 3D simulation on the multiphase flow in a rotor machine. In the last two decades, commercial software started to play an important role in CFD analysis. In the study of Stavros, Nicolas, Antonios and Kristis (2009)[41], experimental procedures include nano-indentation, impact tests and 3D surface topography were used to evaluate the erosion factor of 6 types of coating. **Figure 13** shows the experimental setup which can perform erosion test by varying impact angle. Furthermore, CFD analysis incorporating Finnie's erosion model was used to predict the erosion rate of a submersible pump. By introducing an erosion factor, k , which was acquired in the erosion tests, they obtained 6 erosion rates corresponding to different coating. **Figure 15** and **Figure 16** give the streamwise erosion rates of a pump with 6 types of coating. **Figure 14** gives the erosion rate contours on a pump with different sized particles according to their simulation. However, the particle diameter in experiment was 5 mm, while in CFD analysis, it was no more than 0.6mm. Such discrepancy of particle size has weakened the correlation between experiment and simulation.

Impact Tester

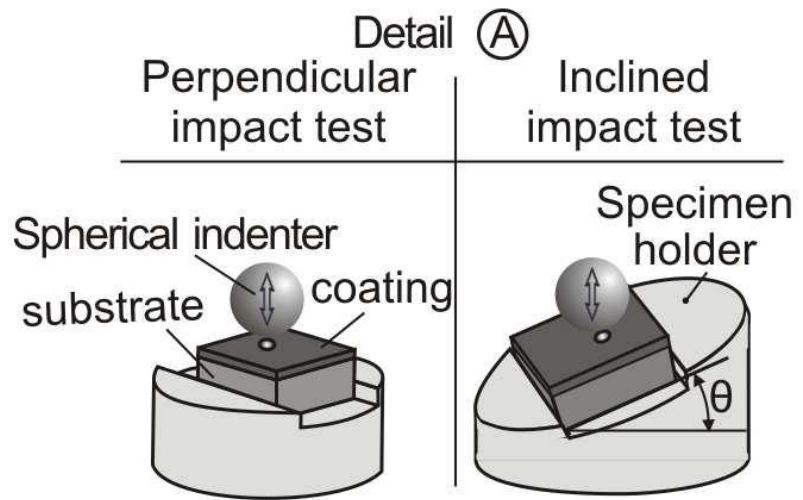


Figure 13: Inclined and Perpendicular Impact Testers[41]

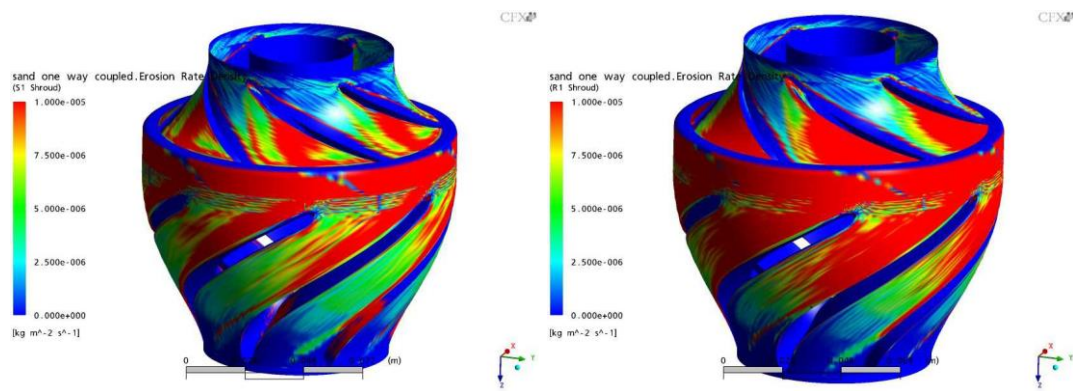


Figure 14: Erosion Rate Contours for the Impeller and Diffuser Shroud for Different Size Particles (27 μm , 60 μm) [41]

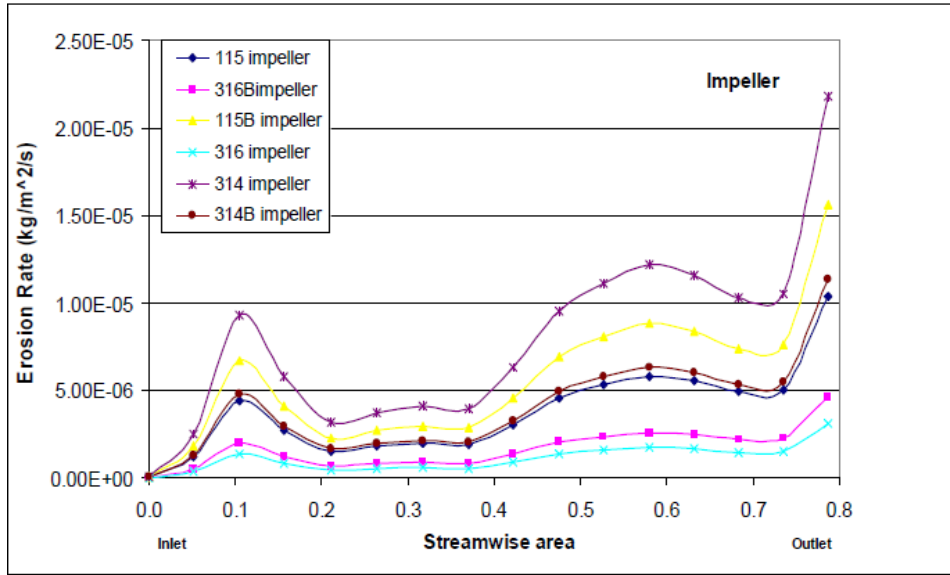


Figure 15: Streamwise Erosion Rates for the Impeller Using Different Coating Materials Which Are Calculated by CFD[41]

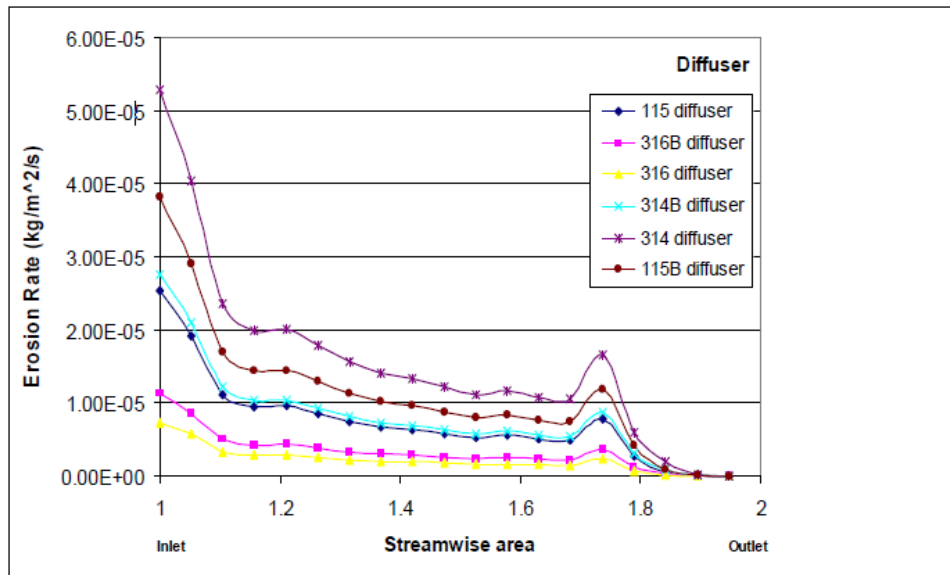


Figure 16: Erosion Rates for the Diffuser Using Different Coating Materials Which Are Calculated by CFD [41]

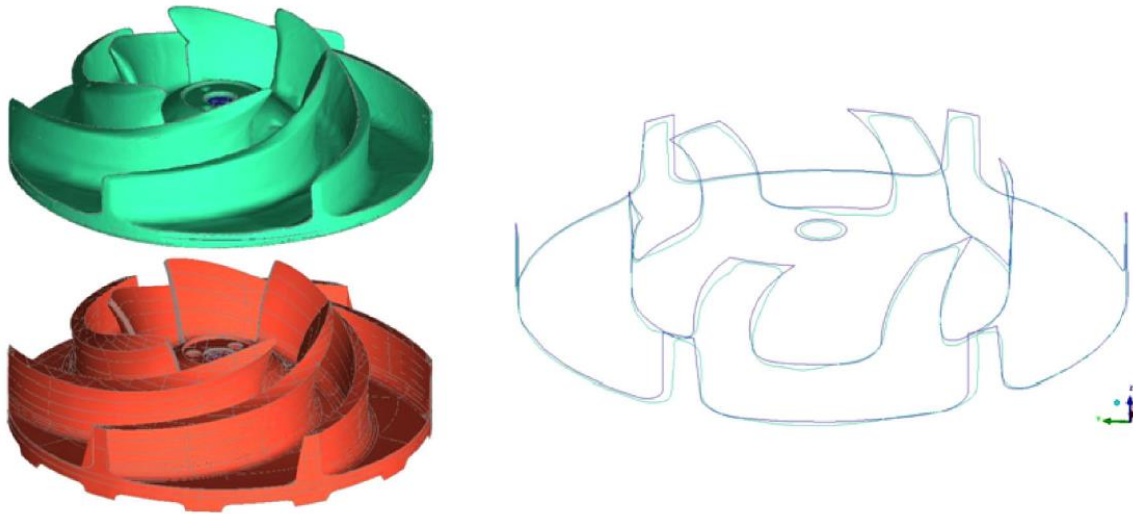


Figure 17: Original (Red) and Eroded (Green) Impeller and Profiles of Them in Best Fit [30]

Krüger, Martin, and Dupont (2010)[30] performed 2 phase simulations on the original and eroded centrifugal pump, respectively. **Figure 17** shows the 3D scanned model of original and eroded pumps. They calculated the erosion factor on both pumps by applying the empirical equation (17) given by Gulich[29]. **Figure 18** presents the comparison of these two pumps on key parameters, such as particle impingement angle, solid concentration, and water turbulence kinetic energy. According to their conclusion, the "shock like" erosion at the leading edge is properly presented; while for the "friction like" erosion at the trailing edge, tip clearance, and side plate, Gulich's model seems not equally applicable.

$$EF = F_{KG} \left(\frac{c_{S,eq}}{c_{S,Ref}} \right) \left(\frac{w_{mix}}{w_{Ref}} \right)^3 \quad (17)$$

w_{mix} : Mixture velocity (m/s)

w_{ref} : Reference velocity (10m/s)

$c_{S,eq}$: Equivalent solids concentration (kg/m³)

$c_{S,eRef}$: Reference solids concentration (kg/m³)

F_{KG} : Particle Size Factor

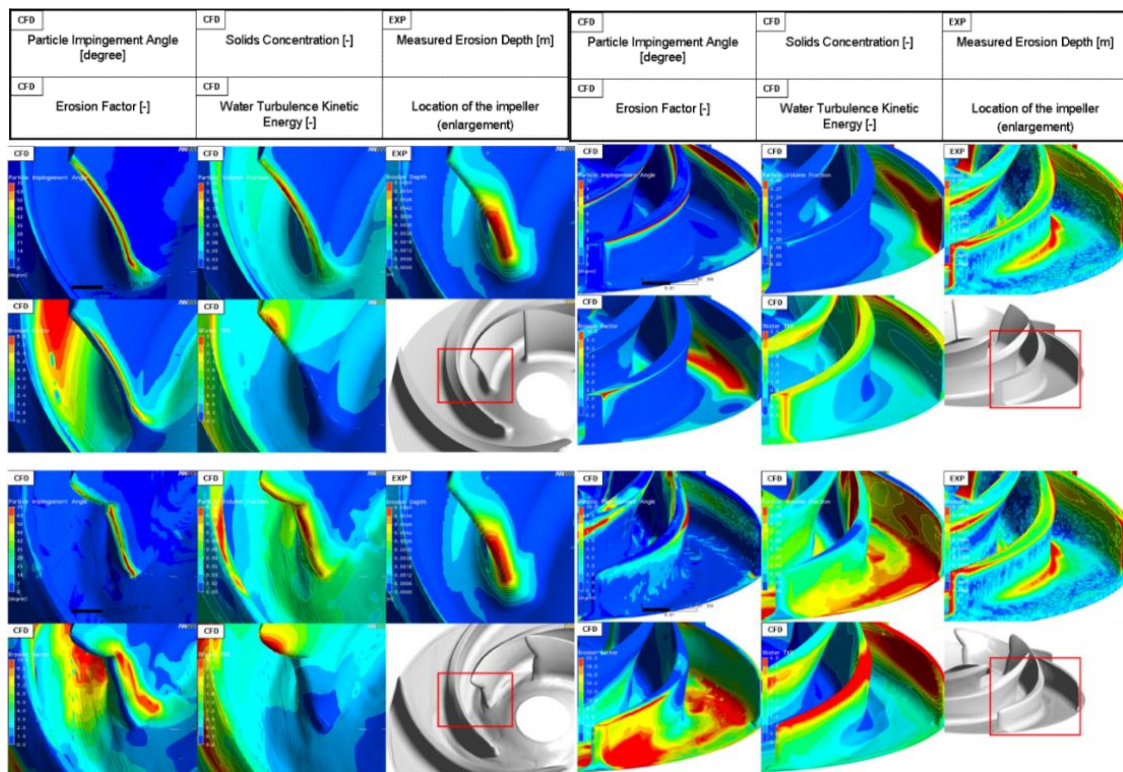


Figure 18: Key Erosion Parameters for Initial (Upper) and Eroded (Lower) Impeller's Leading Edge(left) and Trailing Edge(right) [30]

Pagalathivarthi, Gupta, and Tyagi(2011)[40] predicted the qualitative trends of erosion wear inside a 2D pump casing domain of a centrifugal pump casing by utilizing

FLUENT. The simulation applied Discrete Phase Model (DPM) for the slurry flow and standard k- ϵ model for turbulence.

Diaz, Saleh, and Zheng built an open loop test rig for erosion study of an ESP in 2012 [36] [37][38]. An 185-hour erosion test was conducted on a 3-stage mixed pump in this new test rig. To explore the mechanism of wear with gas entrainment, they ran the pump with water and sand in the 1st 117 hours, and with 15% GVF extra air in the next 68 hours. Performance and vibration data were collected for inspecting erosion. According to their test results, the waterfall plots in **Figure 19** show the vibration signature in frequency and amplitude at 117th and 185th hours. The trend of the peak growth is similar to what happened on the bearing clearance, especially on the subsynchronous peak of $2/3X$ (X is the rotating frequency of the shaft). Moreover, efficiency dropped 6.58% after 117 hours and 15.8% after 185 hours. Considering the relatively shorter period and greater efficiency loss for three phase test, they concluded that the pump performance degraded significantly more after air was involved.

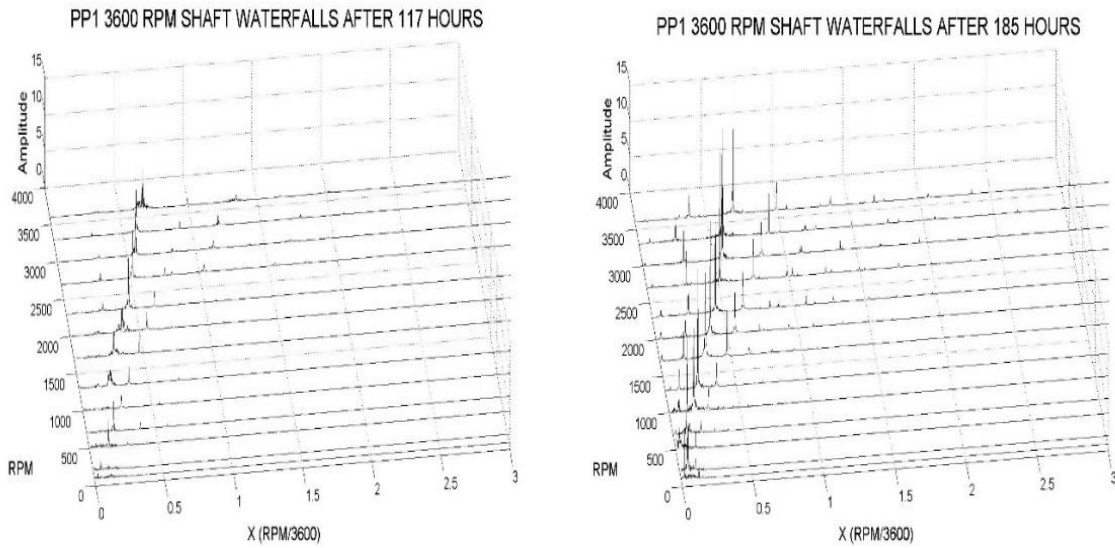


Figure 19: PP1 Shaft Waterfall at 117 and 185 Hours [36]

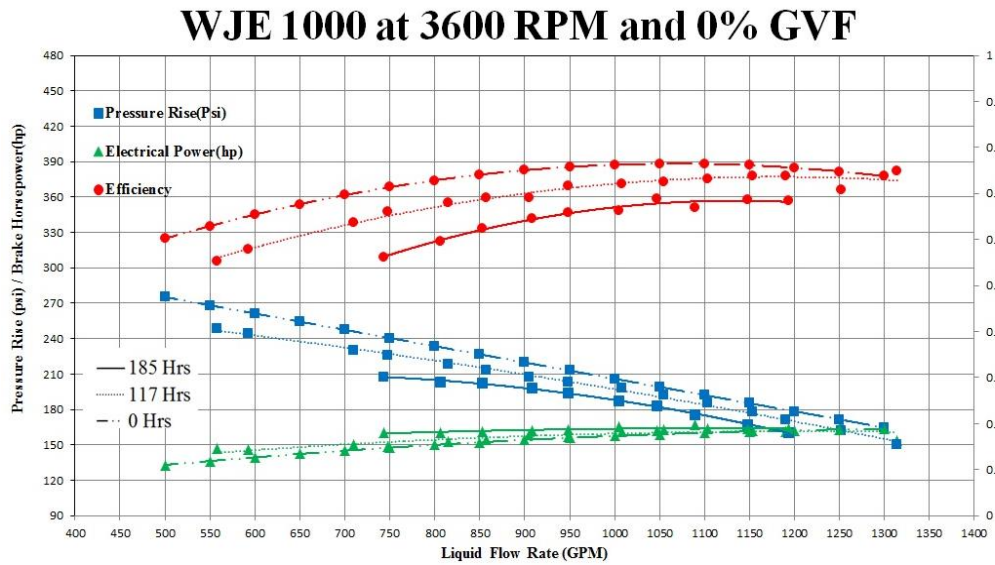


Figure 20: Pump Performance Curve with Pure Water at 0-117-185 Hours [36]

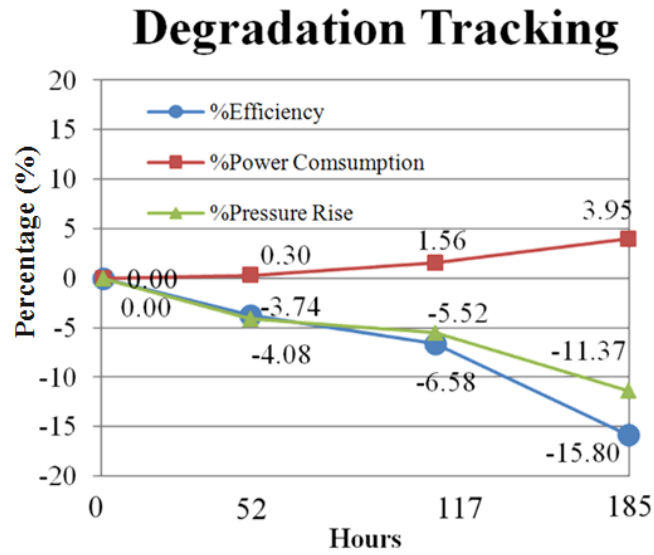


Figure 21: Performance Degradation with Pure Water [36]



Figure 22: Wear Marks on Different Stages [36]

Component wear patterns due to abrasive erosion were detected on both the main flow field and secondary flow field. In the main flow field, material loss on the hub, shroud, blades, balance holes of the impeller and shroud of the diffuser were observed in different levels. **Figure 22** shows the wear on leading edge of 2 impellers. Bearing

clearance and impeller labyrinth both contribute to the secondary flow wear. Bearings appeared to have grooves upstream, and crack patterns downstream of the secondary flow. They assumed the grooves were made by sand grinding and “cracks” were caused by material fatigue (**Figure 23**).

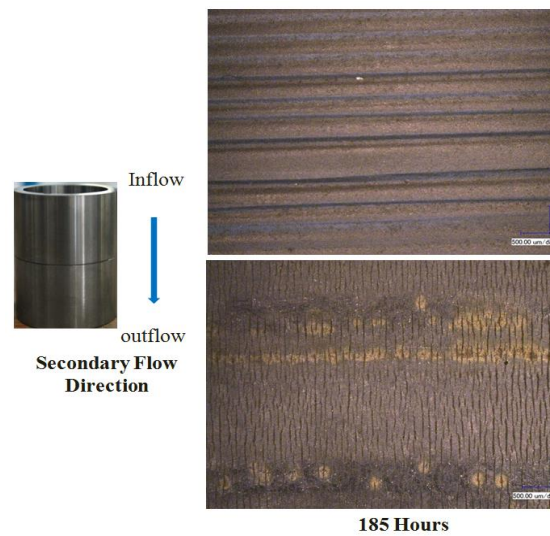


Figure 23: Scoring Wear and Hair Crack [36]

Subsequently, Pirouzpanah and Morrison (2014) [32] conducted a simulation on particle-laden flow in this pump by applying the Eulerian-Granular scheme using Ansys-FLUENT. An empirical-numerical model for predicting erosion was developed by correlating the erosion key parameters with the experiment data (**Figure 24**, equation (18) (19)). Erosion rate distribution on this pump was compared with the eroded surface of the ESP after 117-hour erosion test (**Figure 25**).

$$EF = (c_s)^{0.08} \left(\frac{V_s}{\bar{V}_{s0}} \right)^{0.07} \left(\frac{k_w}{\bar{k}_{w0}} \right)^{1.25} \quad (18)$$

$$ER = A \cdot EF^2 + B \cdot EF \quad (19)$$

ER: Erosion Rate ($\mu\text{m/hr}$)

EF: Erosion Factor

c_s : Sand volume fraction

V_s : Near wall sand velocity, m/s

\bar{V}_{s0} : Reference sand velocity, m/s

k_w : Turbulent kinetic energy of water, m^2/s^2

\bar{k}_{w0} : Reference turbulent kinetic energy of water, m^2/s^2

A= 0.0163, B=0.8774

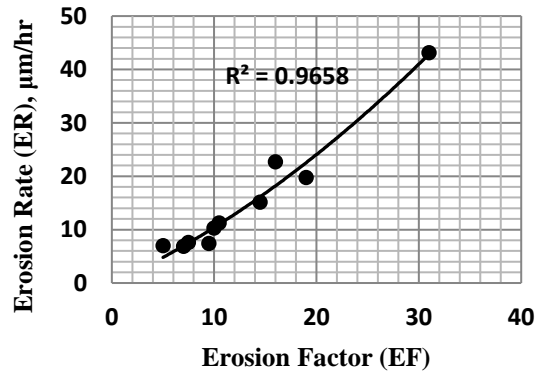


Figure 24: Erosion Rate for the Computed Erosion Factor Values[32]

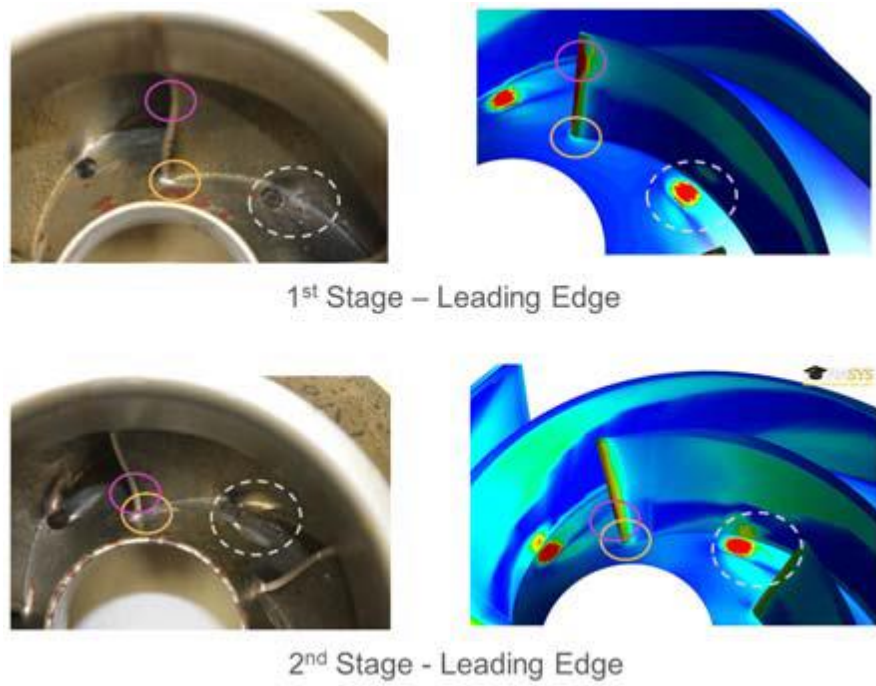


Figure 25: Comparison between the Computed Erosion Rates with the Eroded Locations in the First 2 Impellers [32]

2. OBJECTIVE

As mentioned earlier, erosion of an ESP is an inconvenient problem which directly affects the reliability of the ESP system. Erosion tests on the pump before installation can provide a more accurate prediction on the pump life span and effectively avoid an early failure of the ESP system. Analysis of the erosion process and the erosion mechanism of the pump will help the designer strengthening the endurance of the ESP system and reducing the cost spent on ESP underground installation.

The purpose of this study is to analyze the material loss, performance loss, reliability issue and erosion rate of a helico axial pump undergoing an erosive environment which includes gas, liquid, and particles.

Material loss is evaluated by measurement of volume loss and weight loss. For the volume of material loss, the 3D scan of the ESP can provide a more accurate measurement of the geometry change.

Performance loss is directly caused by the material loss of the ESP. An experimental-numerical combined analysis is given based on the performance maps plotted by the data from performance tests and CFD simulation on the new and eroded ESP. The geometry of the eroded ESP is processed by the 3D scan.

The reliability issue is mostly determined by the performance of the bearing. The stability of the bearing performance is analyzed based on the profiles and the waterfalls of the orbits. The increase of bearing clearance is also used to evaluate the material loss and bearing performance.

To predict the erosion rate of the ESP, a CFD simulation is performed on the gas-liquid-solid flow in the ESP. A popular empirical expression for predicting erosion rate is selected and calibrated based on the metal loss of an impeller. The impact angle, impact velocity, and the sand flush rate are considered in this erosion model. Due to the difficulty to consider all the erosion factors, a certain deviation between the metal loss measured from the test and the metal loss predicted in the simulation is expected. An assessment of the erosion model weighing the cost and accuracy is given.

3. METHODOLOGY

3.1 Experimental Setup

3.1.1 Test Rig

The erosion test rig in Turbomachinery Laboratory at Texas A&M University was originally built by N. Diaz and R. Saleh [37] [38]. **Figure 26** is a systematic view of it. A three-phase (Water-Sand-Air) flow loop (red pipes) is the main component of this open system. A 5,000-gallon tank is the main water supplier for the system which is connected to a cooling loop as well. **Table 1** lists the names of the equipment labeled in the loop in **Figure 26**.

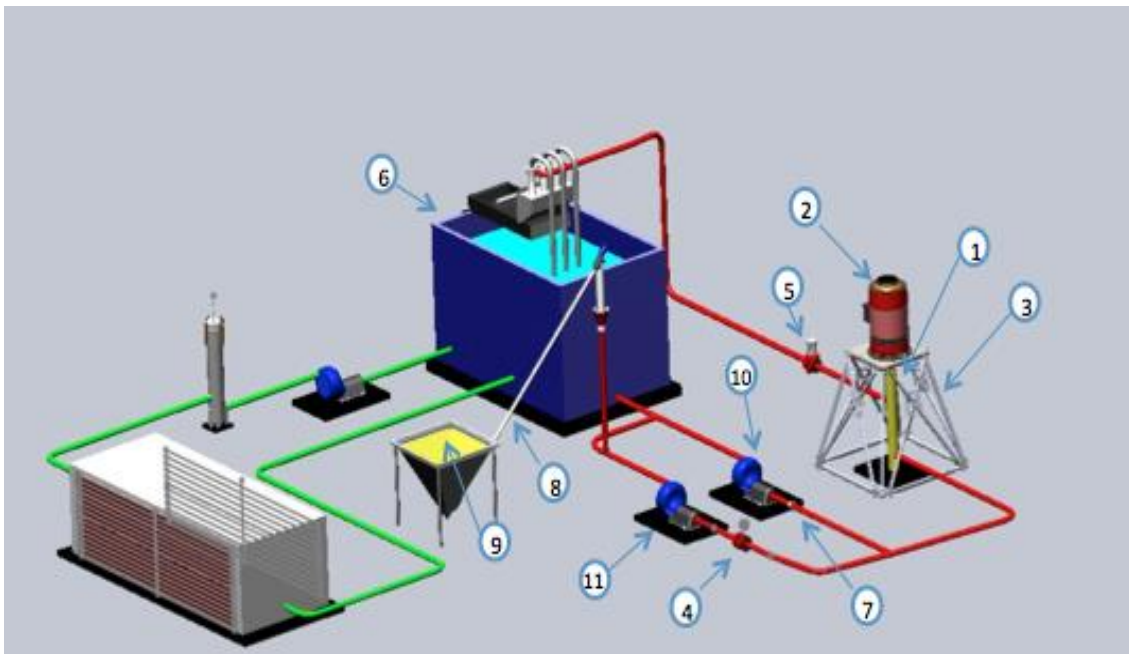


Figure 26: Experimental Setup Diagram.[37]

Table 1: Identification for Items in Figure 26[37]

No.	Item
1	ESP Pump
2	ESP Motor
3	Derrick
4	Coriolis Flow Meter
5	Pinch Valve
6	Tank and Separators
7	Orifice Flow Meter
8	Sand Auger
9	Sandhopper
10	Feed Pump
11	Slurry Pump

Figure 27 is the piping and instrument diagram(P&ID) of this setup. A sand auger and a hopper are used to transport the dry sand to the top of a standpipe and drop sand into the slurry loop which feeds 5% of the total water flow rate. A centrifugal pump(11) conveys the slurry through a Coriolis flow meter which measures the mass flow rate of the slurry. Another centrifugal pump(10) is used to feed the other 95% water to the ESP and provide enough net positive suction head (NPSH) for the ESP. The slurry and the water converge before entering the bottom tee inlet of the ESP. Air is supplied at 110 Psi by a medium pressure air compressor. It passes through a turbine flow meter and two paralleled control valves before entering and mixing with water and sand in the bottom tee. The ESP is assembled vertically and driven by a 250 HP motor. Downstream of the ESP outlet, there is a pinch valve controlling the total flow rate of the pump. The separator system contains a group of cyclone separators and a shaking separator. Through this system, used water will be mostly recycled and sent back to the supply tank, while used sand will be separated and dumped so as to avoid uncontrolled erosion.

Meanwhile, in order to protect all the equipment in the loop from overheating, a heat exchanger in the cooling loop (green) is running all the time to keep the liquid temperature at the pump inlet below 120°F.

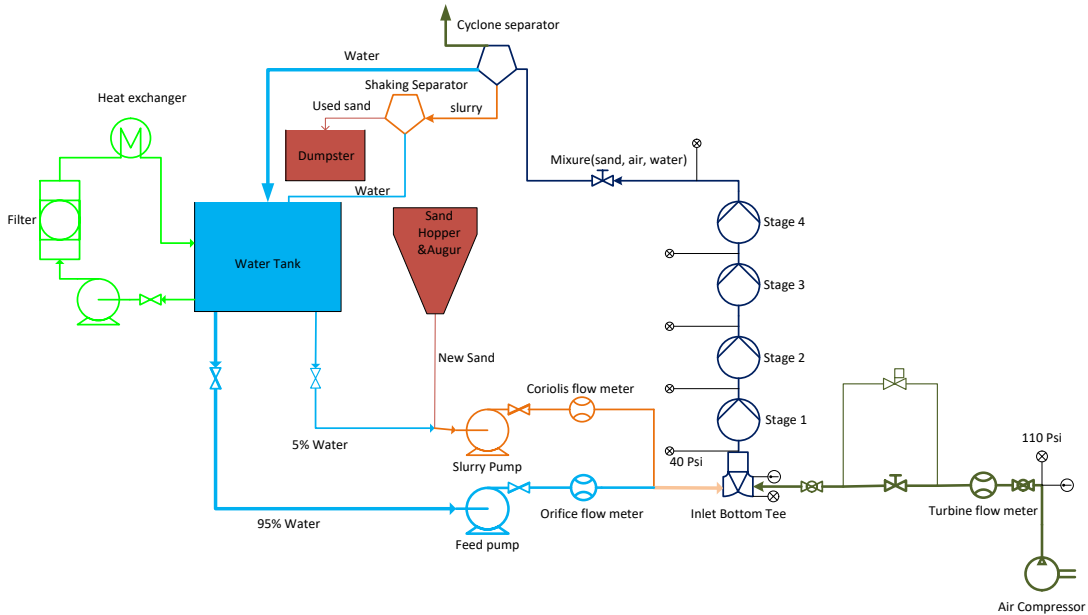


Figure 27: P&ID for Poseidon ESP Erosion Test Rig

The Poseidon ESP has 4 stages in all. **Figure 28** shows more details of the derrick with the Poseidon ESP assembled inside. To balance the thrust, a mechanical seal (gray part in **Figure 29**), which can handle 1000 lb up thrust and 20,000 lb down thrust, is assembled above the outlet head (green part in **Figure 29**).



Figure 28: Erosion Loop Indoor Parts

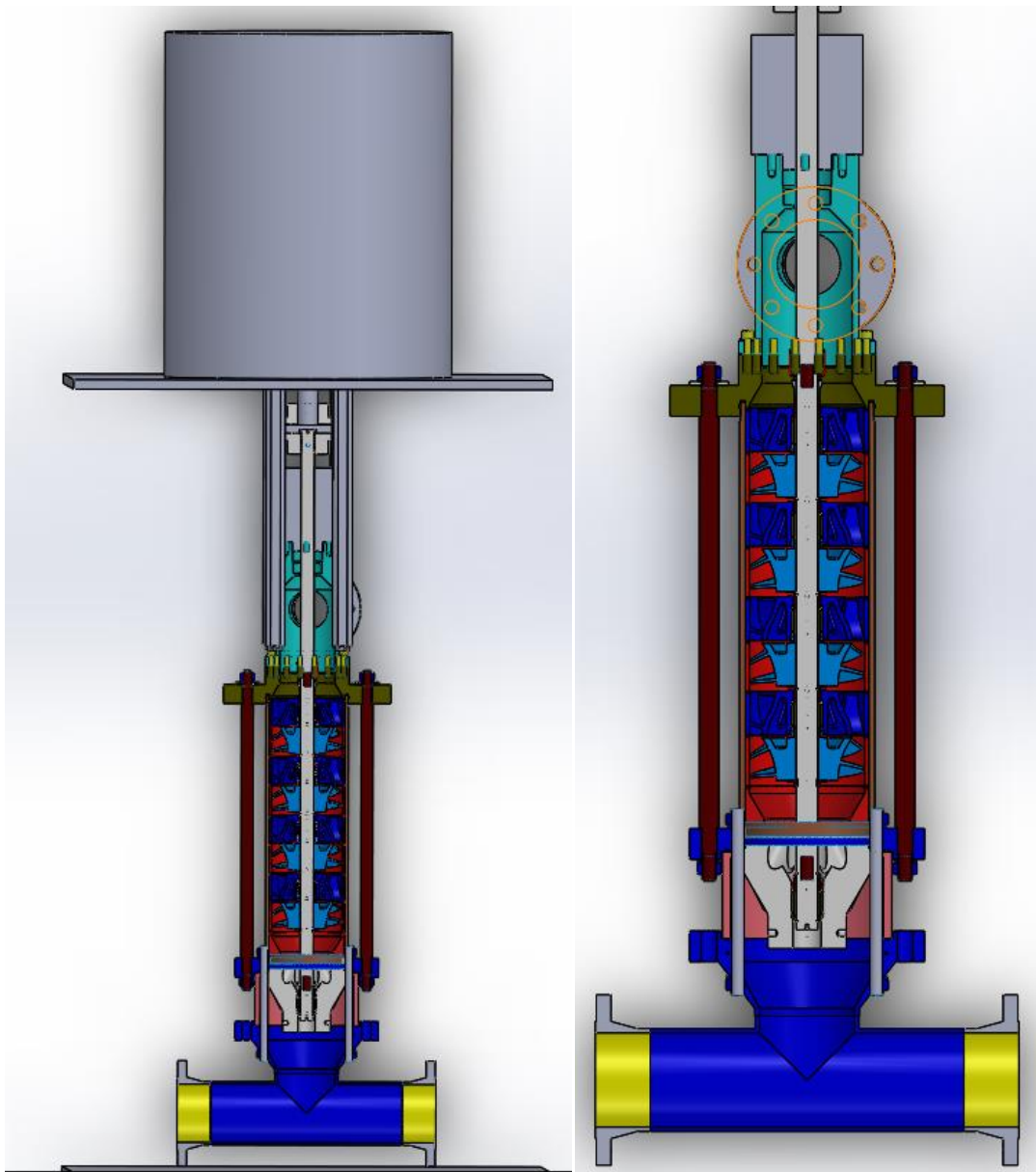


Figure 29: Poseidon Pump Installed in a Derrick(SolidWorks)

3.1.2 Poseidon ESP

Figure 30 to Figure 33 exhibit the original impeller, diffuser, and bearing of the Poseidon pump. Erosion of these components are the primary contributions to efficiency loss and pump failure of an ESP system. Therefore, their metal losses caused by erosion will be measured in this study.

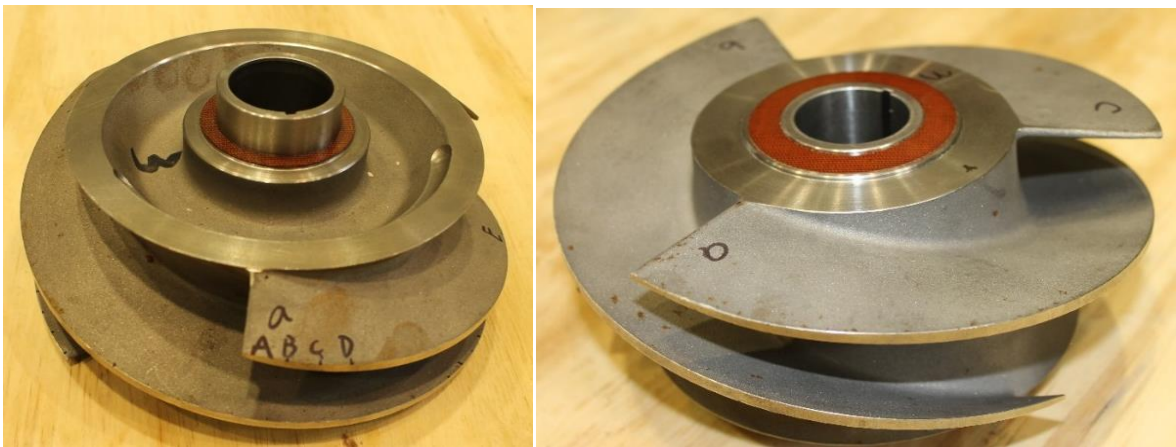


Figure 30: Impeller of Poseidon ESP



Figure 31: Diffuser of Poseidon ESP

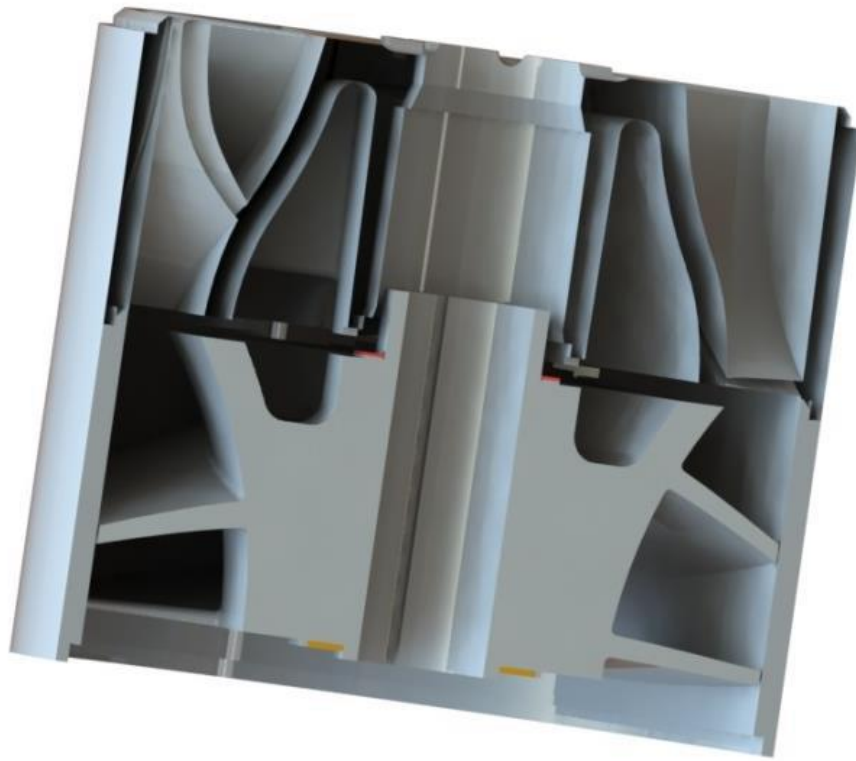


Figure 32: Sectional View of a Stage of Poseidon ESP[43]

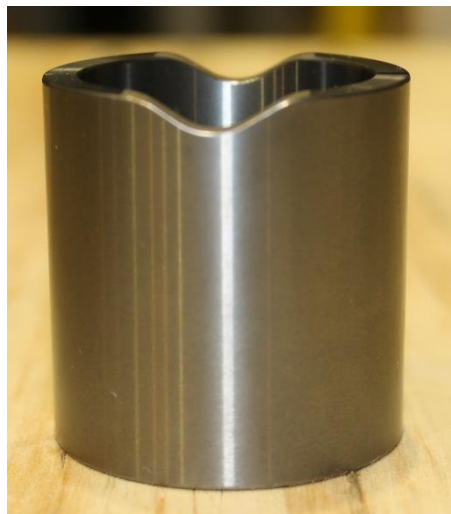


Figure 33: Journal of the Poseidon ESP

3.1.3 Operating Condition

Table 2: ErosionTest Operating Conditions

Item	Value	Unit
Sand concentration	2.3-2.4	gram/liter
Water flow rate	880	gpm
Inlet pressure	40	Psi
Gas Volume Fraction(GVF)	20	%
Rotor speed	3600	RPM
Stage number	4	

Table 2 is the erosion test operating condition utilized for 200 hours. The water flow rate at 880 GPM is the BEP at 20% GVF as obtained from the performance curve for the new ESP.

3.1.4 Sand Property

Sand labeled 100-mesh was purchased from Sierra Frac Sand, LLC. **Figure 34** shows the sand analyzed by the sifting equipment in Turbomachinery Laboratory. **Table 3** is the properties of the sand, and **Figure 35** exhibits the microscopic view of the sand. Both of them are provided by STIM-LAB.

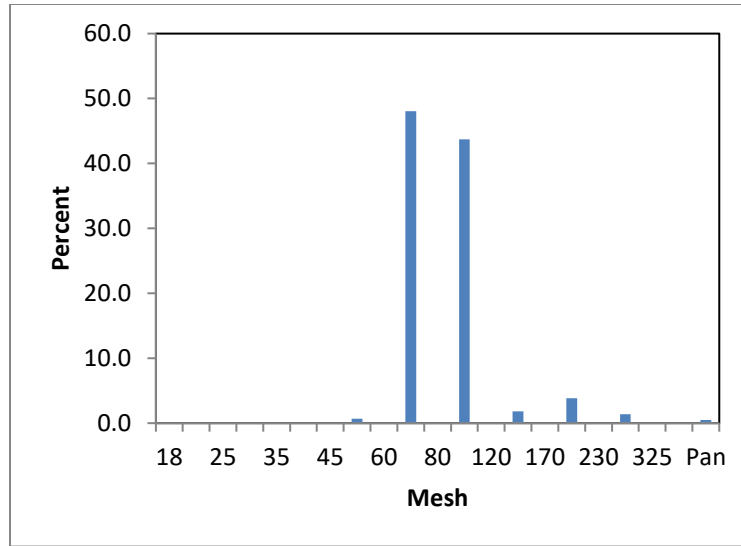


Figure 34: Sand Analysis(size distribution)

Table 3: Sand Properties

Property	Value	Unit
Sphericity	0.6	
Roundness	0.6	
Bulk Density	1.44	g/cm ³
Density	2.64	g/cm ³
ISO Mean Dia.	0.164	mm
Median Dia.	0.157	mm



Figure 35: Microscopic View of New Sand

3.1.5 Performance Measurement

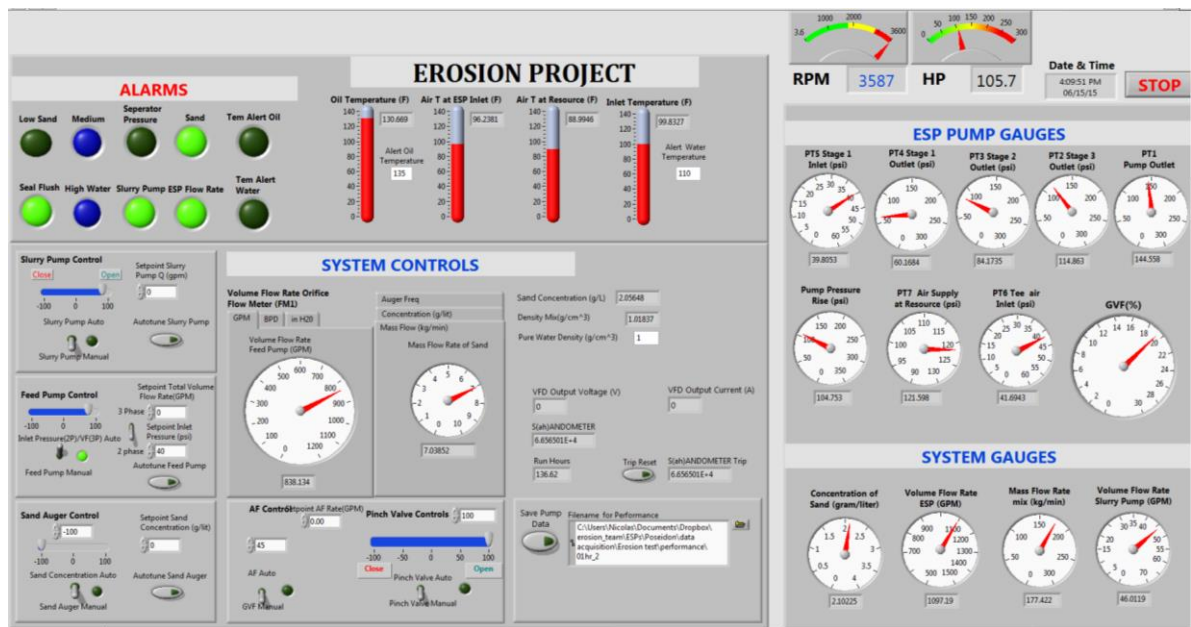


Figure 36: Operating Interface- Test Rig Control and Performance Data Capturing.

Figure 36 exhibits the operating interface in LabView. Current values on it show that the pump is running at the operating conditions given by Table 2. Five pressure sensors are used to obtain the pressure rise of each stage, the other two are collected for calculating the air flow rate. Thermocouples monitor the temperature of the liquid in the cooling loop of the mechanical seal as well as the liquid in the main loop. The temperature of the air at the inlet tee is also collected for calculating the air flow rate. Two water flow meters record the water flow rate. The feed pump is set to maintain a constant pressure at the inlet (40 psi). The slurry pump is set to supply 50 GPM water.

The sand augur maintains the sand concentration at 2 gram/L. Air flow rate is kept at 20% GVF by the control valve.

3.1.6 Vibration Measurement

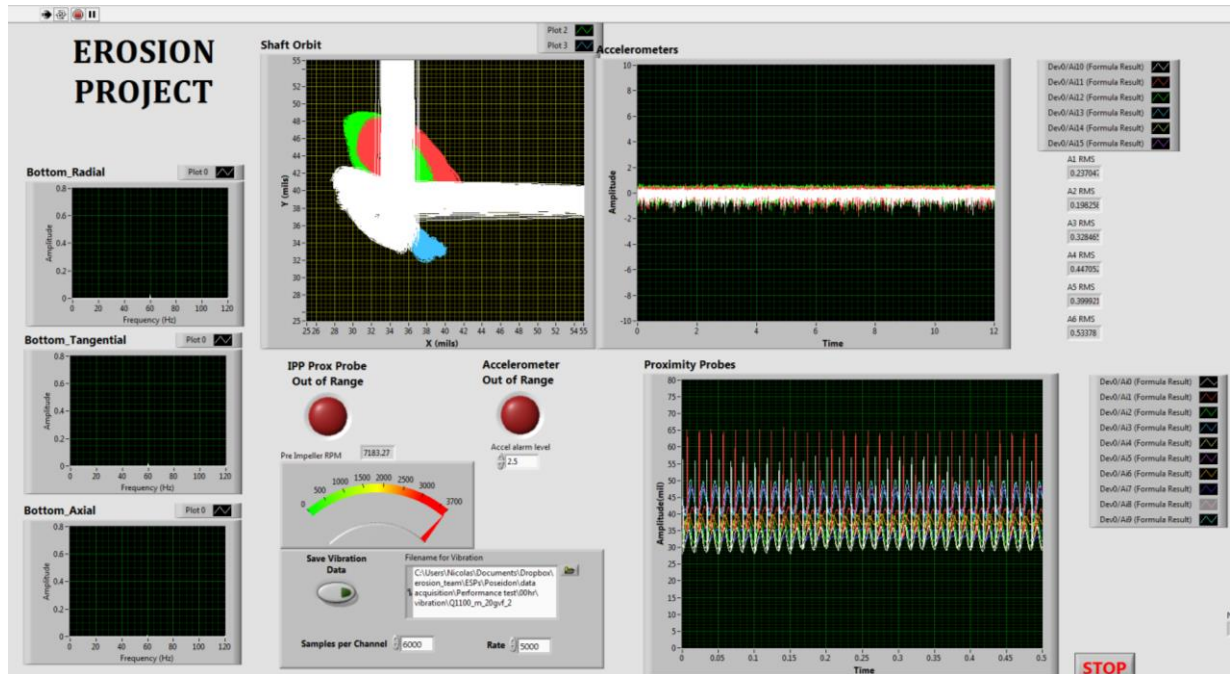


Figure 37: Monitor Interface-Vibration Data Capturing.

Figure 37 shows the monitor interface in LabVIEW corresponding to the performance data. In order to measure vibration, six proximity probes are inserted. Limited by the geometry of pump, probes can only be inserted near the outlet of the diffuser, pointing at the spacers on the shaft (**Figure 38**, **Figure 39**, **Figure 40**). Moreover, there is no space for proximity probes on the 4th diffuser. In order to avoid perforating the blades on the

diffuser, the angle between both probes is 120° . The shaft orbits in the picture are plotted before transformation to an orthogonal coordinate frame.

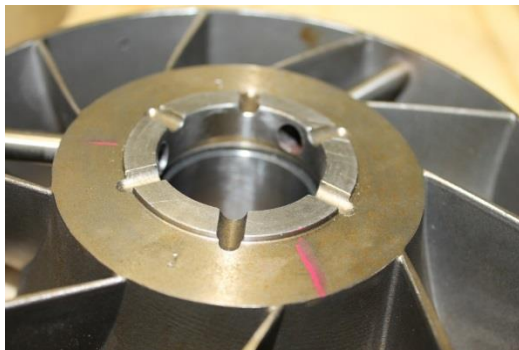


Figure 38: Proximity Probes Location at 1st Diffuser

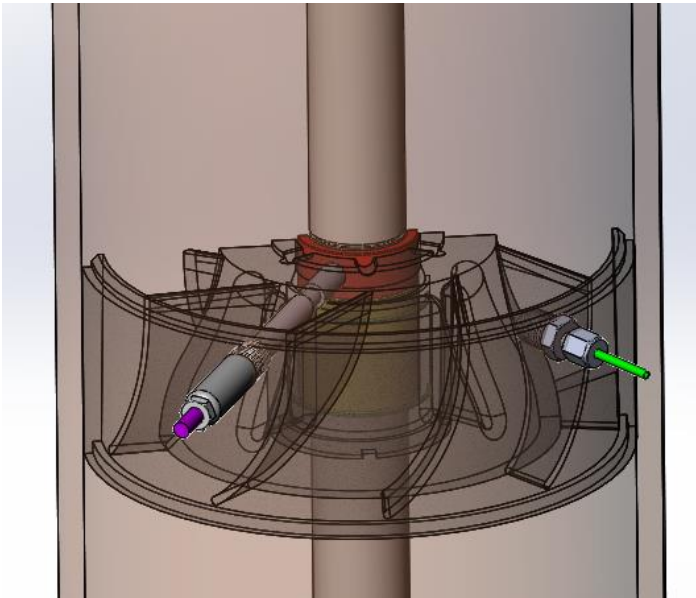


Figure 39: Locations of Proximity Probe(red) and Pressure Sensor(green) at 1st Diffuser (Solidworks)

Two accelerometers are mounted below the top flange and above the bottom flange of the pump assembly, and are aligned with the proximity probes. Each of them measures accelerations in 3 directions, as is shown in **Figure 40**.

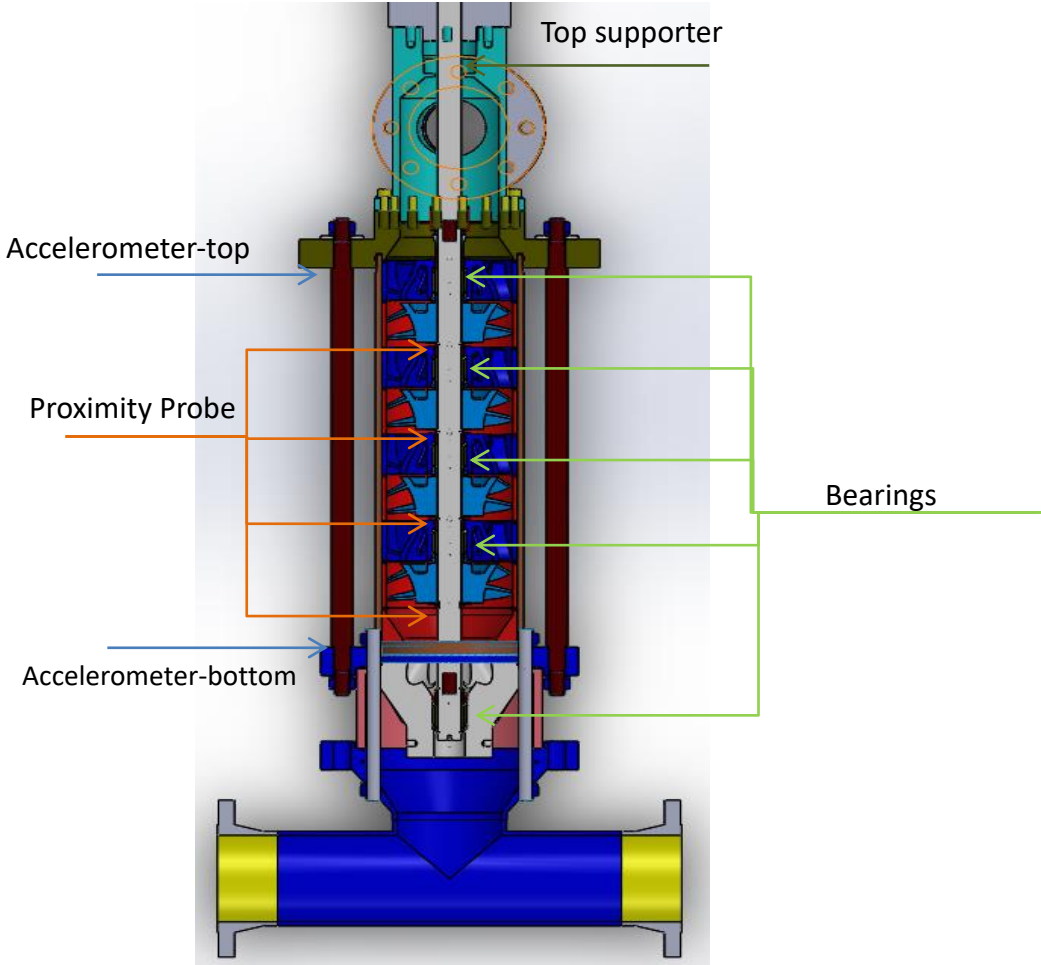


Figure 40: Schematic View of the Vibration Measuring Locations

3.2 Test Procedure

3.2.1 Introduction of Comprehensive Performance Test

Performance data including stage-by-stage pressure, water/air flow rate, sand concentration, gas volume fraction, etc were recorded hourly. Vibration data correlated was also captured, which includes the 3-direction accelerations at 2 locations. System reliability was analyzed through monitoring the head loss and magnification of accelerations.

At the 0th, 25th, 50th, 66th, 100th, 150th, 200th hour (**Figure 41**), the erosion test was stopped and comprehensive performance tests were conducted. This comprehensive test includes the performance test for acquiring the performance maps, the RPM test for plotting the vibration waterfall, Ramp-up, and Ramp-down test. Sand in the loop is flushed out before these tests. Only when there is no sand can the proximity probes be installed to collect the shaft orbits. **Table 4** presents the matrix of operating conditions in the test.

Table 4: Performance Test Matrix

Hour	Valve Position (For Liquid flow rate with no air, GPM)	GVF	
0	600	0	25%
25	700	5%	30%
50	800	10%	35%
66	900	15%	40%
100	1000	20%	45%
150	1100		
200			

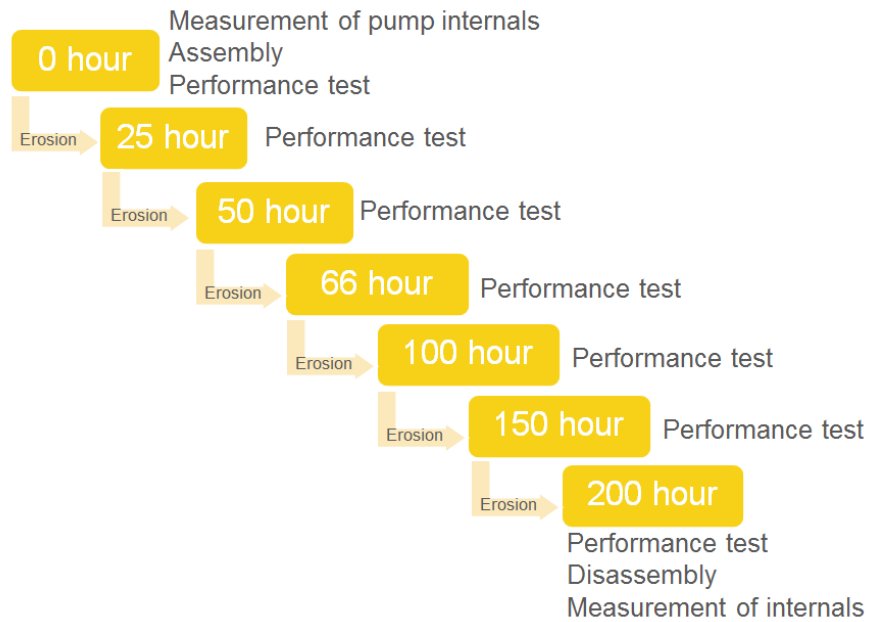


Figure 41: Comprehensive Performance Tests Scheduled During Erosion Test.

3.2.2 Practical Issues in Data Trueness and the Solutions

The pump inlet pressure is supposed to be constant (40 Psi) during the erosion test. However, in the test, the pressure sensor to measure the pump inlet was too close to the impeller inlet, which affected its accuracy. So the pressure sensor at the air inlet of the bottom tee is now used as the inlet pressure. In addition, the 4th diffuser was identified to be rotating at the 1st 100 hours and then stopped rotating after 150th hour. This will affect the pressure rise of the 4th stage. Therefore, although some correction has been done and the corrected performance would be plotted, the 4th stage performance will seldom be considered in the analysis.

3.3 Record of Geometry Change

In order to investigate the wear on the key components, the geometry information of the impellers, diffusers, diffuser spacers were recorded by measurement as well as 3D scanned before assembling and after disassembling of the ESP.

3.3.1 3D Laser Scanner

A 3-D scan system in the Department of Mechanical Engineering at Texas A&M University (**Figure 42**) was utilized to capture the geometry of the Poseidon pumps. According to the product introduction [44], the 3-D scan system contains a tracking system, a scanner, and the image process software.

The tracking system (**Figure 43**), NDI's PRO CMM Model 1000, delivers 3D measurements using a high-speed optical tracker and dynamical part reference. It has a single point accuracy up to 20 μm and the application accuracy up to 35 μm .

An advanced 3D laser scanner, ScanTRAK (**Figure 44**), combines NDI's Multi-Sided Probe (MSP) and Perceptron's ScanWorks® V5 laser scanner. It can directly capture complex geometries that are translated into a common coordinate frame to produce digital 3D models. However, this scanner is not able to deal with the geometry whose surface is not accessible to the laser, so it can be used to scan the impellers only. The measurement accuracy, feature resolution and sensor feature repeatability of this scanner are 24 μm , 4.5 μm , and 5 μm respectively.

Image process software, Geomagic Studio(**Figure 45**), is used to receive the data in the form of point and present clusters of points in the process of scanning. Once all the surfaces of a component are basically represented by collected points, the scan is completed. After that, the image is processed based on the original points.



Figure 42: Instrument for 3D Scan



Figure 43: NDI PRO CMM Model 1000



Figure 44: NDI ScanTRAK

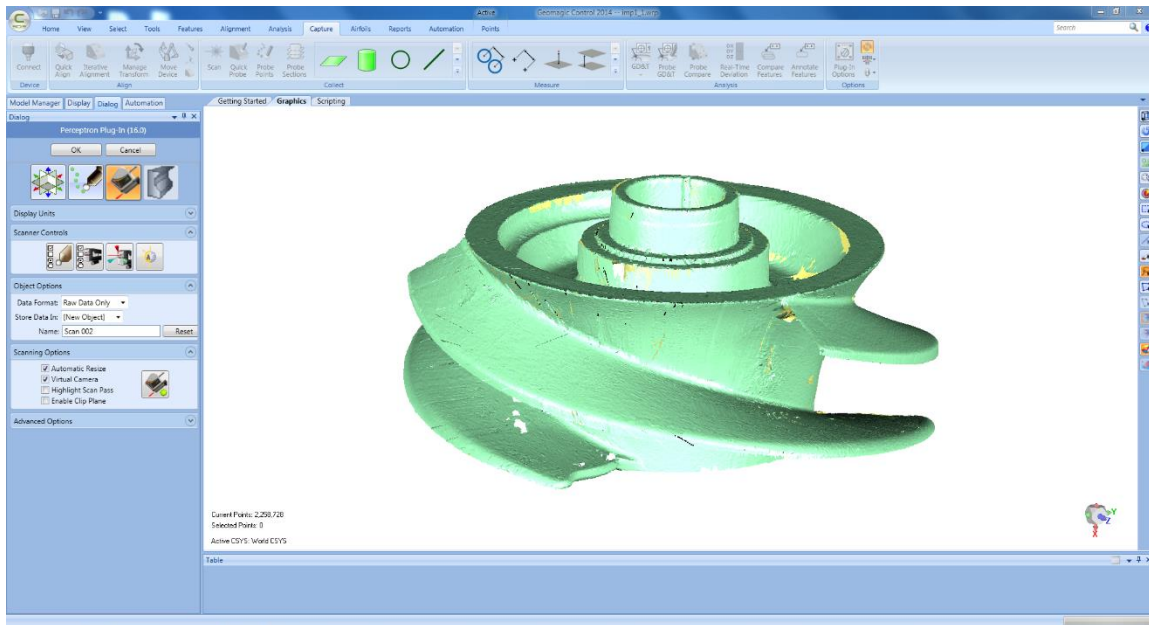


Figure 45: 3-D Scan Interface in Geomagic Studio (1st eroded impeller, points)

3.3.2 Image Process

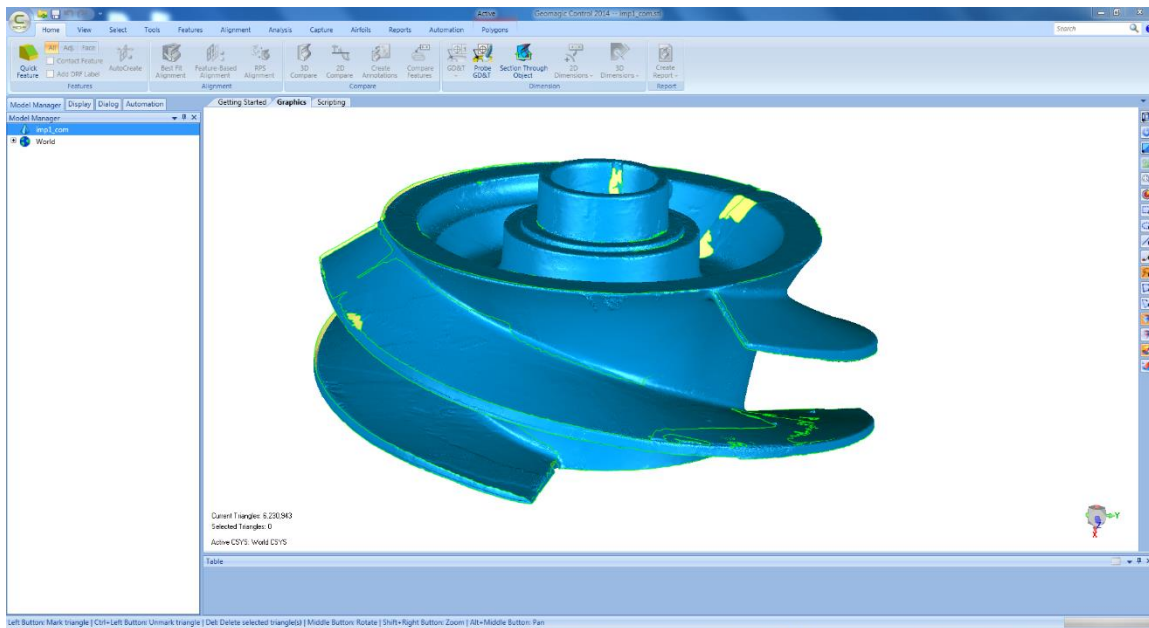


Figure 46: Preliminary Processed Image of The Original Impeller(polygons).

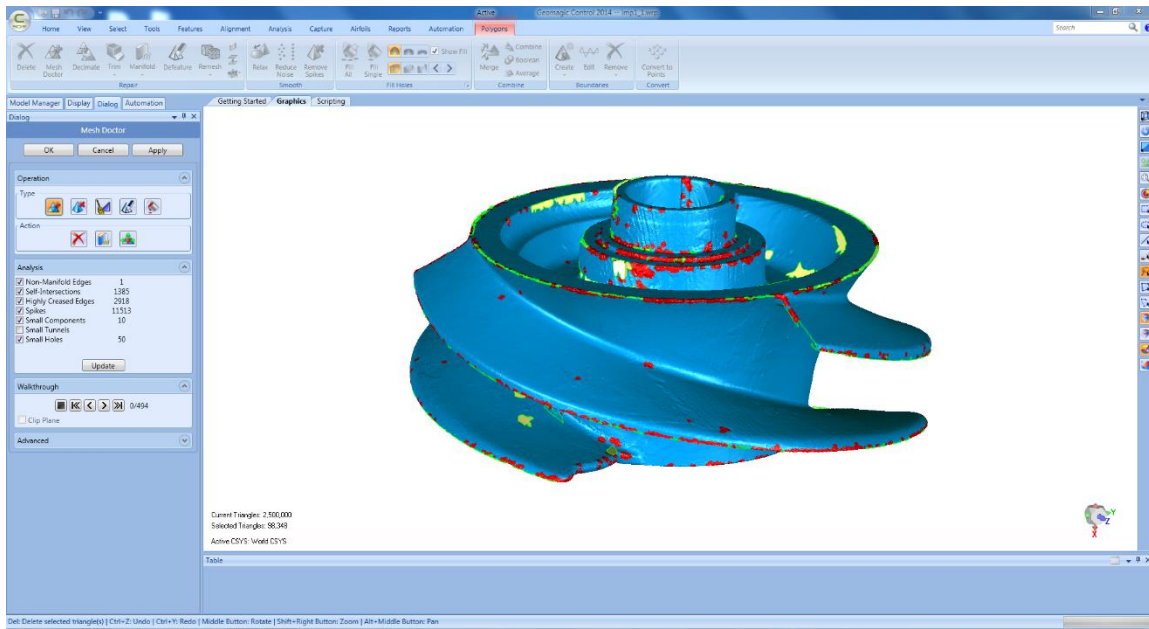


Figure 47: Preliminary Processed Image of 1st Eroded Impeller(polygons)

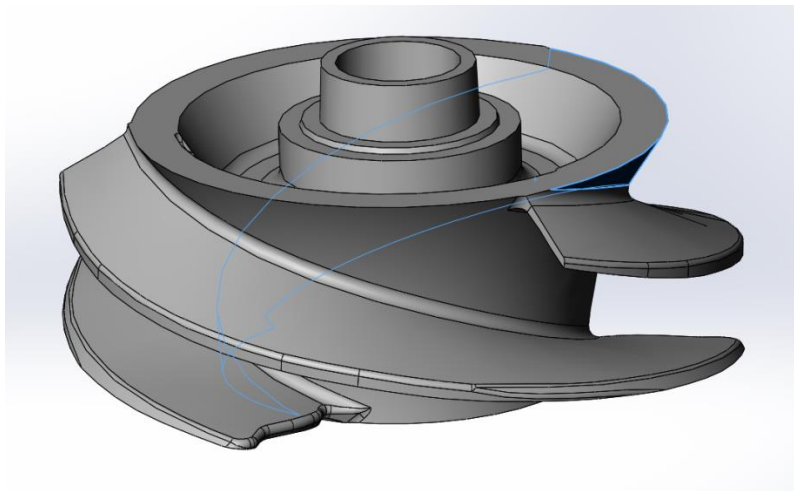


Figure 48: Finally Processed Image of 1st Eroded Impeller(surfaces)

Basically, image processing is to convert the 3-D scanned points into polygons and then polygons into surfaces. During these two steps, most erroneous data from the scan will be removed. However, some of the data representing the real geometry might also be changed due to the approximating modification or an improper process. **Figure 47** shows the preliminary processed image of an impeller which is transferred from points to polygons. **Figure 48** shows a successfully processed geometry of the impeller whose surfaces are smooth and continuously connected. More importantly, it can be read and edited by most CAD software. In this study, the polygon image is used to identify and quantify the geometry loss during erosion, while the surfaced 3-D model is used as geometry for CFD simulations.

3.3.3 Impeller Recorded by Camera and 3-D Scanner

With the help of 3-D scan, the geometries of all the 4 impellers were captured. Since the erosion on blades is more crucial in our study, it is bearable that the scan quality of the hub surfaces is not as good as that of the blade. To identify the wear of the impeller blades, geometries captured before and after erosion are aligned in **Figure 50**. The yellow part is the wear near the leading edge of each blade. And the measurement of wear at the leading edge of each impeller is on these figures.



Figure 49: 1st Impeller(Eroded and Original) Captured by Camera(left) and 3-D Scanner(right)

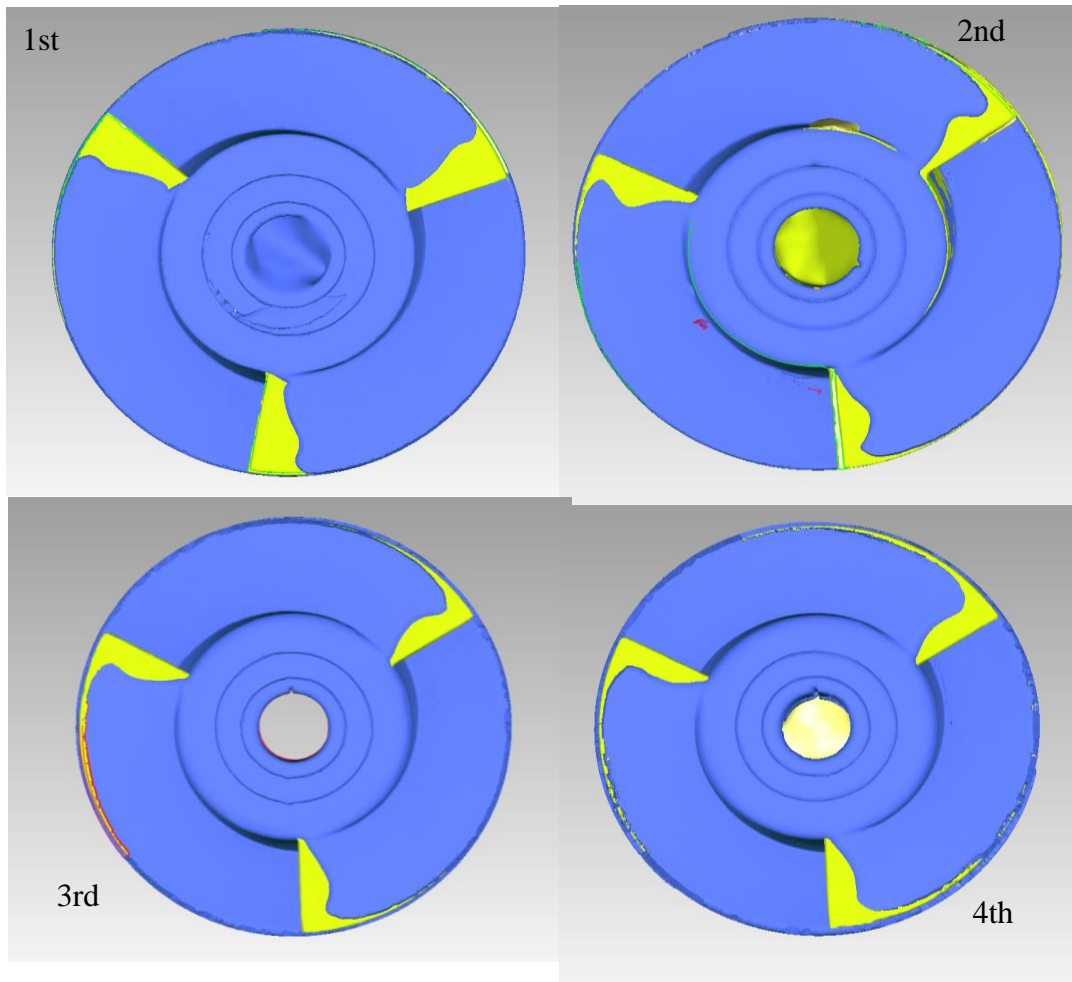


Figure 50: Comparison of Original and Eroded Impellers When Aligned Together

3.4 Numerical Simulation

In this study, the commercial software ANSYS FLUENT is used to calculate the single-phase, two-phase, and three-phase flow in this ESP. Erosion module issued by ANSYS is applied to extract the erosion-related parameters.

3.4.1 Two Ways to Investigate Erosion

Head loss and erosion related parameters derived from the simulations are utilized to investigate the pump erosion. In order to obtain the performance degradation caused by erosion, the performance maps of the new and eroded ESP are plotted in chapter 4. From observing the pressure distribution and related variables, the mechanism of head loss is expected to be determined.

Erosion rate can be predicted in a three-phase simulation by selecting a proper erosion model and calibrating it by the measurement of wear in **Figure 50**. As is discussed in the literature reviews [14][15] [21] [23], many factors decide the erosion rate. In this study, sand flush rate, impact angle, and impact velocity are selected to generate the erosion model. After knowing the erosion rate on a pump, the designer and manufacturer can improve the pump by strengthening the area with high erosion rate.

3.4.2 Geometry and Mesh for 1st Stage Performance

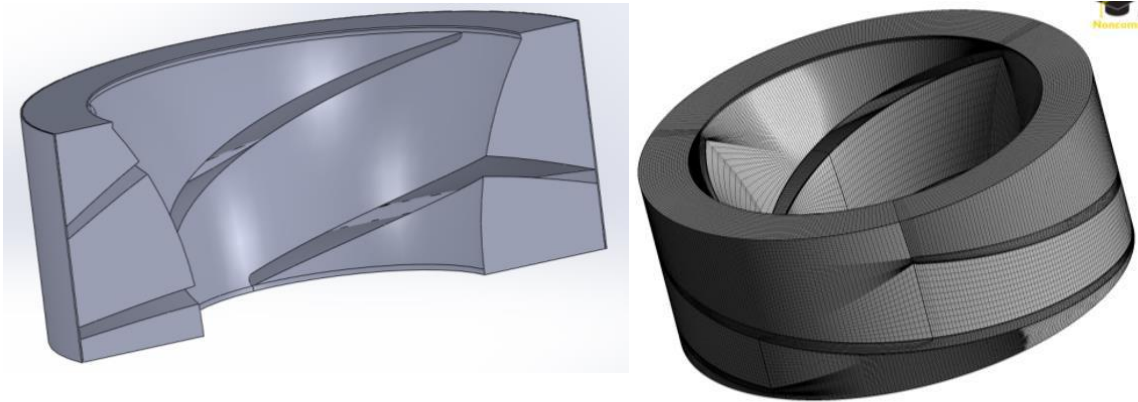


Figure 51: Geometry and Mesh of Original Impeller of the Pump[43]

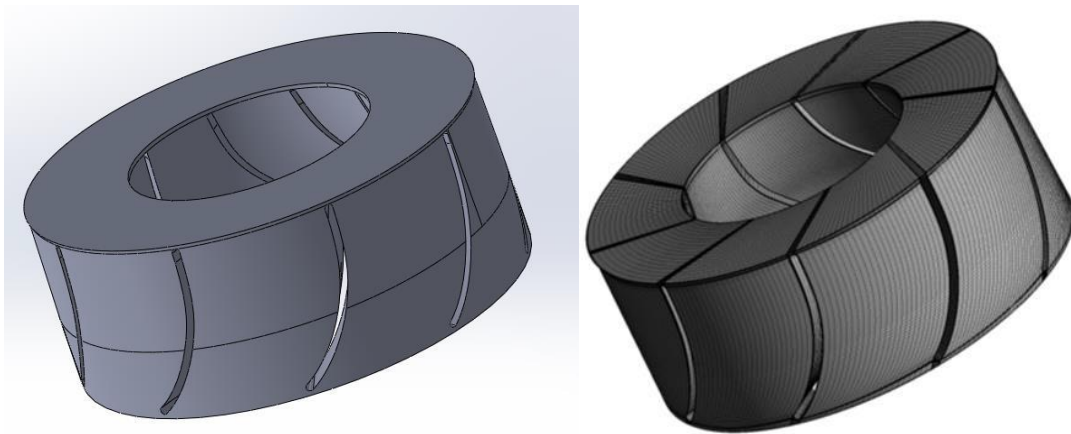


Figure 52: Geometry and Mesh of Original Diffuser of Poseidon Pump [43]

Flow paths for the new impeller were meshed by S. Reddy in Gambit[43]. About 3.71 million hexahedral elements were generated (**Figure 51**). Flow paths for the new diffuser were meshed by S. Reddy in ICEM(**Figure 52**)[43]. Around 0.94 million

elements were created. The geometry of the flow paths for the 1st stage eroded impeller is given by the 3-D model from image process in **Figure 48**. Grids are generated in ANSYS-Mesh (**Figure 53 to Figure 55**). Around 3.15 million tetrahedral and hexahedral mixed elements are generated. Grid independence study is conducted to verify the quality of meshes.

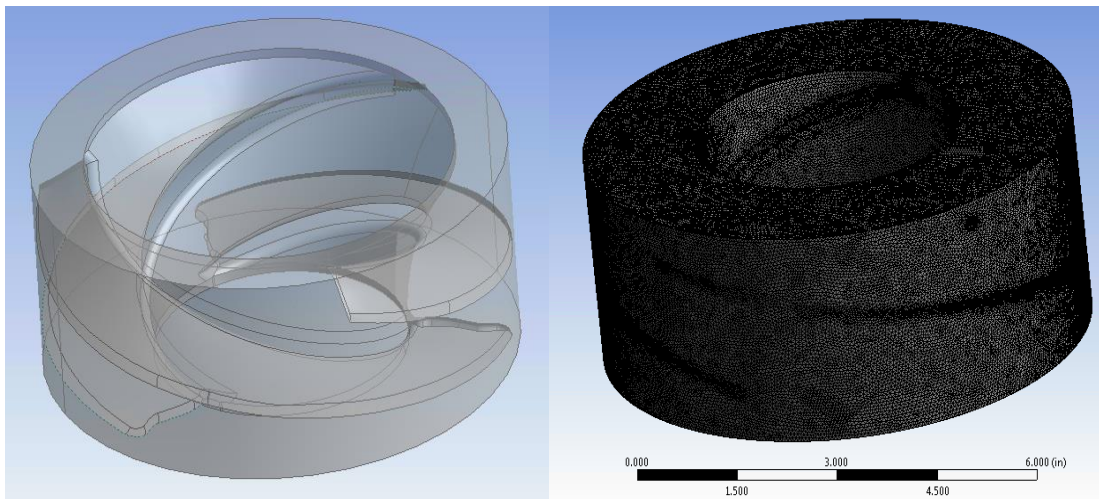


Figure 53: Geometry and Mesh of Eroded Impeller of 1st Stage

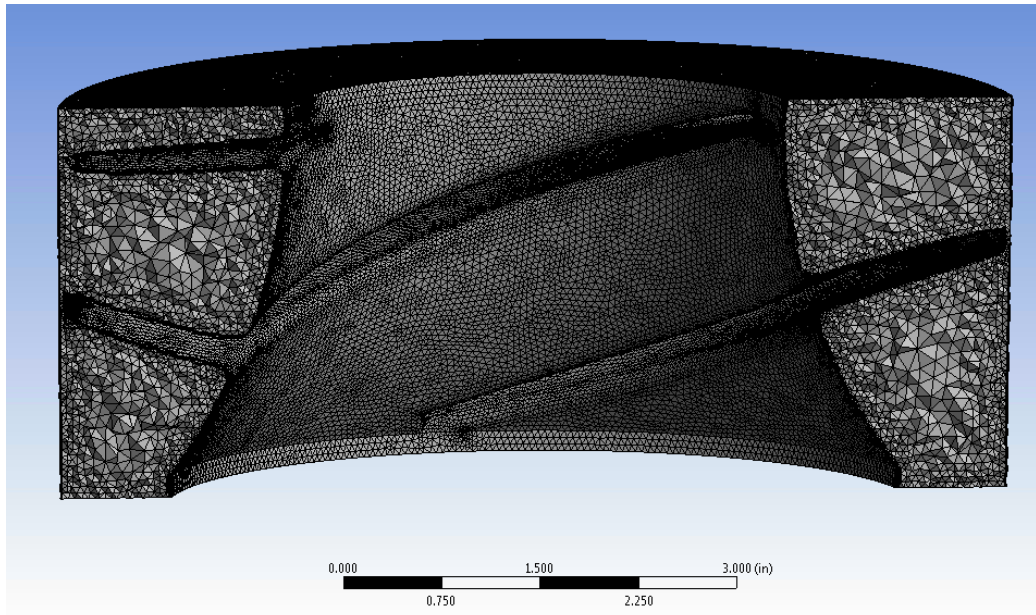


Figure 54: Geometry of Eroded Impeller of 1st Stage-Sectional View

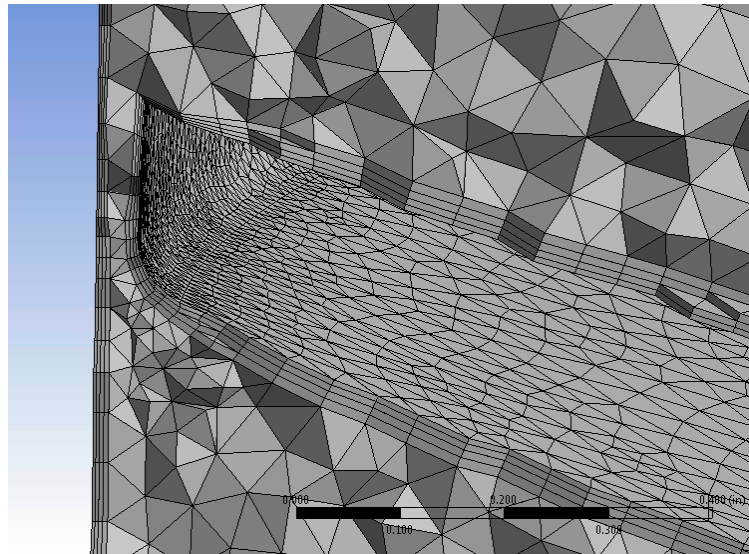


Figure 55: Geometry of Eroded Impeller of 1st Stage-Detail of the Tip Clearance

3.4.3 Time/ Grid Independence Study

Grids of the new impeller and diffuser were generated by Sujun Reddy[43]. In his study, the quality of the grids is verified. Thus, only the grid quality of the eroded impeller is analyzed here.

Before checking the grid, a time independence study is done to determine the proper time step for grid independence study. Seven simulations with different time steps are performed. Time step is presented in the form of rotated angle which is based on the time and angular speed. For example, “0.25 degree/step” means in one step the impeller has moved by 0.25 degree in “1.15741E-05 second”. The head ratio and torque ratio are referenced to the case that time step is 0.25 degree/step and the number of elements is 3.15 million. Boundary conditions are set as:

Water flow rate, 880gpm;

Outlet pressure, 65 Psi;

Angular speed, 3600 RPM.

For the time step independence study, the head, thrust, and torque calculated at different time steps are given in **Table 5**.

Table 5: Time Step Independence Study

Element no.(million)	3.15	3.15	3.15	3.15	3.15	3.15
Time step(degree)	0.05	0.1	0.25	0.5	1	2.5
Head(psi)	28.4	28.1	28	28.3	28.8	30.5
Head Ratio (%)	101.4	100.4	100.0	101.1	102.9	108.9
Y+	109.7	109.5	114.9	111.0	111.2	112.8
Y*	200.2	206.3	201.3	206.1	197.2	198.4
Thrust on Blade(N)	-2868	-2779	-2835	-2877	-2941	-3149
Thrust Ratio (%)	101.2	98.0	100.0	101.5	103.7	111.1
Total Torque(N*m)	61.580	-59.350	-60.160	-60.800	-61.790	-65.100
Torque Ratio (%)	1.024	0.987	1.000	1.011	1.027	1.082

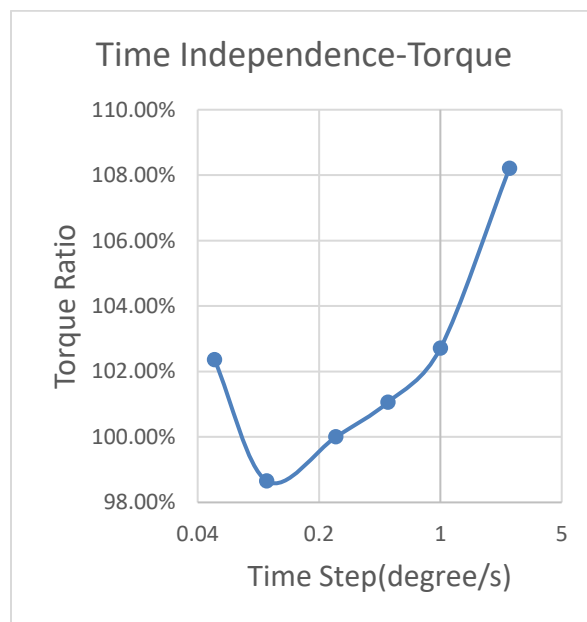


Figure 56: Torque Ratio in Time Independence Study

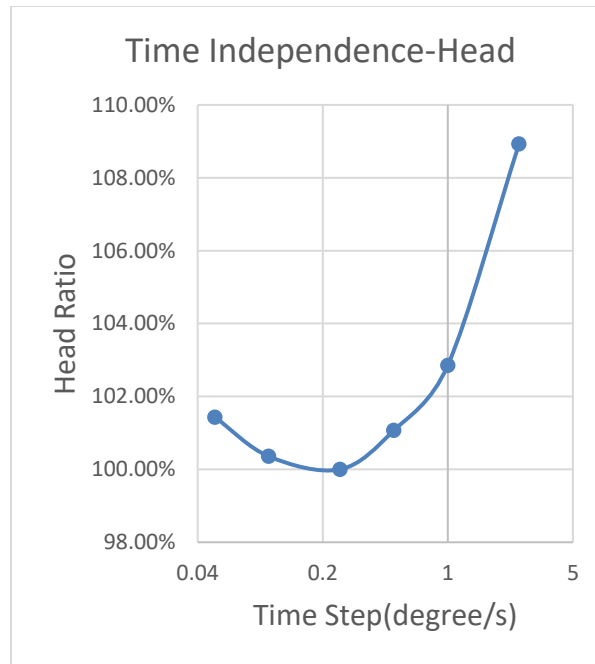


Figure 57: Head ratio in Time Independence Study, Logarithmic Scale in X-Axis

Figure 56 and **Figure 57** present head ratio and torque ratio for the different time steps. When reducing the time step from 2.5 degree/step, both the head ratio and the torque ratio go down, getting close to 100% and then go up. Considering that the time step which is too small will have the issue of truncation error, and the time step which is too big will lose the trueness of the rotating process, the proper time step is picked between 0.1 and 0.5 degree/s. At this range, the error would be limited to $\pm 1\%$. Both Y^+ and Y^* are given as reference. Since the mesh does not change, these values do not change much.

Table 6: Grid Independence Study

Element No.(million)	1.35	2.2	2.63	3.15	3.69	5.01
Time step(degree)	0.25	0.25	0.25	0.25	0.25	0.25
Head(psi)	27.8	28.1	28.3	28	28.2	28.1
Normalized head	0.993	1.004	1.011	1.000	1.007	1.004
y+	248.9	161.1	151.8	114.9	87.5	85.4
y*	440.5	297.100	268.200	201.3	143.9	150.9
Thrust on blade(N)	-2810	-2865	-2848	-2856	-2853	-2862
Normalized thrust on blade %	0.987	1.003	0.997	1.000	0.999	1.002
Total torque(N*m)	-62.83	-60.32	-60.24	-60.16	-60.03	-60.18
Normalized total torque	1.044	1.003	1.001	1.000	0.998	1.000

In **Table 6** the head, thrust, and torque calculated using different meshes are given. **Figure 58** and **Figure 59** show the head ratio and torque ratio for grid independence study. In the grid independence study, the time step is set as 1.15741E-05s (0.25 degree/s). When refining the mesh, the head ratio is fluctuating within $\pm 1\%$, while the torque ratio goes down from over 104% to 100% and then fluctuates within $\pm 1\%$. It seems that the torque of the impeller is more sensitive to grid density than the head of the impeller. Although torque is not analyzed in this study, it can reveal how accurate the simulation is when describing the flow field in the boundary layer. Y+ and Y* are the parameters used to describe the boundary layer. Therefore, the grids with no less than 2.2 million elements in this study, or in other words, (such as) the case that y+ is no more than 161, can be used to describe the single phase simulation at flowrate of 880 GPM. However, the flowrate in this numerical study will vary from 583 GPM (20 kBPD) to

1200 GPM (41 kBPD), so choosing a finer mesh would be a safer choice. The mesh with 3.15 million is utilized.

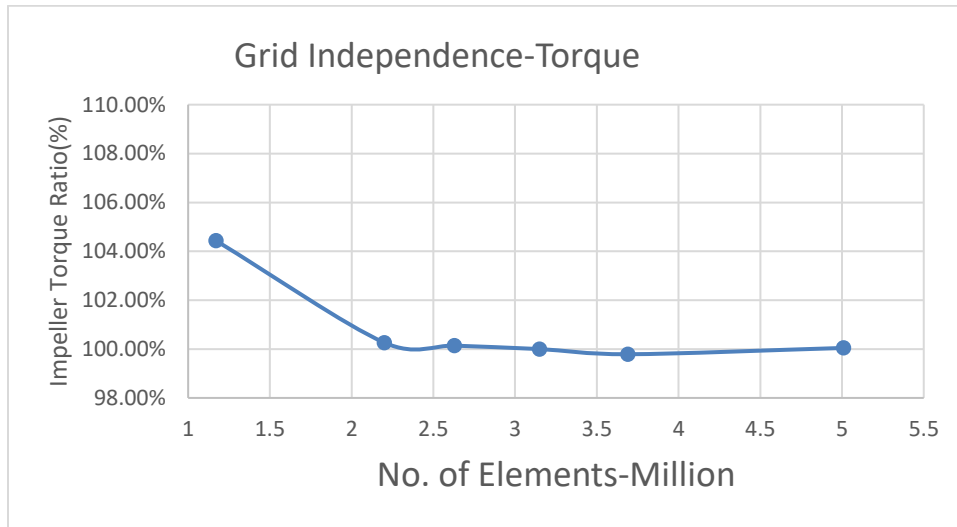


Figure 58: Torque Ratio in Grid Independence Study

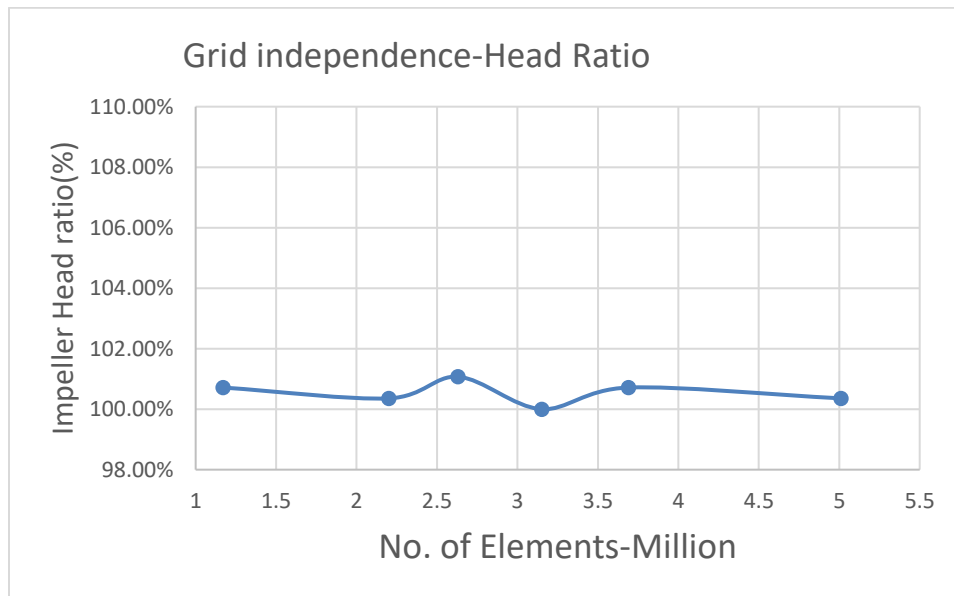


Figure 59: Head Ratio in Grid Independence Study

4. RESULTS AND ANALYSIS

4.1 Metal Loss of the Pump

4.1.1 Overview of the Wear



Figure 60: New and Eroded Diffuser of the 1st Stage



Figure 61: New and Eroded Diffuser of the 2nd Stage

Figure 60, Figure 61 and Figure 62 compare the new and eroded diffusers and impellers of the 1st and 2nd stages. The metal loss on the diffuser mainly appears at the trailing edge near the shroud, while the metal loss of the impeller is at the leading edge and the blade tip near the leading edge.

Each of the impeller housings, which are also called diffuser spacers, has minor erosion at the inner wall. The amount is too small to be observed, but it is measurable and will be analyzed later.

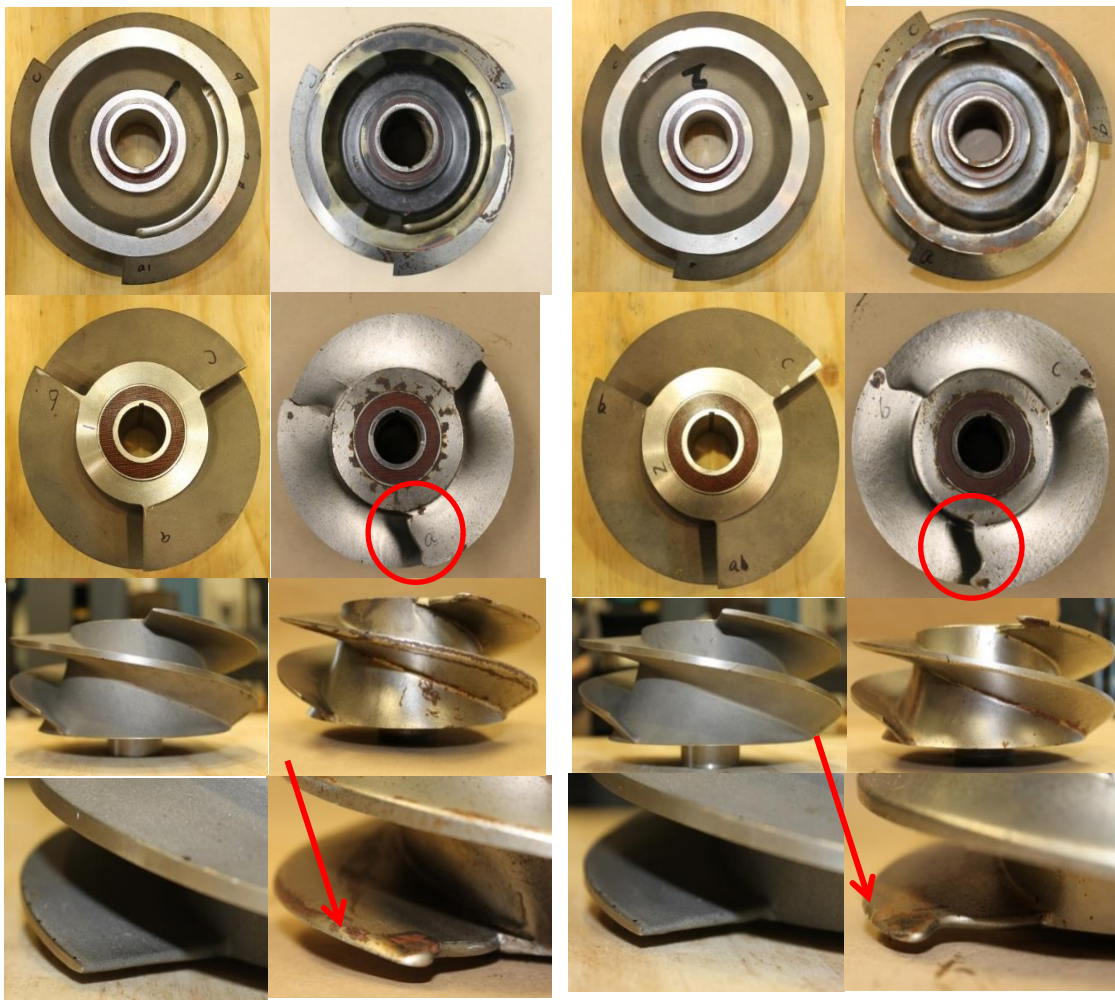


Figure 62: New and Eroded Impellers of the 1st Stage (Left) and 2nd Stage(Right)

4.1.2 Contour of Wear on the Impellers: 3D scan

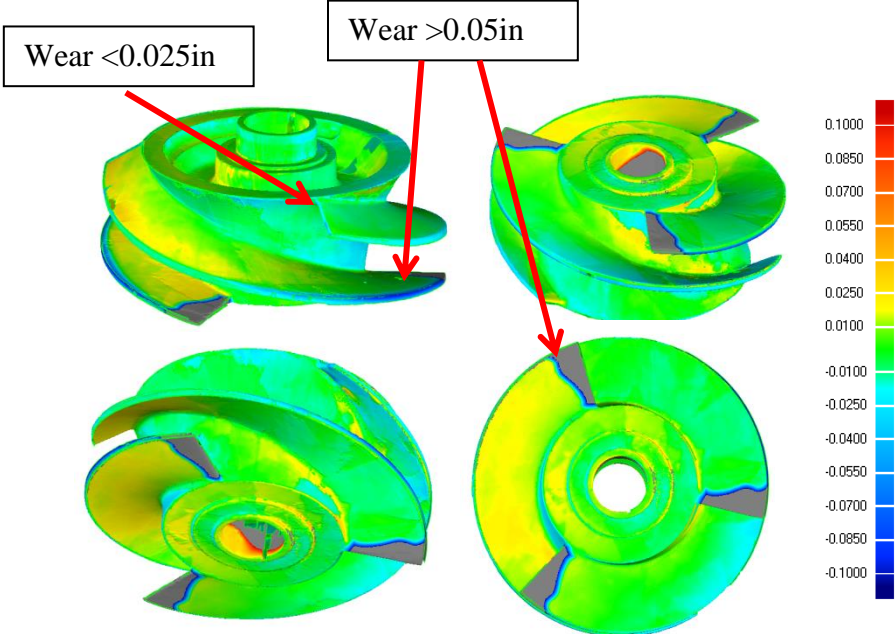


Figure 63: Surface Distance between New and Eroded Impeller 1 (Unit: inch)

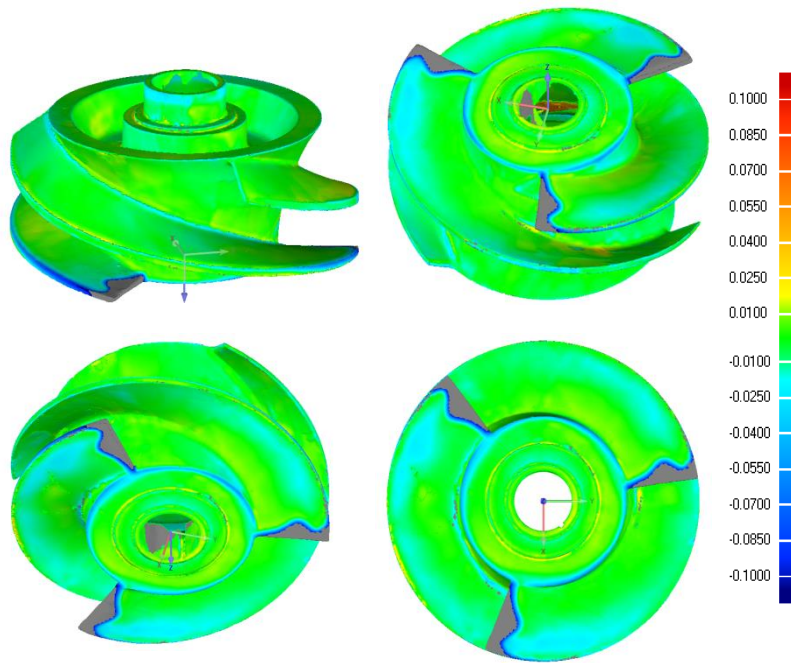


Figure 64: Surface Distance between New and Eroded Impeller 2 (Unit: inch)

As is mentioned above, the pictures captured by the camera cannot quantitatively show the metal loss. For example, the wear at the impeller blade tip is very small compared with the leading edge. But with the help of 3D scan, when the new and the eroded impellers are aligned together, the contours of their surface distance can directly represent the loss of thickness. (**Figure 63** and **Figure 64**) The gray area at the leading edge illustrates that the distance is large, exceeding the range (± 0.1 inch). The wear at the blade tip appears near the leading edge is more than 0.05 inch (blue). For the trailing edge, the wear goes below 0.025 inch (green). **Figure 65** reduces the range of the contour and increases the contrast of wear on the tip. It appears as a border dividing the

eroded area (green) and non-eroded area (red) on the tip. So, on the impeller, the wear mainly appears at the leading edge and the tip area from the leading edge to that border in **Figure 65**. These areas are mainly affected by impact wear. Some areas with yellow color (around 0.01-0.03inch) might come from the error in scan, image process and alignment. Slight deformation during pump blade disassembly might also contribute to it.

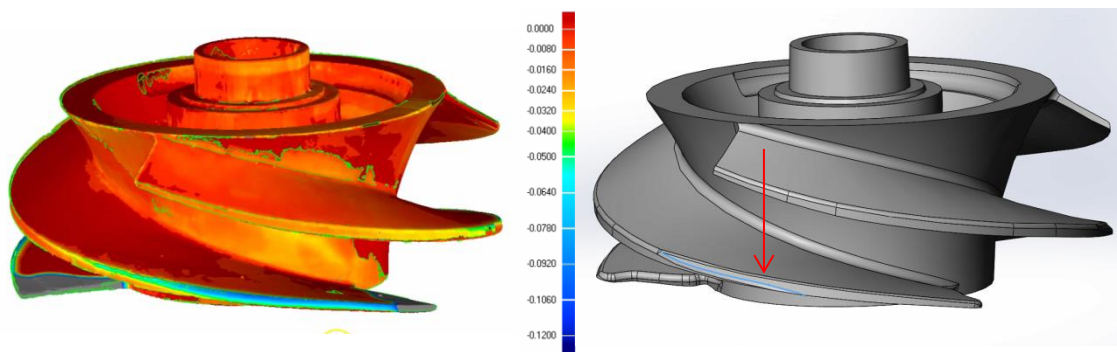


Figure 65: Boundary Dividing Wear Area on the Blade Tip of Impeller 1 (Unit: inch)

4.1.3 Tip Clearance Increase

Figure 66 presents the blade profiles in a sectional view when new and eroded impellers are aligned. The minimum distances between the blade tips are measured. It is not hard to identify that the wear near the pressure side of the tip is more than that near the suction side. It is assumed that the abrasive carried by the secondary flow from the pressure side to the suction side is the cause of the wear. **Figure 67** shows the overview of such measurement in **Figure 66** for the 1st impeller.

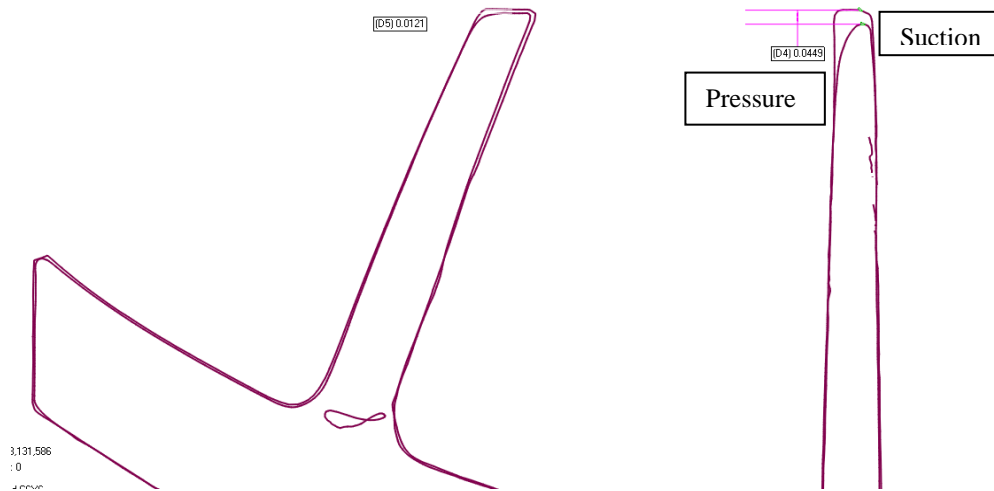


Figure 66: Measurement of the Wear on the Aligned Impeller Profile

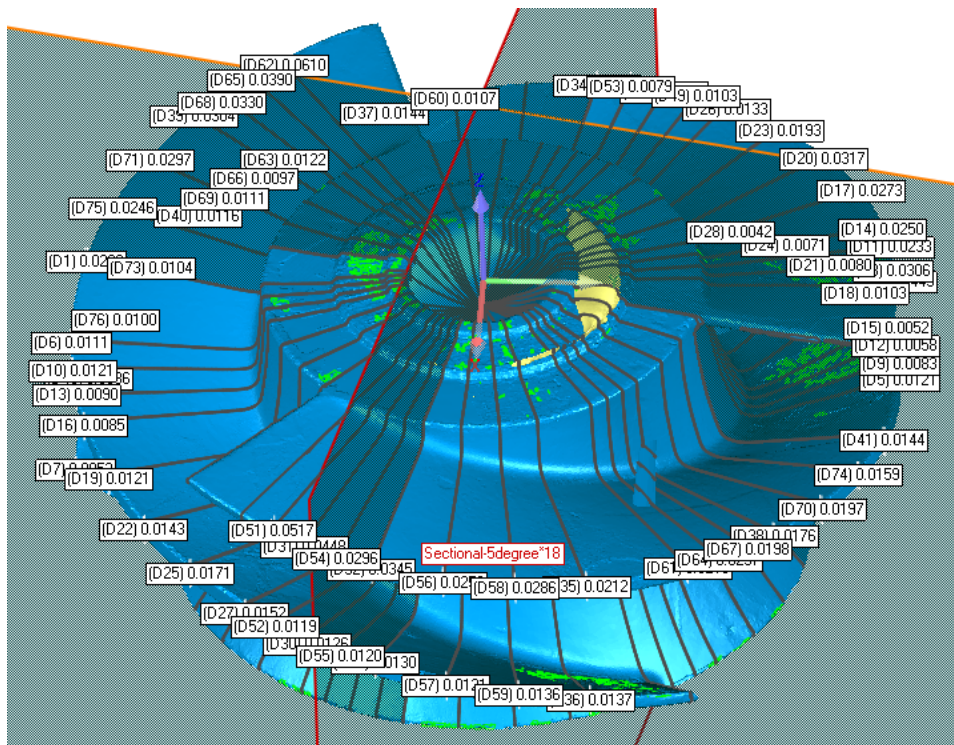


Figure 67: Measurement of the Wear on the Aligned Impellers

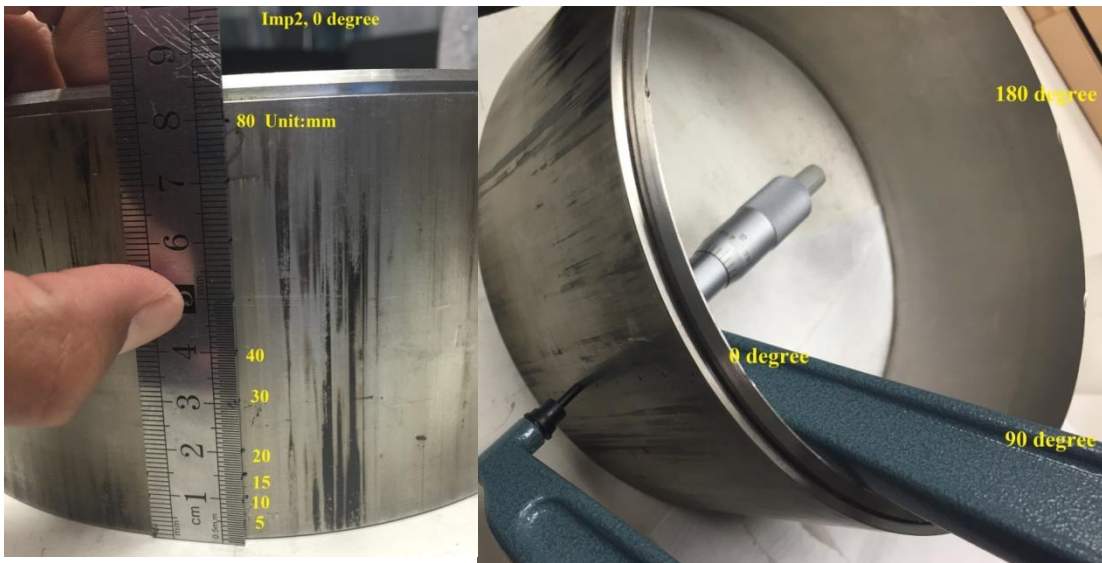


Figure 68: Measurement of the Thickness of Impeller Housing

In order to know the variance of the tip clearance (distance between impeller blade tip and impeller housing), the axial thickness of the impeller housing is measured (**Figure 68**).

In **Figure 70**, the thickness of metal loss of the impeller housing and impeller tip is plotted along the axial direction. At the top of the plot is the schematic view of the impeller blade and impeller housing, which is picked from **Figure 69**. The axial location of the leading edge of a new impeller is designated to be zero, so the blade tip of the eroded impeller is not measurable near $x=0$ mm. (For impeller 2, the quality of image processing is not good enough, so it is removed.) Wears of the tip and housing at the same stage are plotted in the same color. Obviously, the overall increase of tip clearance

is larger in the downstream stage, and the tip clearance is getting smaller downstream of an impeller.

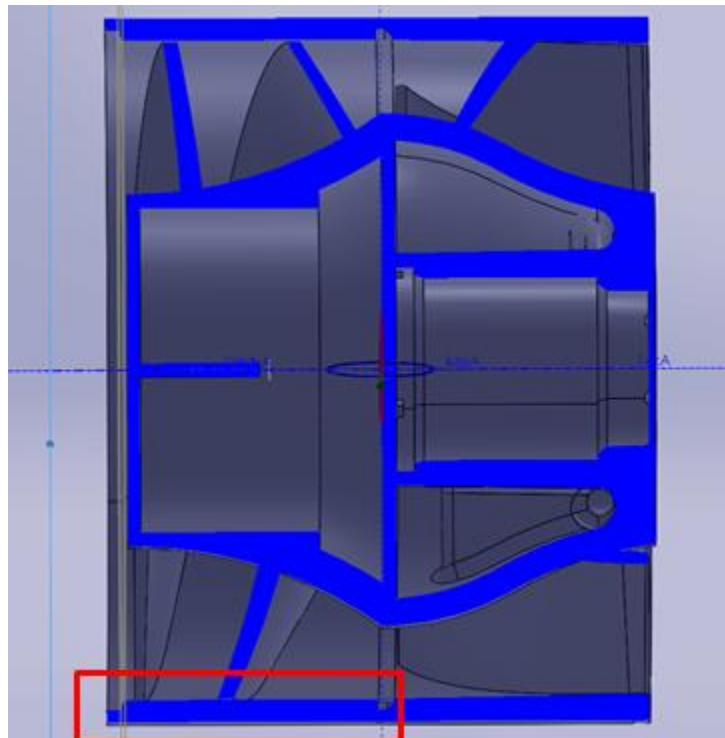


Figure 69: Sectional View of the 1st Stage Assembled

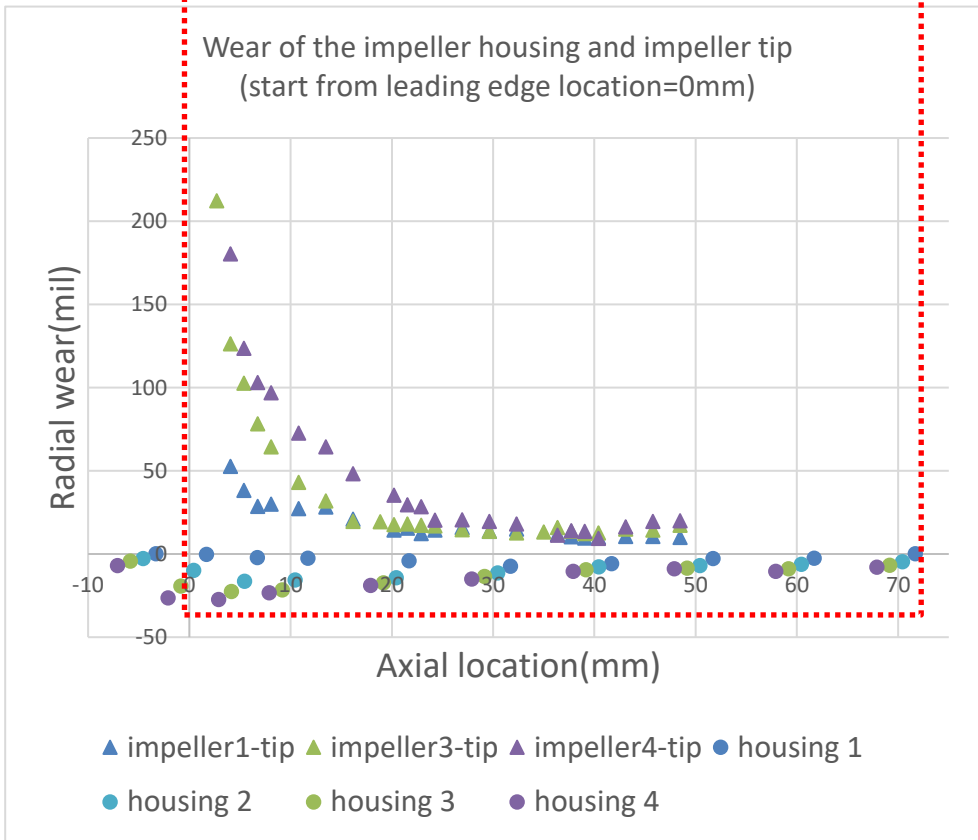
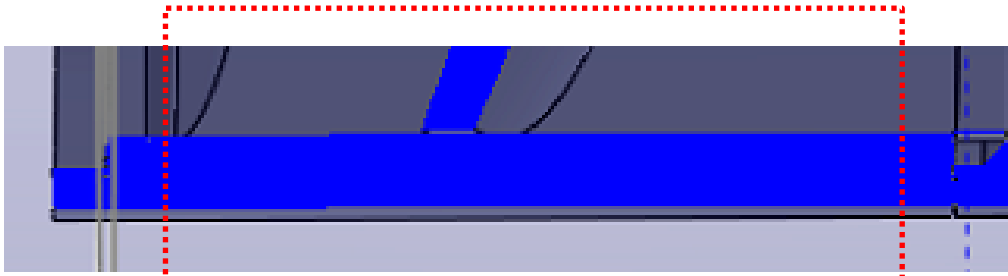


Figure 70: Measurement of the Wear at the Blade Tip and Impeller Housing

4.1.4 Wear of the Leading Edges

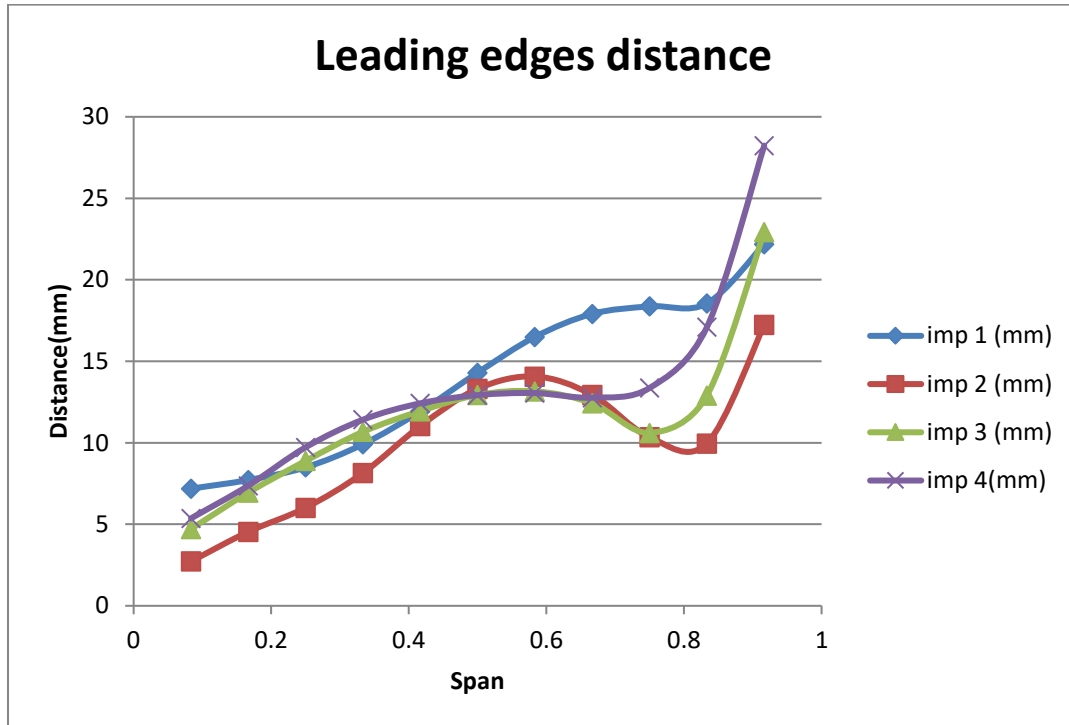


Figure 71: Distance between Leading Edges of the New and Eroded Impellers.

The loss of thickness at the leading edge of each impeller is the most significant wear that is observed. In **Figure 71**: the wear is measured between the leading edge surfaces of new and eroded impellers according to **Figure 50**. For the eroded impeller at the 1st stage, the shape of the profile is obviously different with the other 3 impellers. This could be explained by the different flow regime and particle distribution at the inlet. For the 1st impeller, there is no diffuser in the upstream. While for the next three stages, the inlet flow regime of each impeller is adjusted by the diffuser in the last stage.

Considering the next three impellers, the wear at the leading edge of the impeller is more severe at the downstream stage. This trend is also seen in the tip clearance wear of each stage.

4.1.5 Weight Loss of Each Stage

According to the measurements above, it is easy to explain the weight loss of the impeller and impeller housing shown in **Figure 72**, **Figure 73** and **Figure 74**. For the 4th diffuser, there is no impeller after its outlet, which has reduced its weight loss.

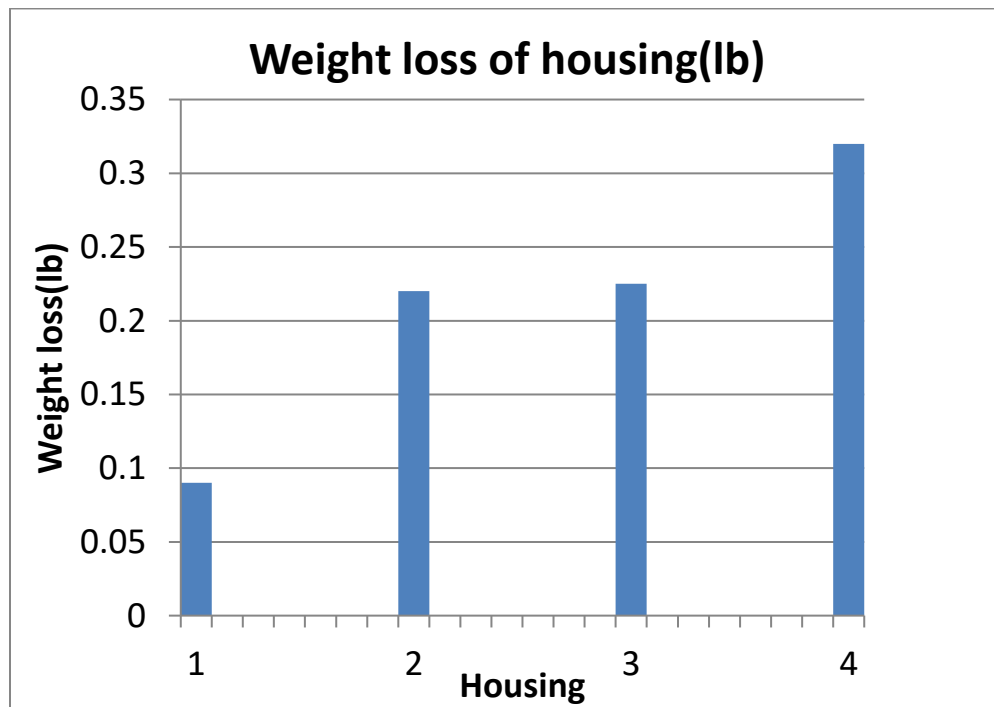


Figure 72: Weight Loss of each Impeller Housing

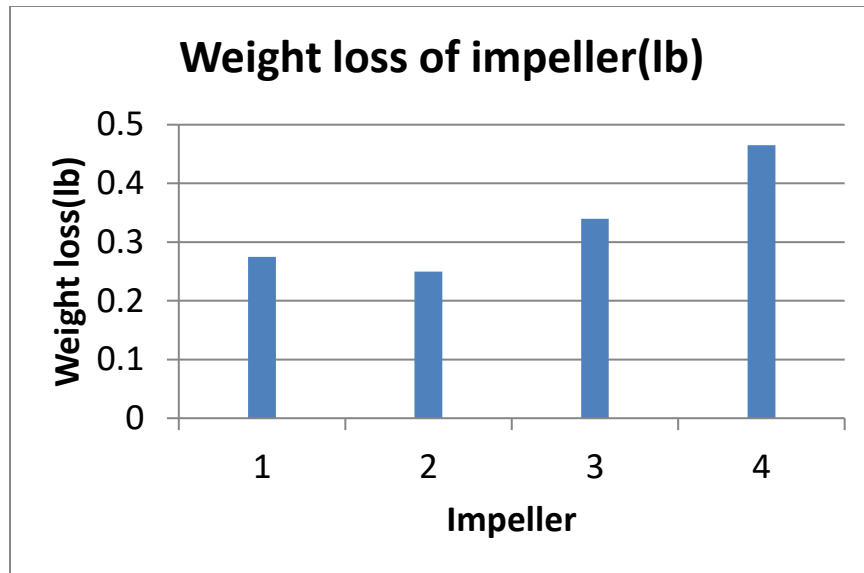


Figure 73: Weight Loss of each Impeller

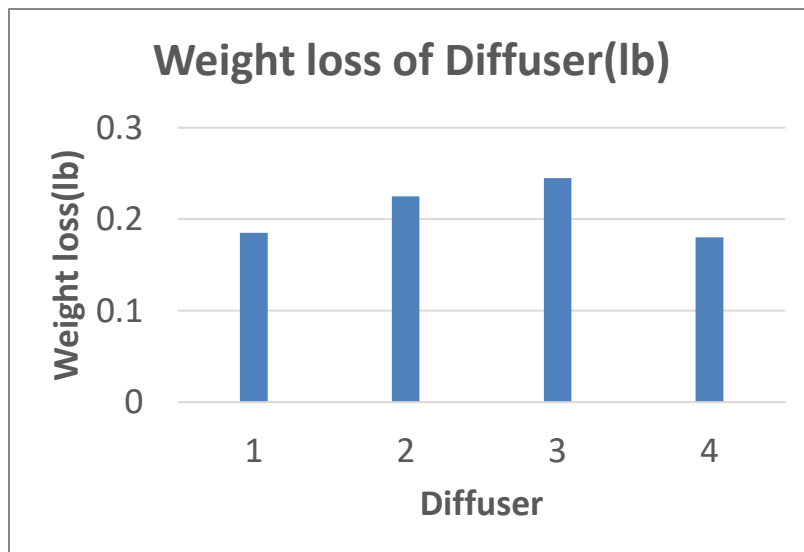


Figure 74: Weight Loss of each Diffuser

4.2 Pump Performance Change

4.2.1 Overview of the ESP Performance Change at Erosion Condition

As is mentioned in 3.2.2, some issues of the data need to be solved. In this section, “C” appears in the plots means the value has been “corrected” to be the real value in the test. “M” means the value has been modified (based on the tested value) to be the value when the 4th diffuser is not rotating. (The process of the correction is shown in Appendix)

Figure 75 presents the static pressure measured by the pressure sensors at each inlet and outlet. The value of PT5 at stage 1 inlet is fixed at 40 Psi in 200 hours. However, it cannot truly represent the inlet pressure due to the questionable location of the sensor. Thus, the pressure measured at the bottom tee near air inlet is used as the inlet pressure of the ESP.

In order to know the performance change of the ESP, the pressure rise of each stage is plotted in **Figure 76**. For the same liquid flow rate, higher GVF will always cause a lower pressure rise of a pump. The inlet GVF of each stage goes down, so the pressure rise of each stage goes up. In addition, each stage has a slight pressure drop during the 200 hours. In order to compare the head ratio loss stage by stage, **Figure 77** plots the percentage of the pressure rise (or head ratio) of each stage. The 1st stage is special and has around 25% head loss. The 2nd and 3rd stage has 10% head loss, and the 4th stage (modified) has 17% head loss which has the most erosion loss of thickness.

When considering the head of the multistage pump, it is better to be cautious when viewing the compressible mixture condition. Although the inlet GVF of the 1st stage is constant, the exact inlet GVFs of the other stages will increase due to the head loss of the stages at its upstream. In this case, the head loss of the 1st stage will increase the inlet GVF at the 2nd stage and reduce the head of 2nd stage. So the wear on 2nd stage and head loss of the 1st stage are both contributions of the 2nd stage head change. In order to avoid the GVF effect on performance loss of each stage, it is better to consider the case with water only.

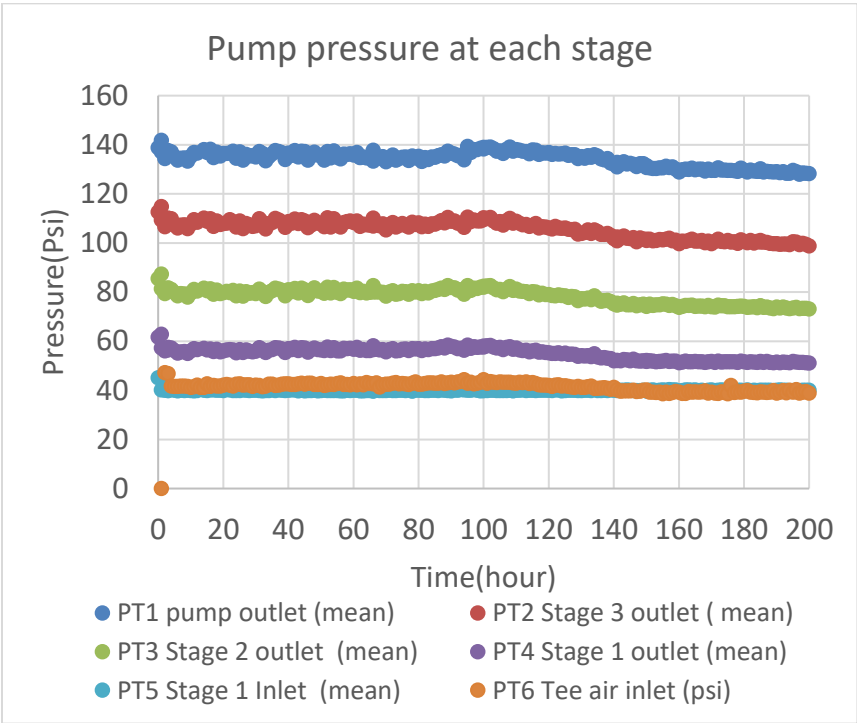


Figure 75: Static Pressure Measured at Different Location during the 200-Hour Test

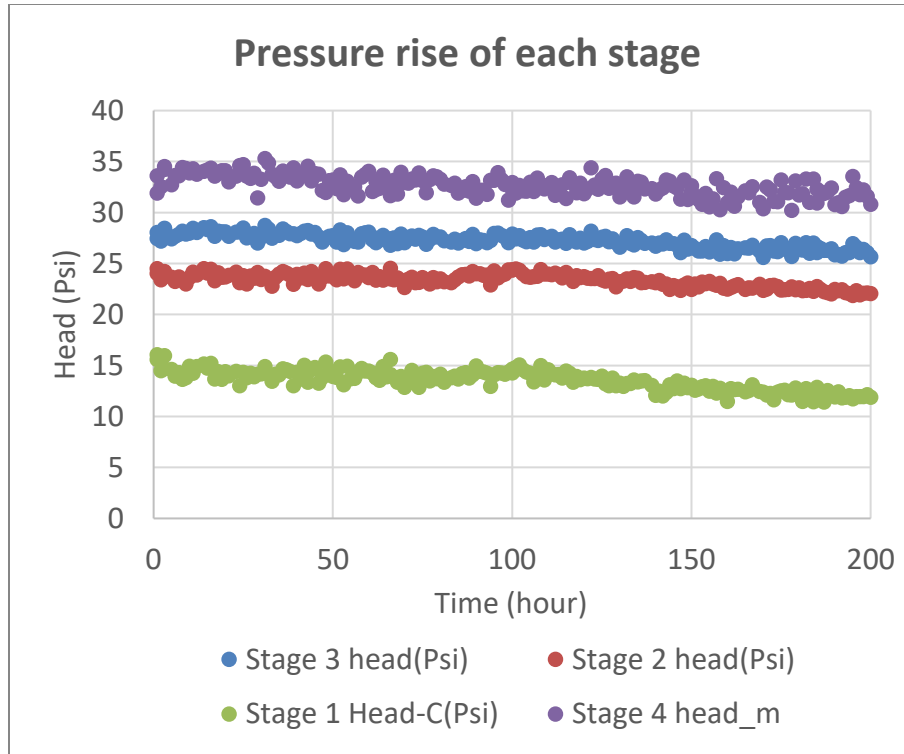


Figure 76: Pressure Rise of each Stage during the 200-Hour Test

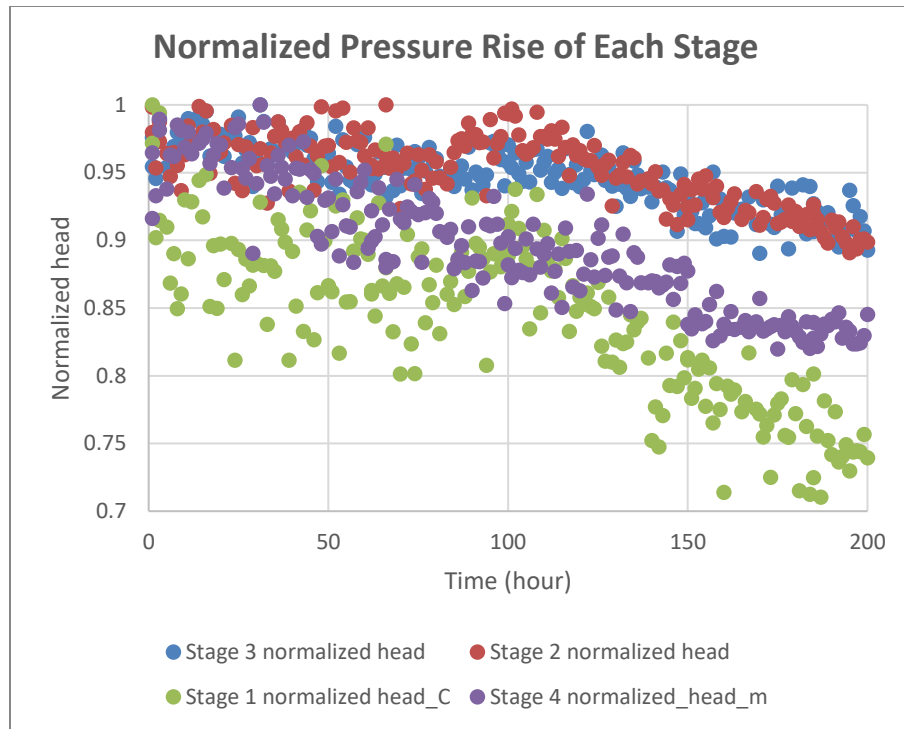


Figure 77: Normalized Pressure Rise during the 200-Hour Test

4.2.3 Performance Curves Movement in 200 Hours

Figure 78 to **Figure 82** compare the pump performance at the 0th and 200th hour. Stars and circles are the tested points in the 0th hour performance test. Diamonds and squares are the tested points in the 200th hour performance test. Each solid line stands for the 0th hour performance curve, while each dashed line stands for the 200th hour performance curve. Those curves are generated by polynomial fitting based on the tested points. The left end of each curve is limited by pump surge, while the right end is limited by pressure loss in the loop. The X-axis is the liquid volume flow rate instead of the mixture volume flow rate. GVF always stands for the inlet GVF of the 1st stage. **Figure 78** and

Figure 79 compare the performance maps of the overall head and efficiency before and after erosion test. The efficiency is calculated by equation(20):

$$\eta = \frac{(P_{out} - P_{in}) * Q_{water} + P_{in} * Q_{air,in} * \log(P_{out}/P_{in})}{I * U} \quad (20)$$

Figure 80:**Figure 80, Figure 81** and **Figure 82** compare the head-Q curves of each stage before and after erosion test. No matter what stage, at what GVF, a common result is that the performance loss is greater at lower flow rate.

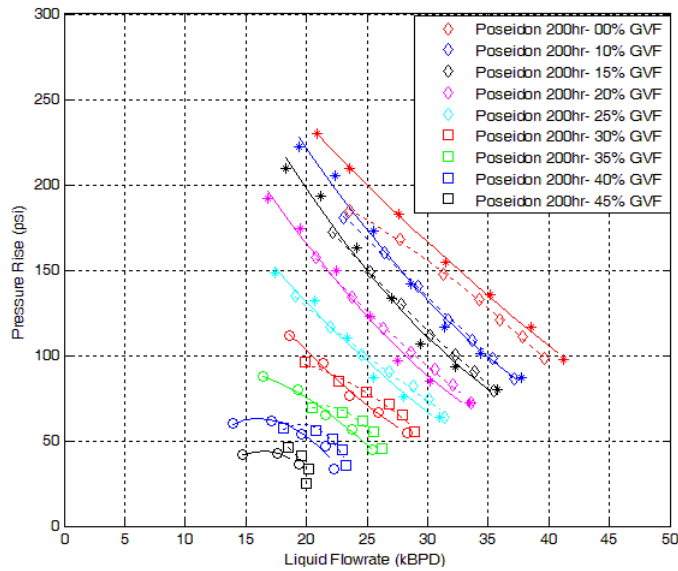


Figure 78: Total Pressure Rise at the 0th and 200th Hour

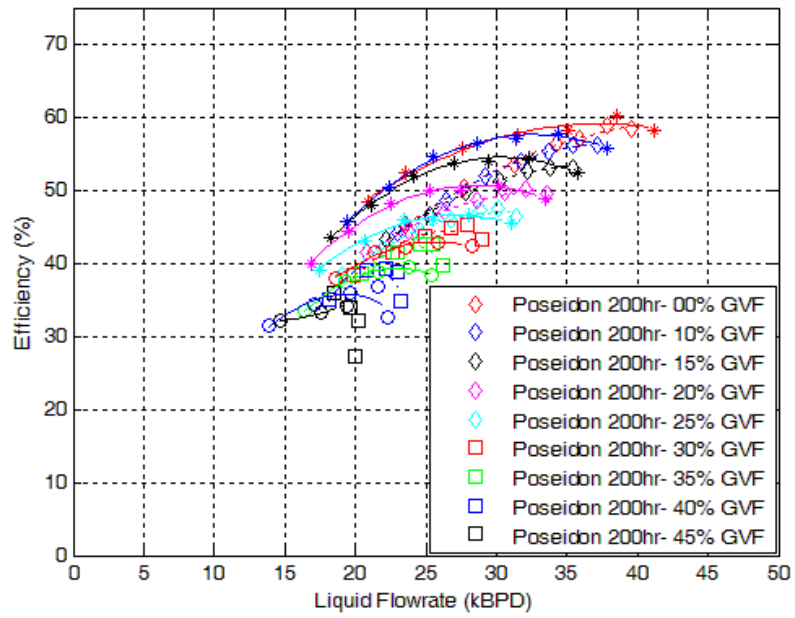


Figure 79: ESP Efficiency at the 0th and 200th Hour

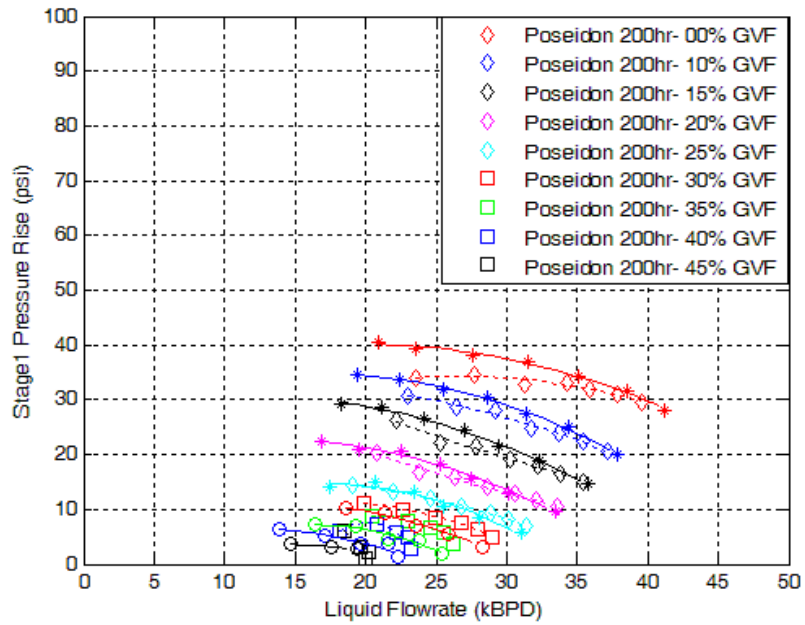


Figure 80: 1st Stage Pressure Rise at the 0th and 200th Hour

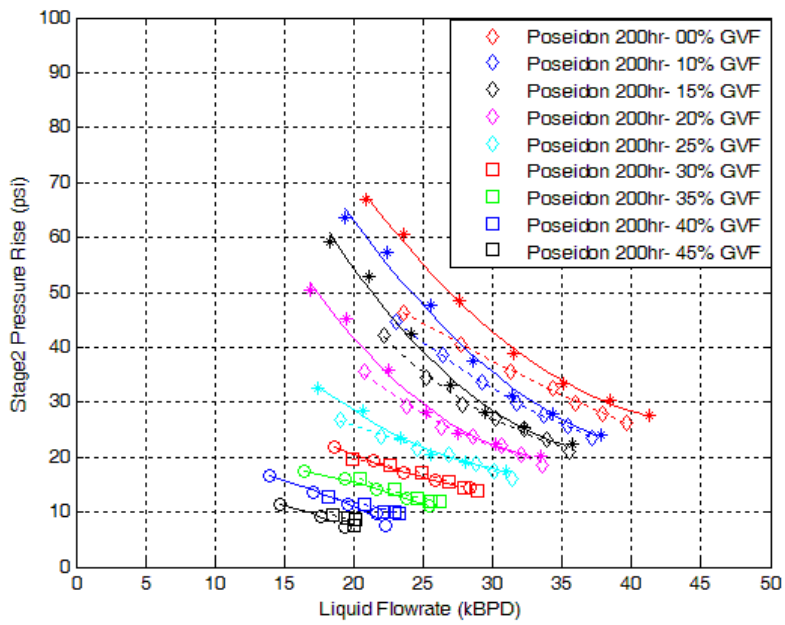


Figure 81: 2nd Stage Pressure Rise at the 0th and 200th Hour

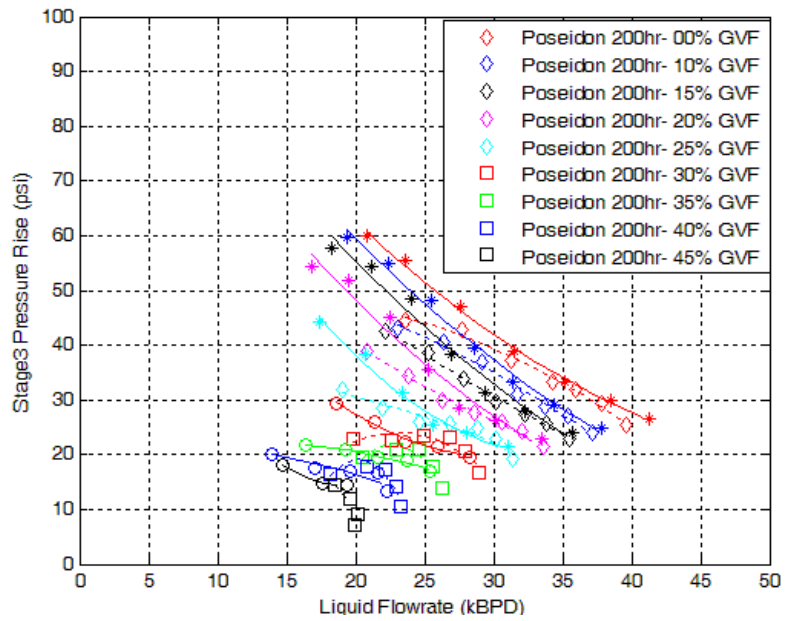


Figure 82: 3rd Stage Pressure Rise at 0th and 200th Hour

To learn how much percentage the parameters have changed, plots present curve function of 200th hour over that of curve function of 0th hour (**Figure 83** to **Figure 86**). Obviously, the head loss ratio or the efficiency loss ratio has a negative correlation with GVF and liquid flowrate. Considering the loss of thickness of the impeller in Chapter 4.1, the head loss is caused by the increase in tip clearance, which leads to greater internal leakage. Then, these two negative correlations can be explained by the reduced leakage due to lower pressure rise. Considering the error in curve fitting, the exact values of some points in the curve might not accurately represent the real values, but the trend of these curves can still be used to study the performance change due to the erosion. The 1st stage is special but it also has the similar trends. Only the performance curves at the same inlet GVF of the target stage is comparable. Therefore, the curves at non-zero GVF in **Figure 84** and **Figure 85** cannot directly prove the negative correlation of head loss ratio and GVF, but this result could be acquired through further analysis.

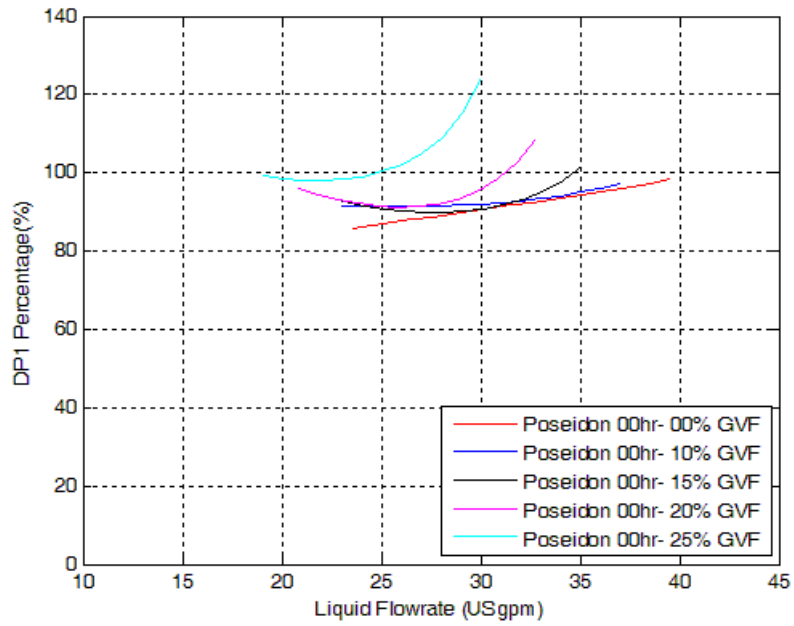


Figure 83: Performance Map, 1st Stage Pressure Rise Ratio at the 200th Hour

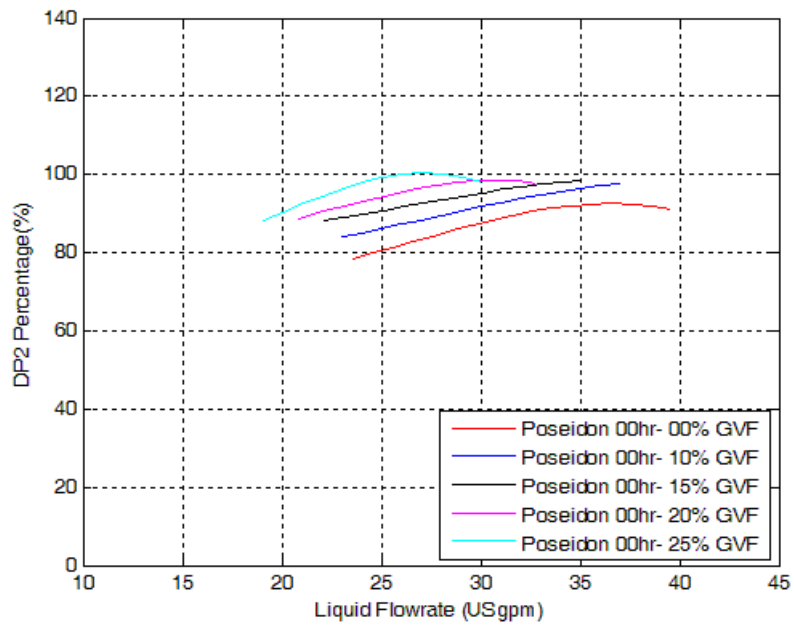


Figure 84: Performance Map, 2nd Stage Pressure Rise Ratio at the 200th Hour

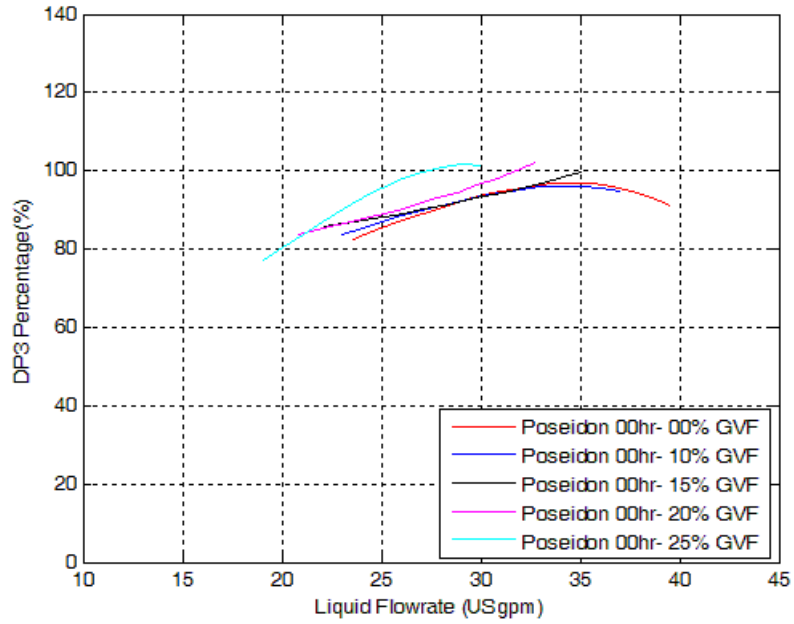


Figure 85: Performance Map, 3rd Stage Pressure Rise Ratio at the 200th Hour

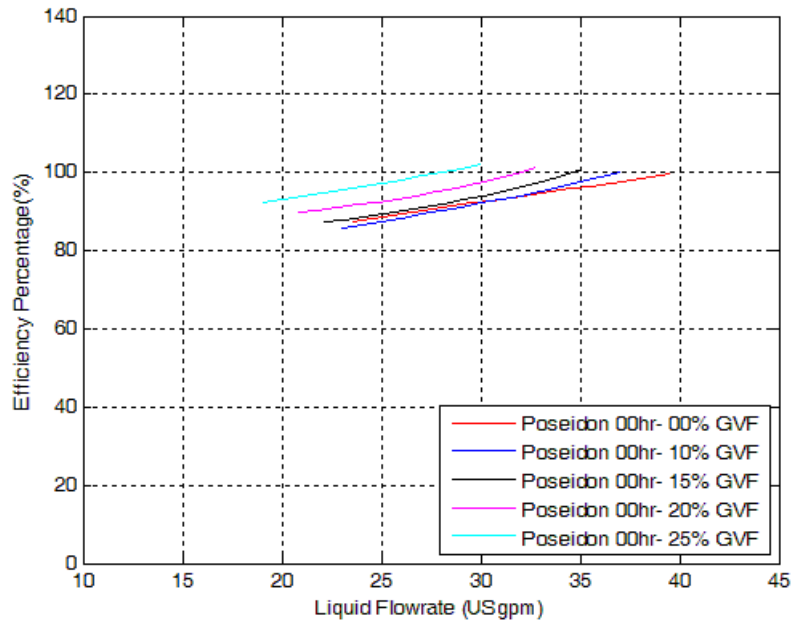


Figure 86: Performance Map, Efficiency Ratio at the 200th Hour

To have a direct proof of the head loss at each stage caused by erosion only, the test points collected every 50 hours from performance tests are plotted in **Figure 87, Figure 88, and Figure 89**. The lines here are just connecting the points. The Head-Q map of the 1st stage is always different with other stages. But the movement of its performance curve due to erosion is similar to other stages. The head loss of the each stage is getting larger at lower flowrate, which is indicative of larger internal leakage due to larger pressure difference between the pressure side and suction side. The measurement of each point might have been affected by the pressure fluctuation in the loop. For example, the 1st stage, the head of 34kBPD flowrate at 150th hour is smaller than that at 200th hour. This fluctuation is acceptable and could be reduced by curve fitting. But it affects the accuracy in evaluating the head ratio loss which is important in inspecting the GVF effect on head loss caused by erosion.

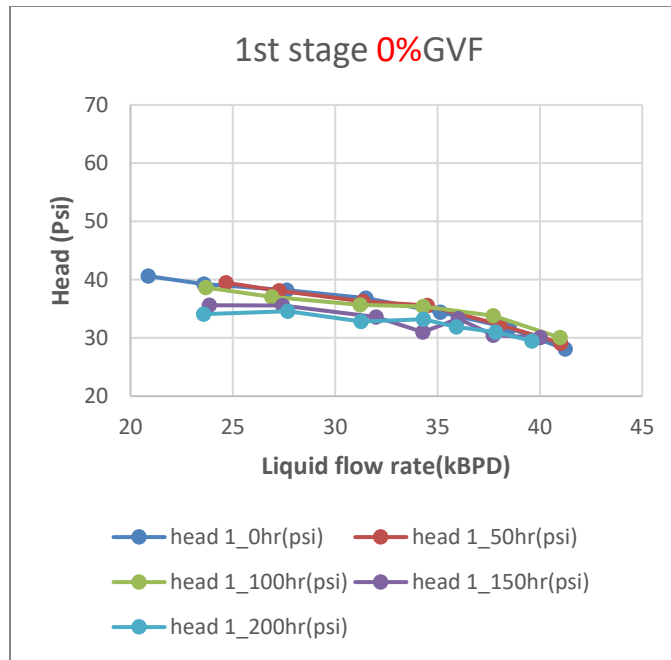


Figure 87: Performance Curves of the Head at 1st Stage Every 50 Hours.

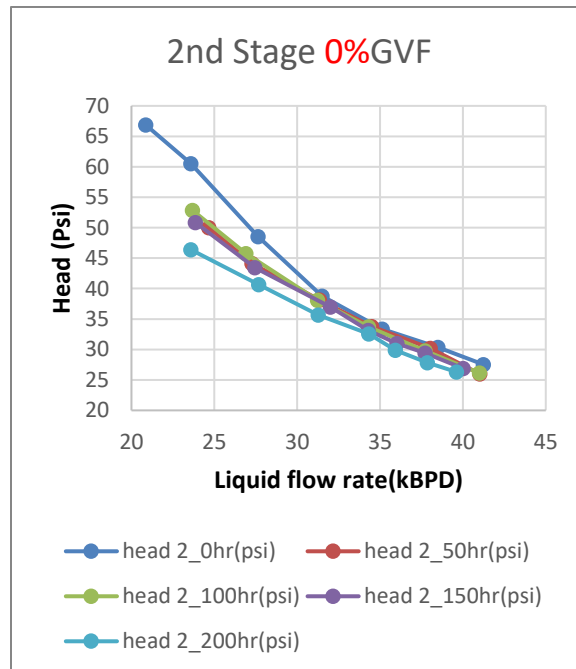


Figure 88: Performance Curves of the Head at 2nd Stage Every 50 Hours.

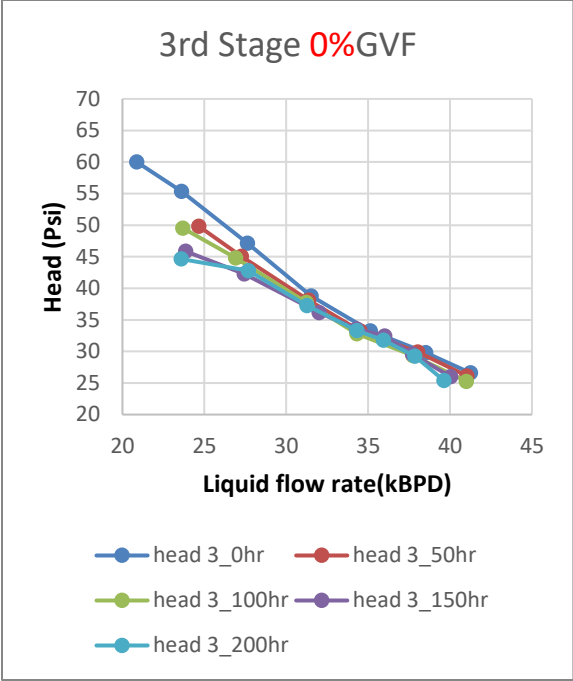


Figure 89: Performance Curves of the Head at 3rd Stage Every 50 Hours.

4.3 Numerical Simulation on the Pump

4.3.1 Performance Map (Single-Phase)

This section will discuss the single phase simulation of the 1st stage. According to the grid/time independence study in a previous section, the time step is set at 0.25 degree/step and the mesh with 3.15 million elements is used. Assumptions and simplifications for single phase simulation are shown below:

1. Instruments like proximity probes, pressure sensors are removed
2. Geometry of the impeller and diffuser from centerline to hub is simplified
3. The wear in axial direction of the diffuser spacer is averaged
4. The wear of diffuser does not affect the performance of the ESP
5. Temperature is constant everywhere
6. No air dissolved in the water
7. Ignore the eccentric effect caused by vibration of the impeller
8. The area-weight average pressure on the sectional surface represents the inlet or outlet pressure of the pump
9. The mass flow rate at the 1st stage inlet is even

Table 7: CFD Boundary Condition for Single-Phase Simulations

ESP	Water Flow Inlet(GPM)
Original, 1 st stage	583
Eroded, 1 st stage	700
	880
Pressure outlet	1000
65 Psi	1100
	1200

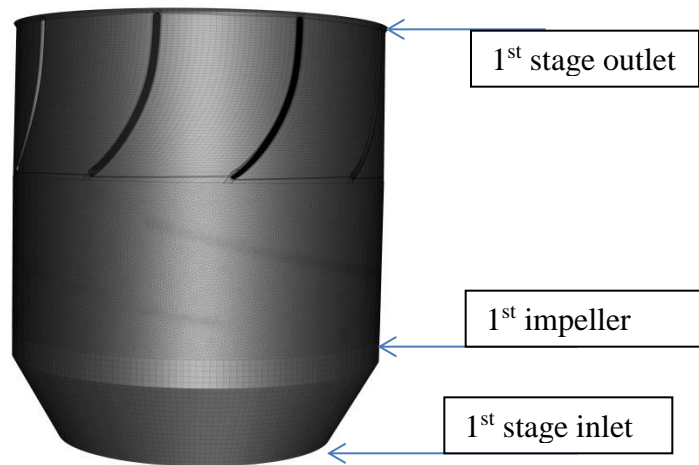


Figure 90: Grid for 1st Stage Performance Simulation

For incompressible flow, the mass flow inlet of the 1st stage can be regarded as uniform. Considering that the inlet flow regime would be affected by the 1st impeller, simulation is performed on the 1st stage connecting with an inlet body. **Figure 90** shows the grid of these aligned geometries. It also points out the difference between the impeller inlet and stage inlet chosen in CFD simulation. Without adding the whole bottom tee, it saves the calculation hours. **Table 7** presents the boundary conditions for these single-phase simulations. All the simulations applied k-epsilon Model, Realizable, and standard wall function.

Figure 91 compares the performance curves collected in the performance test and calculated in the CFD simulation. For the new pump, the CFD simulation nicely captures the curve in the test. For the eroded pump, the simulation has a good match at lower flow rate, but it gradually underestimates its head when flow rate is increased. The

assumptions and simplifications mentioned above might have caused the underestimation. In short, the overall single-phase simulations have still captured the head loss of the 1st stage, though roughly.

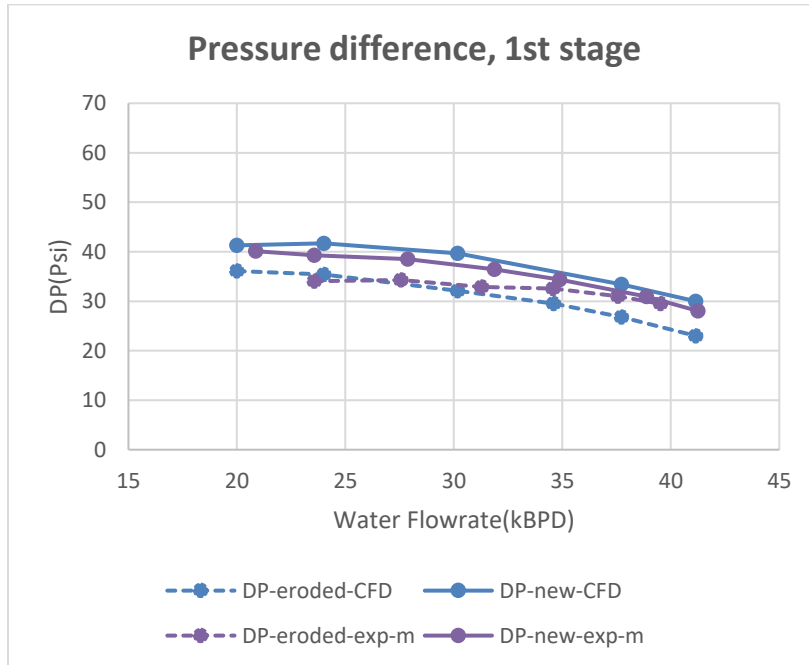


Figure 91: Comparison of the Head-Q Curves for the 1st Stage

Figure 92 plots the contour of location in the Z direction. It points out the axial locations of the plots in **Figure 93** and **Figure 94** for the 1st stage. **Figure 93** plots the area-weight average pressure for every 0.5 inch in the axial direction. Both the new and the eroded pumps are considered. Because of the better prediction of the head at lower flowrate, the cases with flowrate of 20kBPD (583gpm) are analyzed. Thanks to the incompressible flow, the pressures at the inlet ($z=-2$ inch) for these cases are unified to 37.2psi (originally the pressure outlet of all cased are all the same). The pressure of each case

keeps rising in the impeller (0 inch to -2.5 inch), drops a little at the interface between impeller and diffusers(-3 inch), and then slightly rises at the end of the diffuser.

Moreover, most of the pressure rise happens in the impeller. **Figure 94** presents the deduction of the pressure calculated in the new and the eroded pump. The pressure in the impeller(-2.5inch to 0 inch) is constantly increasing, while the most pressure loss due to erosion happens in the 1st 0.5 inch(-0.5inch to 0inch) where the main material loss happens (**Figure 70 and Figure 71**). Therefore, the simulation can capture the pressure loss reasonably. It clearly describes how the metal loss caused by erosion affects the performance of the 1st stage. However, it is still not clear which one determines the head loss, the wear at leading edge, or the wear at the tip, or both.

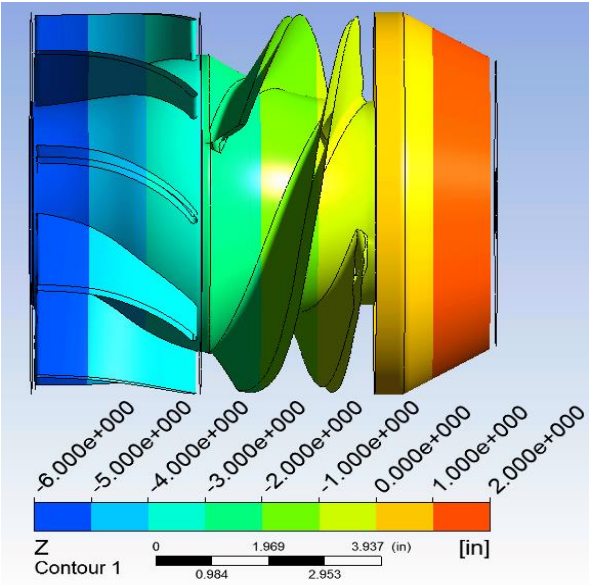


Figure 92: Schematic View of the Axial Location on the 1st Stage

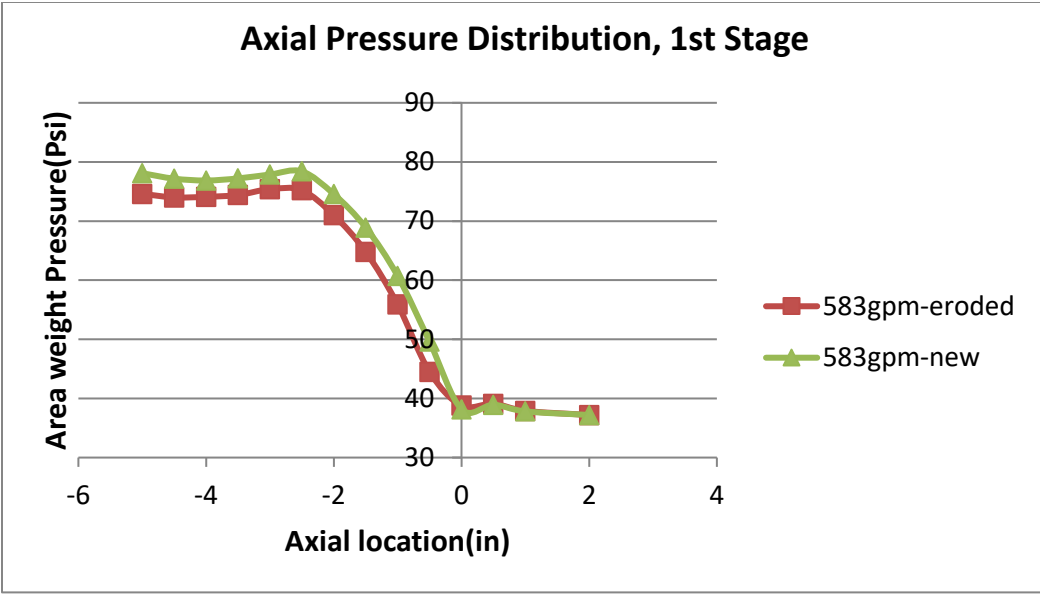


Figure 93: Axial Pressure Distribution in the New and Eroded Pump in CFD Simulation

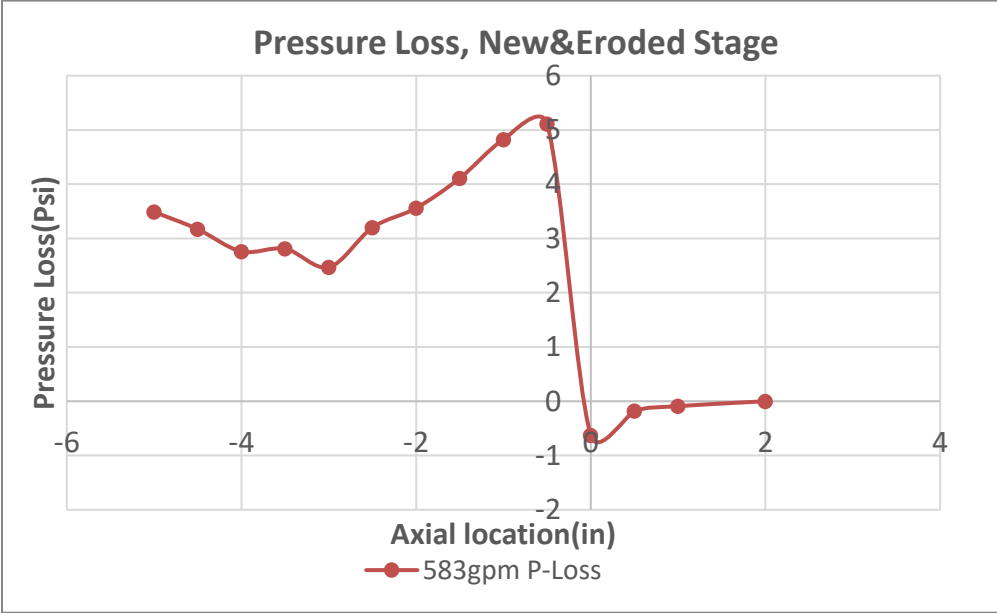


Figure 94: Axial Pressure Loss in the New and Eroded Pump in CFD Simulation

4.3.2 GVF Distribution at the Interfaces (Two-Phase)

In order to predict the erosion rate of the pump, a three-phase simulation of the erosion condition with gas and sand is necessary. However, it is too complicated and time-consuming to directly perform a three-phase simulation. Thus, some simplifications and assumptions were made by referring to the two-phase simulation.

It is not easy to “describe” the inlet condition of the 1st stage inlet due to the uneven GVF distribution at the stage inlet. Therefore, the bottom tee and the mixer body are simply meshed and connected to the 1st stage in the simulation. **Figure 95** presents the whole geometry, and **Figure 96** is the mesh based on the simplified geometry. **Table 8** lists the boundary conditions and other related settings.

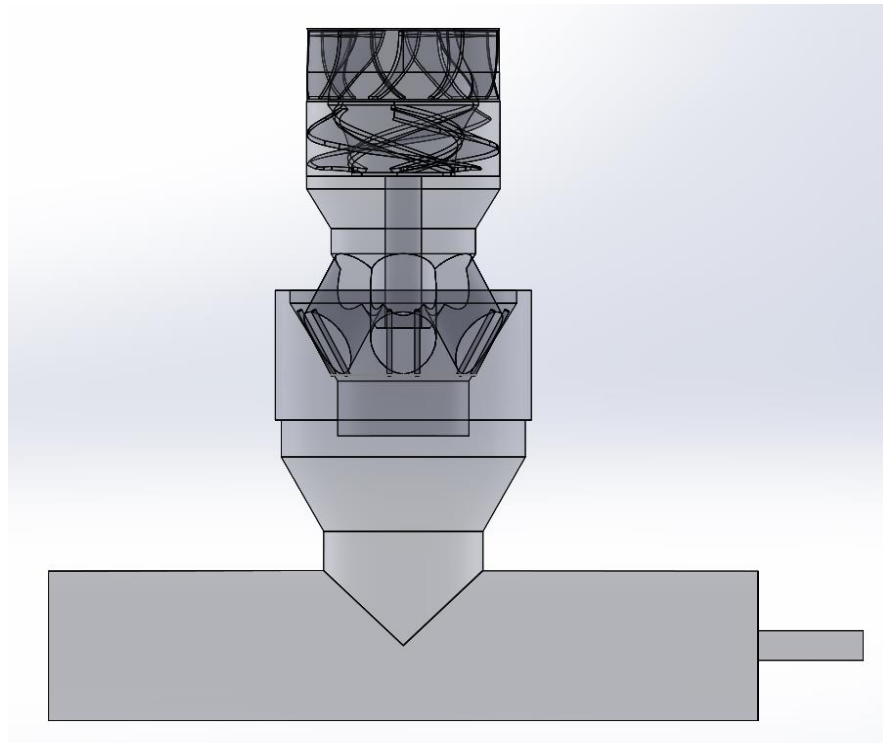


Figure 95: Front View of the Whole Geometry

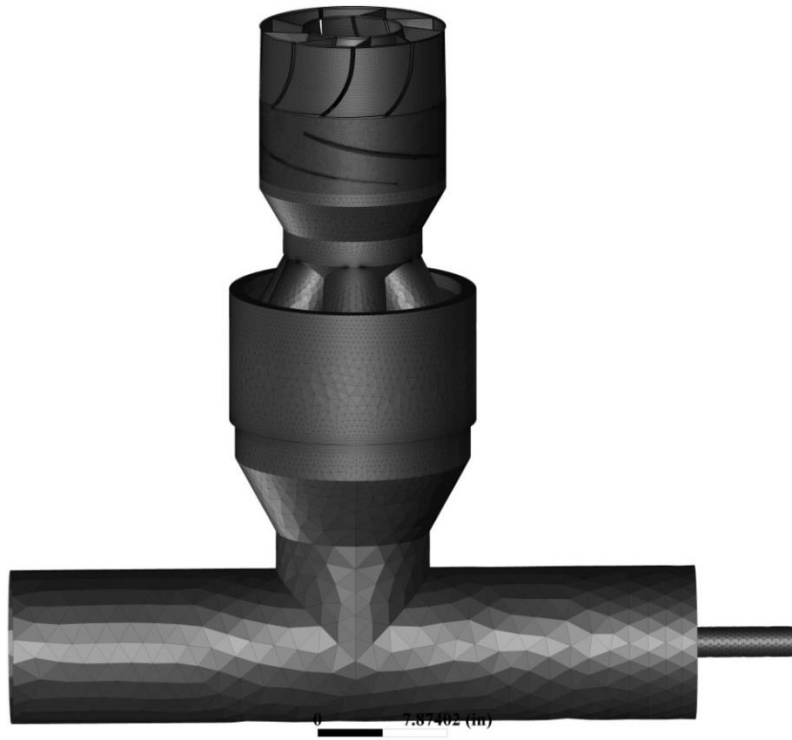


Figure 96: Mesh of the 1st Stage with the Bottom Tee Connected

Table 8: Parameters Setting and Model Selection for 2-Phase Simulation

Parameter/Model	Setting
Mass flow inlet-water	55.0kg/s
Mass flow inlet-air	0.056 kg/s
Pressure outlet	60 Psi
Angular speed	3600 RPM
Air density	4.9kg/m ³
Water-air Drag	Schiller-Naumann
k-epsilon Model	Realizable
Water-air (multiphase)	Eulerian-Eulerian
Turbulence Multiphase Model	Mixture
Near-Wall Treatment	Standard wall function
Lift	none

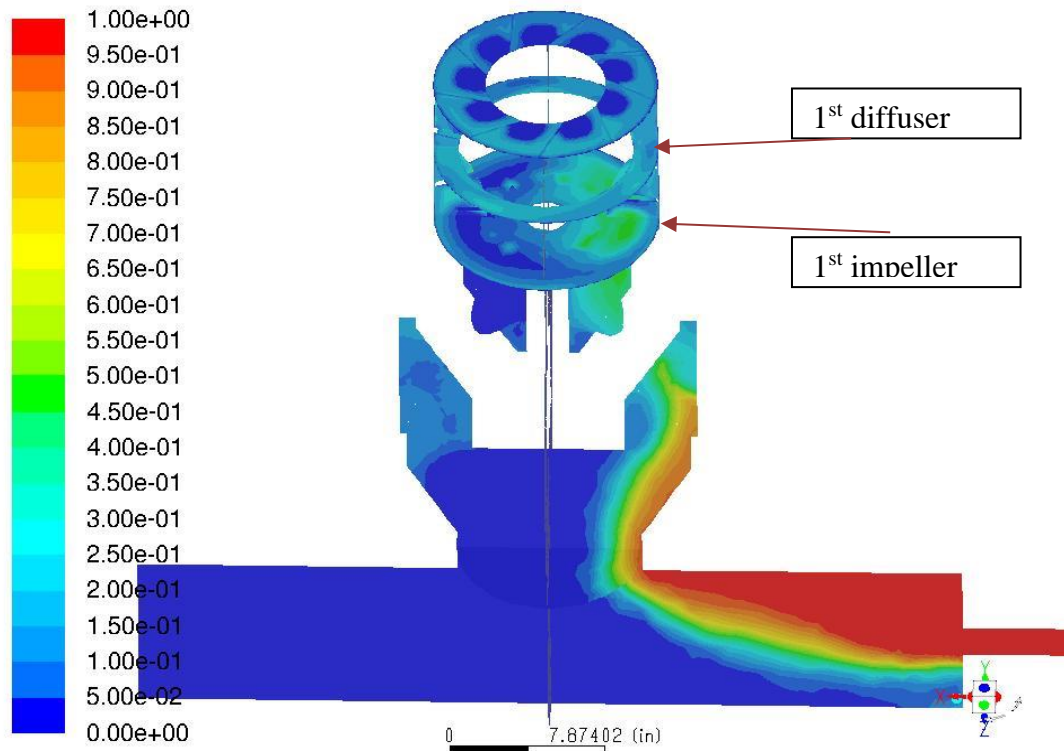


Figure 97: GVF Distribution at Certain Cross-Sections, 20% GVF Inlet

Figure 97 shows the GVF at the 1st impeller inlet, 1st diffuser inlet, and 1st diffuser outlet. The GVF is not even at 1st impeller inlet due to the geometry of bottom tee. However, at the 1st diffuser inlet, the unevenness of air distribution has been greatly reduced. Although the GVF is not evenly distributed at each outlet of the diffuser channel, the nine diffuser channels have similar GVF. In this case, if we perform the simulation on the 1st diffuser and 2nd impeller with an evenly distributed GVF at diffuser inlet, it can be assumed that the GVF distribution at the inlet of the 2nd impeller is close to the “real condition.” This assumption is also verified by S. Reddy [43]. If analyzing the 1st stage, it is necessary to simulate on the whole flow field in **Figure 95** and **Figure 96**. Therefore, performing the erosion simulation on the 2nd impeller results in more uniform inlet GVF than on the 1st impeller.

Although this two-phase simulation does not apply the ideal gas model, the prediction of the pressure distribution can still be used for reference due to the lower compress ratio at a relatively higher pressure. **Figure 98** and **Figure 99** present the pressure distribution and blade loading of the 2nd impeller at span=0.98. This is the location of the blade tip. At the pressure side, the pressure rise mainly happens at the first 1/3 of the impeller blade while at the suction side, the pressure rise is evenly distributed (**Figure 98**). This causes a big pressure difference between the suction side and the pressure side at the first 1/3 of the impeller (**Figure 99**). Therefore, the leakage will be greater at this area and leads to greater erosion and larger tip clearance which is observed in **Figure 70**.

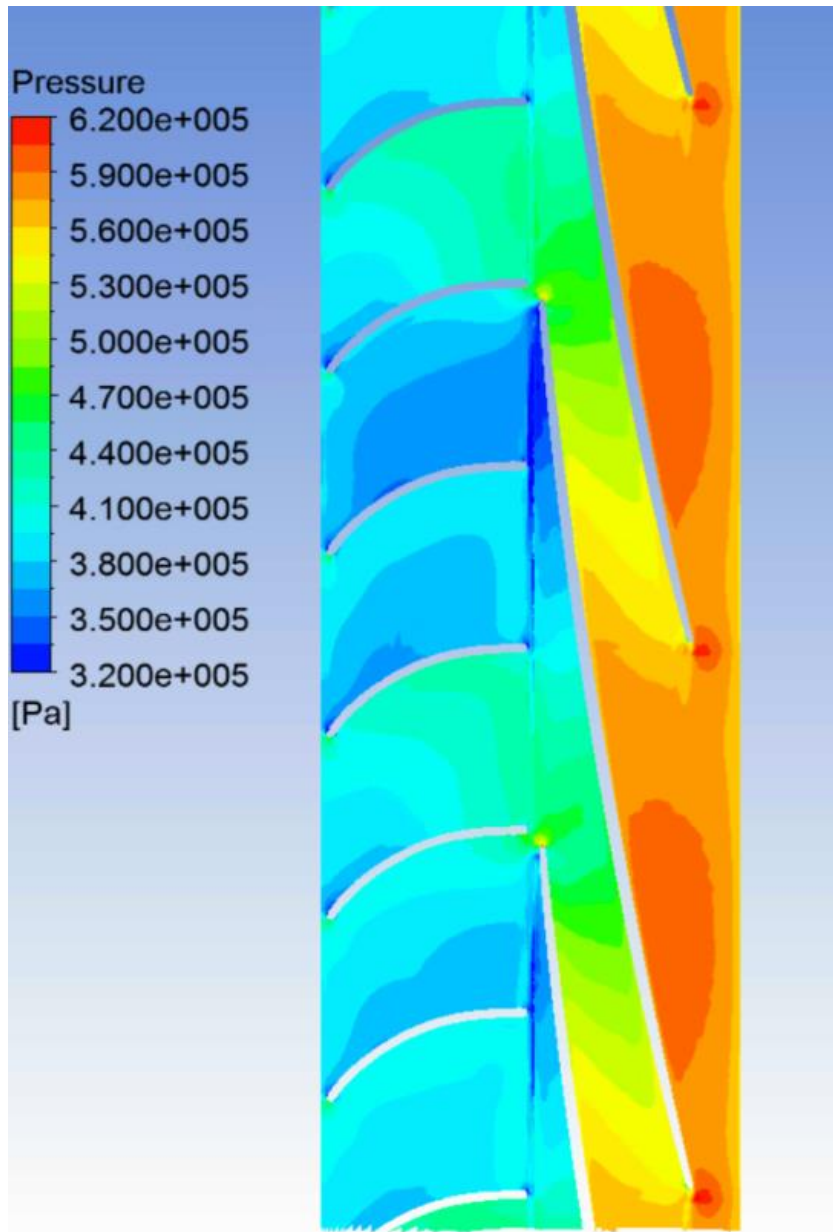


Figure 98: Blade to Blade Pressure Distribution of 2nd Impeller at Span=0.98

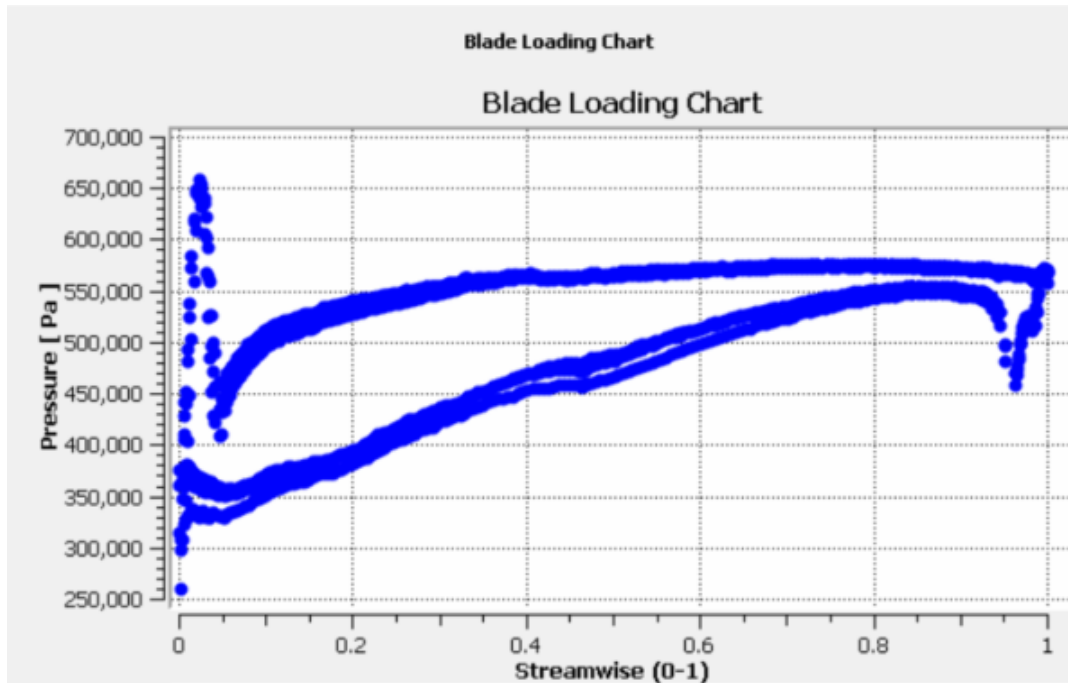


Figure 99: Blade Loading of 2nd Impeller for Pressure at Span=0.98

4.3.3 Erosion Model for Predicting Erosion Rates (Three-Phase)

In this section, a CFD erosion model is created according to the erosion related parameters from the three-phase simulation. In addition, it is calibrated by the loss of thickness measured on the impeller.

After weighing the balance between the trueness and simulation hours, the 2nd impeller is chosen to analyze the erosion rate, and the 1st diffuser is used to create a GVF distribution inlet for the 2nd impeller. After this simplification, the geometry size and the element number have been reduced significantly. Grids of the new impeller and new diffuser are aligned and connected (**Figure 100**).

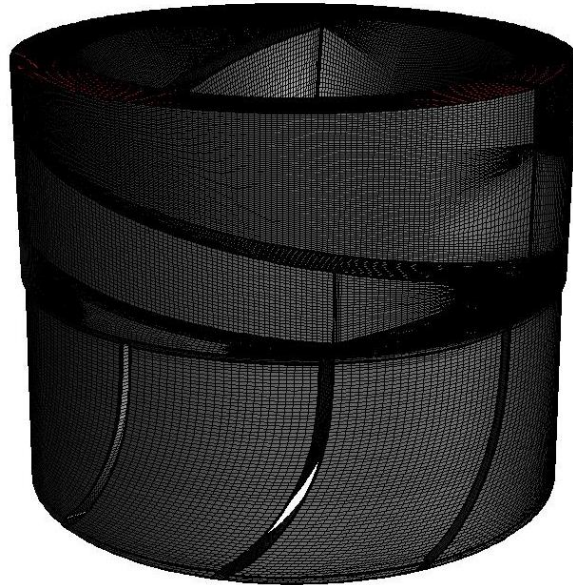


Figure 100: Grid for the 3-Phase Simulation Inspecting the 2nd Impeller

The assumptions and simplifications for the three-phase simulation are as follows:

1. Instruments like proximity probes, pressure sensors are removed
2. Geometry from centerline to hub is simplified
3. Slip velocity (air and water) is not large
4. Bubble size is constant
5. Diameter and density of sand are constants
6. Temperature is constant everywhere
7. Ignore the eccentric effect caused by vibration of the impeller
8. GVF and sand concentration is evenly distributed at the inlet of the 1st diffuser
9. Bubble size is constant[43]

Table 9: Boundary Conditions and Other Parameters for 3-phase Simulation

Parameter	Value	Unit
Mass flow inlet-water	55.0	kg/s
Mass flow inlet-air	0.056	kg/s
Mass flow inlet-sand	0.133	kg/s
Pressure outlet	80	Psi
Angular speed	3600	RPM
Bubble size	10e-4	m ³
Sand size	0.0159	in

Table 9 lists the boundary conditions and other parameters specified in this three-phase simulation. During the simulation, the third phase is not added until the two-phase flow field is stabilized. When adding the sand, the DPM (discrete phase model) has been applied. When the three-phase simulation is stabilized, the erosion module is applied to calculate the impact angle, impact rate (sand flush rate), and impact velocity. After obtaining these parameters, a calibration is performed to obtain the coefficients in the erosion model.

Assumptions and other details in erosion rate calibration are as follows:

1. Erosion happening at the leading edge of the impeller is a periodical process, and its period is decided by diffuser blade number and rotating speed (every 40 or 120 degrees)
2. Wear measured at the same radial location of the leading edge of each blade is averaged. (**Figure 70**, in Chapter 4.1)
3. According to **Figure 101**, 3x11 points between the tip and hub of each blade are considered in the calibration.

4. Impact erosion dominates the erosion on this pump, and it mainly happens at the leading edge of the impeller. (Only the impeller blade's leading edge is going to be used for calibration here.)

5. Equation (21) suggested by ANSYS[28] for predicting erosion is calibrated using the least square method.

$$E_R = c\dot{m}V_{sand}^n f(\alpha) \quad (21)$$

6. The Impact angle function developed by Y. Zhang [23] is applied here.

7. For the DPM simulation, all the particles are discrete. This will require the parameters in equation(21), which is for continuous phase, to change to be averaged terms for describing the discrete phase problem. Assuming in time Δt , there are $N(\Delta t)_{particle}$ particles impacting the surface with area A_{face} at impact angle α_p and impact velocity V_p . The averaged erosion parameters are defined in eq(22-25). If Δt is big enough, there will be enough particles impacting the area, which makes the time averaged parameter accurate enough to represent the parameters in a continuous case. Thus, eq(25) can represent Eq(21). In this study, assuming $\Delta t = 40$ degree/angular-velocity is big enough.

$$\bar{\dot{m}} = \frac{\sum_{p=1}^{N(\Delta t)_{particle}} \frac{m_p}{A_{face}}}{\Delta t} \quad (22)$$

$$\bar{V} = \frac{\sum_{p=1}^{N(\Delta t)_{particle}} \frac{m_p}{A_{face}} V_p}{\bar{\dot{m}}\Delta t} \quad (23)$$

$$\bar{\alpha} = \frac{\sum_{p=1}^{N(\Delta t)_{particle}} \frac{m_p}{A_{face}} \alpha_p}{\bar{\dot{m}}\Delta t} \quad (24)$$

$$\overline{E}_R = c\overline{m}\overline{V}^n f(\overline{\alpha}) \quad (25)$$

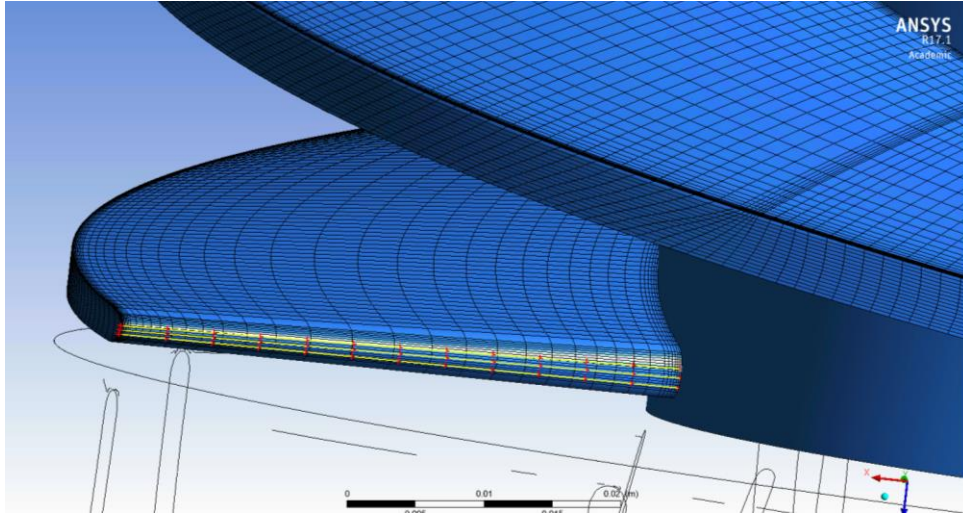


Figure 101: Points at the Leading Edge of Impeller Picked for Calibration (exclude two ends)

As is discussed above, the erosion related parameters are time-averaged. When the time exceeds the period mentioned above, the longer time it is simulated, the more accurate it will be. **Figure 102** to **Figure 105** show these time-averaged parameters when the impeller rotates 120 degrees. At the area with small sand flush rate, the time might not be enough to show the continuous distribution of the parameters, for example, the downstream area in **Figure 104**. Due to the characteristic of the erosion model which is an empirical formula (eq (21)), when calibrating the erosion model, all these parameters are non-dimensionalized by removing the unit shown in these pictures (directly divided by a reference parameter with the same unit, and the value equal to 1).

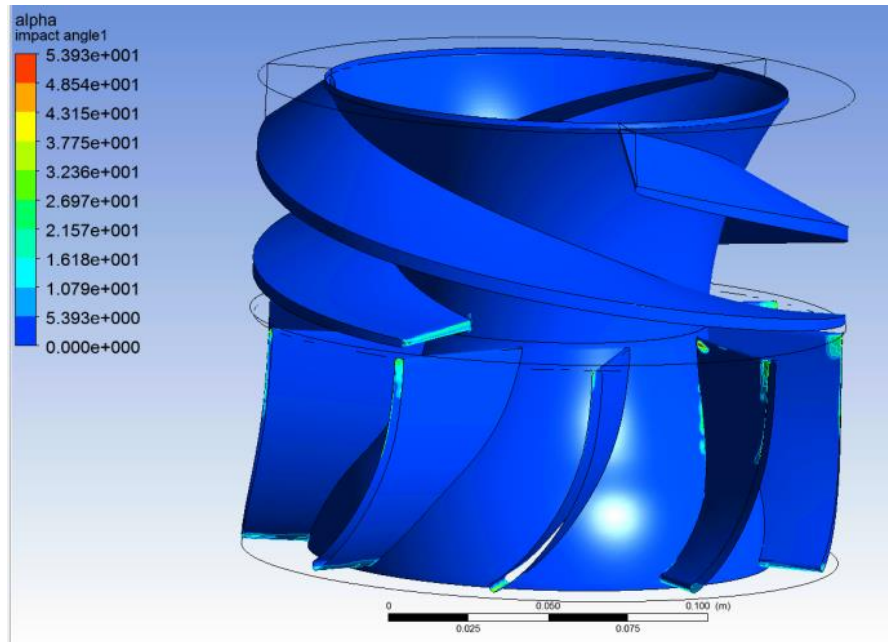


Figure 102: Contours of the Impact Angle (unit: degree), 120-Degree Averaged

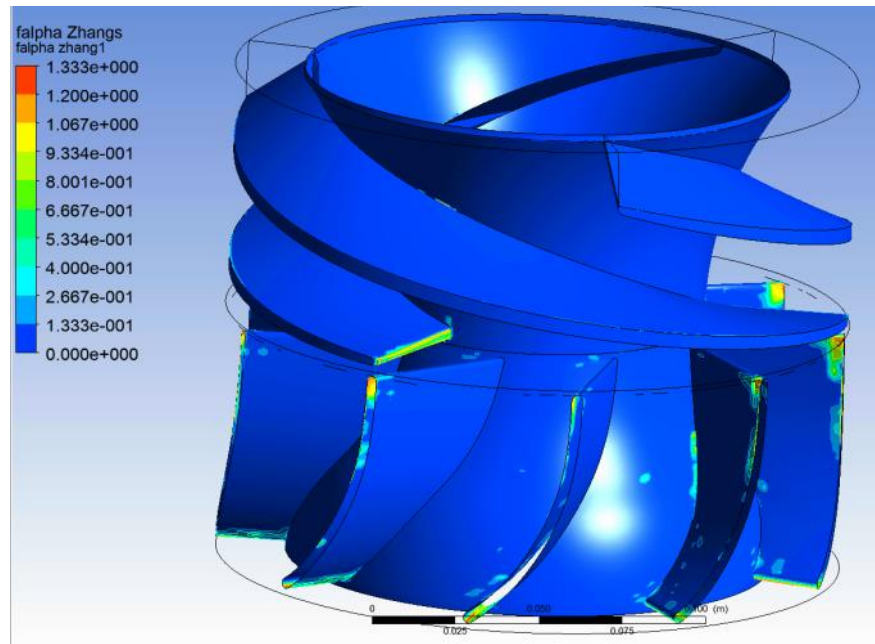


Figure 103: Contours of the Impact Angle Function, 120-Degree Averaged

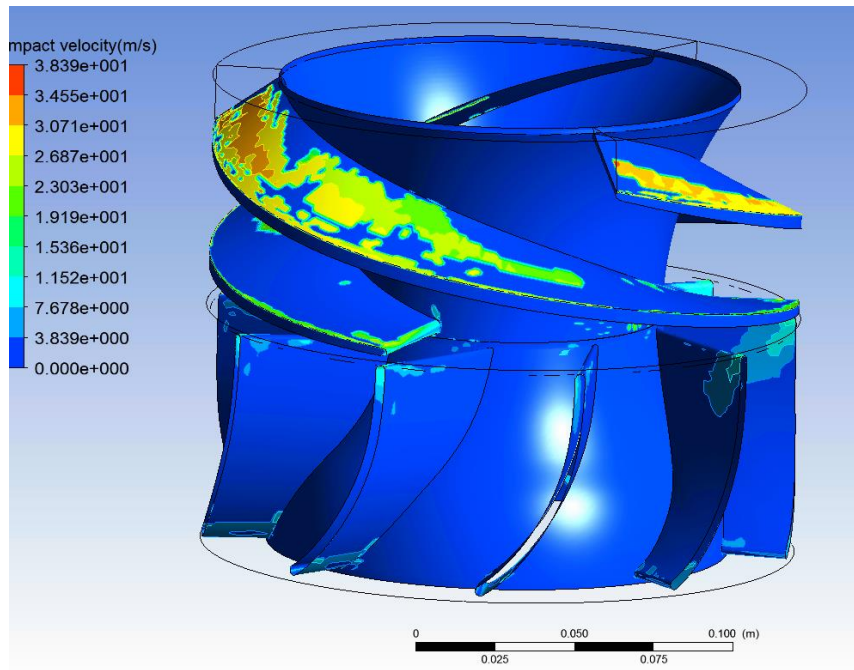


Figure 104: Contours of the Impact Velocity, 120-Degree Averaged

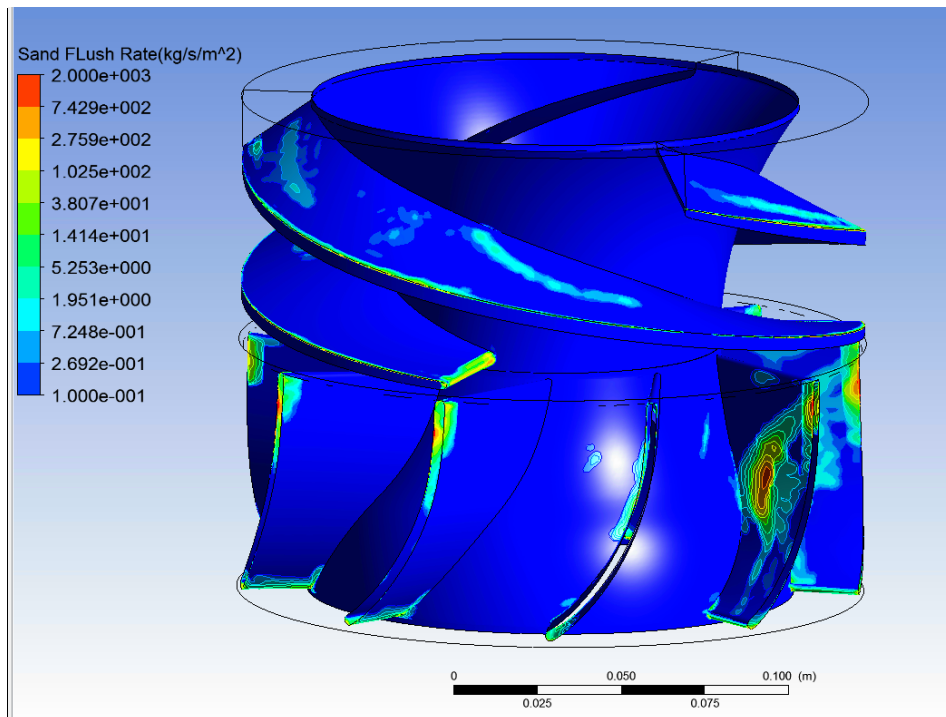


Figure 105: Contours of the Sand Flush Rate, 120-Degree Averaged

(Logarithmic Scale)

Assuming the wear has a linear relationship with time and erosion rate, equation (26) is prepared for least square regression. **Table 10** presents the calibration details. From 40-degree average to 120-degree average, the correlation coefficient stabilizes over 0.7.

(**Figure 106**, **Figure 107** and **Figure 108**). The coefficients, a, b, c, n, are stable as well.

$$\begin{aligned} \text{Log}(\overline{E}_R * T) - \text{Log}(f(\overline{\alpha})) - \text{Log}\left(\overline{m} * \Delta t * \frac{T}{\Delta t}\right) & \quad (26) \\ = \text{Log}(c) + n\text{Log}(V) & \\ \text{Log}(c) = b, n = a & \end{aligned}$$

T: erosion time, 7.2E+05 seconds

Δt: Time spent in rotating by certain degrees

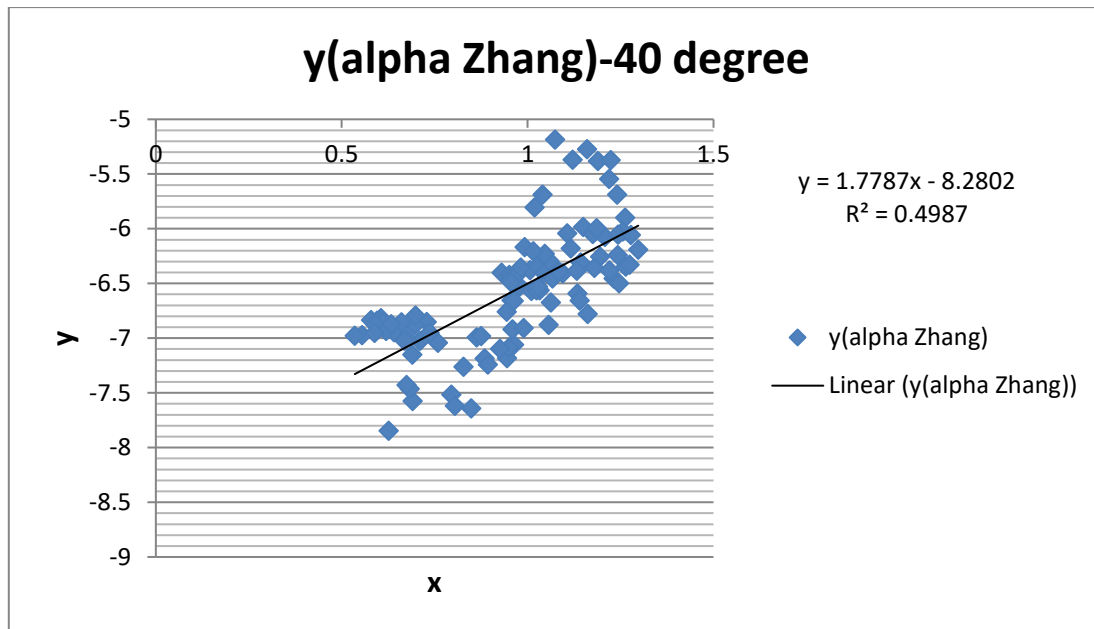


Figure 106: Calibration for the Erosion Model from 40-Degree Averaged Simulation

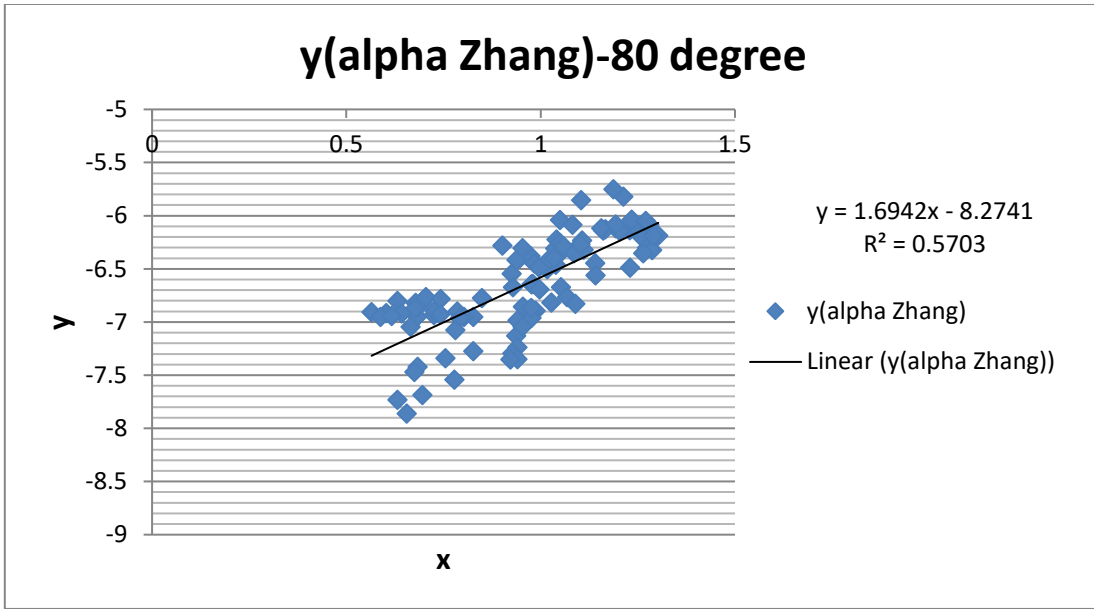


Figure 107: Calibration for the Erosion Model from 80-Degree Averaged Simulation

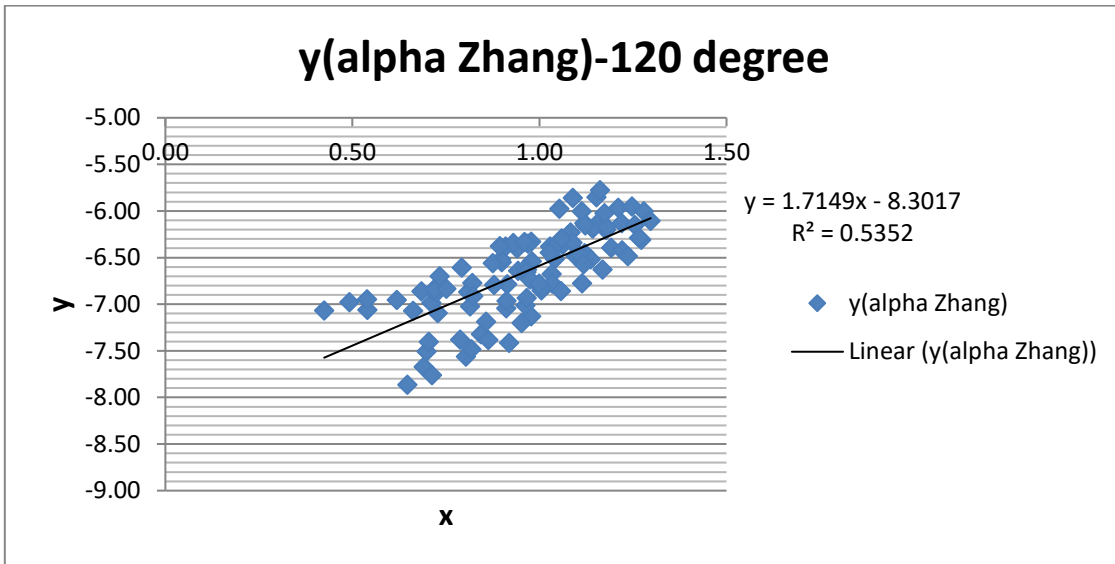


Figure 108: Calibration for the Erosion Model from 120-Degree Averaged Simulation

Table 10: Coefficients from Least Square Regression Analysis

	40degree	80 degree	120 degree
R ²	0.4987	0.5703	0.5352
R	0.7061	0.7551	0.7315
a	1.778	1.694	1.714
b	-8.280	-8.274	-8.301
c	5.245E-09	5.319E-09	4.992E-09
n	1.778	1.694	1.714

Choosing the c and n calibrated from the 120-degree-averaged simulation, the final erosion empirical equation reduces to equation (27). After applying this model to the 120-degree-averaged simulation, the erosion rate is shown in **Figure 109** and **Figure 110**. Assuming the linear relationship between loss of thickness and time, equation (28) can be used to predict the wear of the pump.

$$\overline{E}_R = 4.992\overline{m}V_{sand}^{1.714}f(\overline{\alpha}) \times 10^{-9}(mm/s) \quad (27)$$

$$\begin{aligned} Wear &= \int_0^T (E_R t) dt \approx \overline{E}_R T \\ &= 4.992\overline{m}V_{sand}^{1.714}f(\overline{\alpha})T \times 10^{-9}(mm) \end{aligned} \quad (28)$$

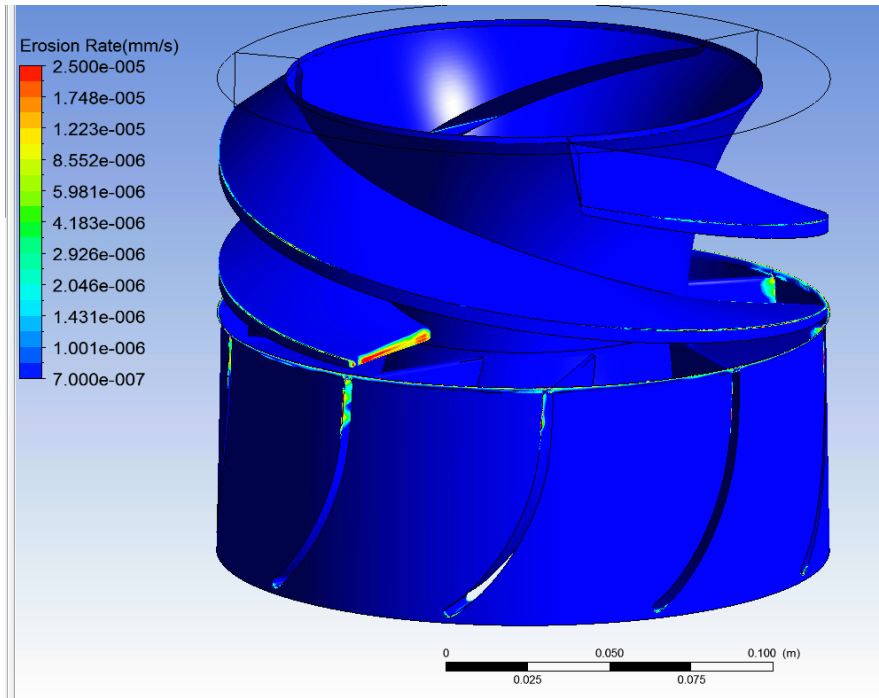


Figure 109: Erosion Rate near 2nd Impeller Inlet, Logarithmic Scale (unit, mm/s)

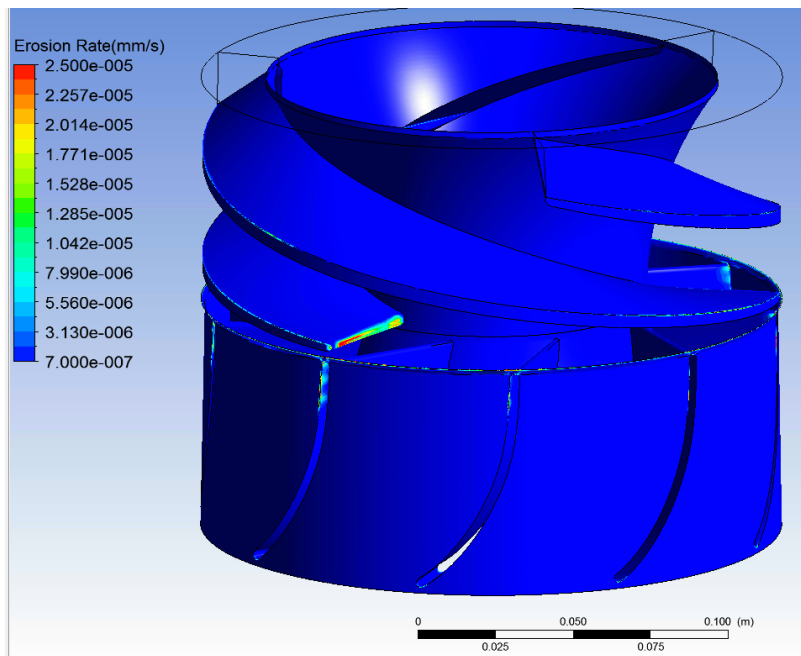


Figure 110: Erosion Rate near 2nd Impeller Inlet, Linear Scale (Unit, mm/s)

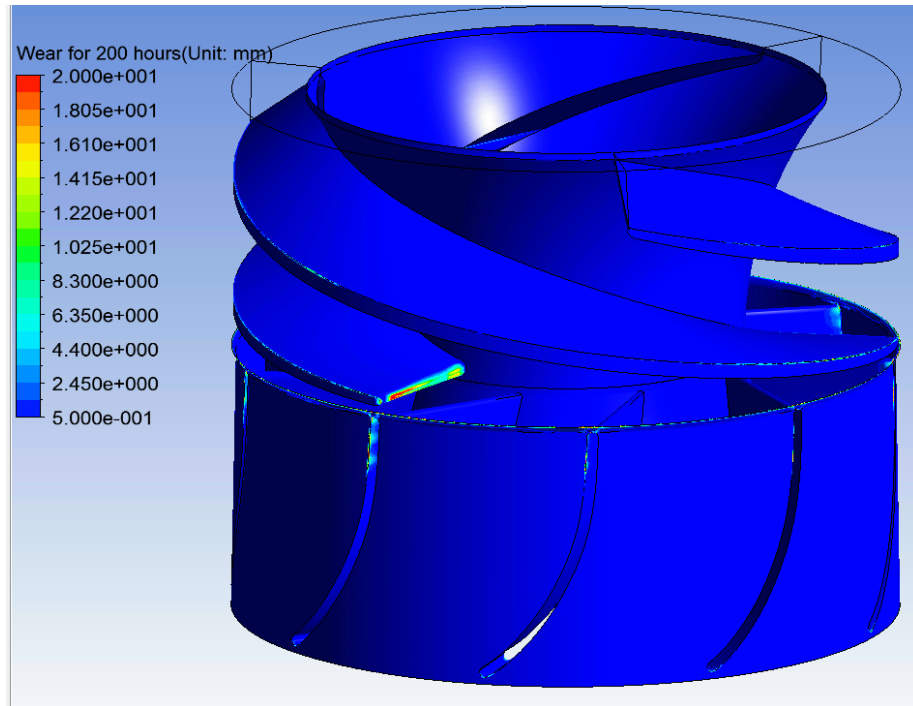


Figure 111: Wear on near the 2nd Impeller for 200 Hours, Linear Scale (Unit, mm)



Figure 112: Eroded 1st Diffuser and Eroded 2nd Impeller

Comparing the wear prediction in **Figure 111** with the actual wear on the pump in **Figure 112**, the wear predicted has a nice match with the actual wear. The predicted values at the leading edge in **Figure 111** are close to the values plotted in **Figure 71**. Even the wear at the diffuser trailing edge which is not considered in calibration, is captured by the prediction.

However, the quantitative difference is still observable. There are three main factors that lead to this difference:

First, the wear actually does not have a linear relationship with time and erosion rate. The material loss on the impeller happens gradually during the erosion test. Comparing with the pipe or elbow, the leading edge of an impeller has a smaller effective erosion area but a greater effect on the flow. Any slight volume loss of the leading edge will lead to a big change of local flow and affect the impact angle, impact velocity, and sand flush rate, all of which directly affect the erosion rate. This makes the prediction even harder.

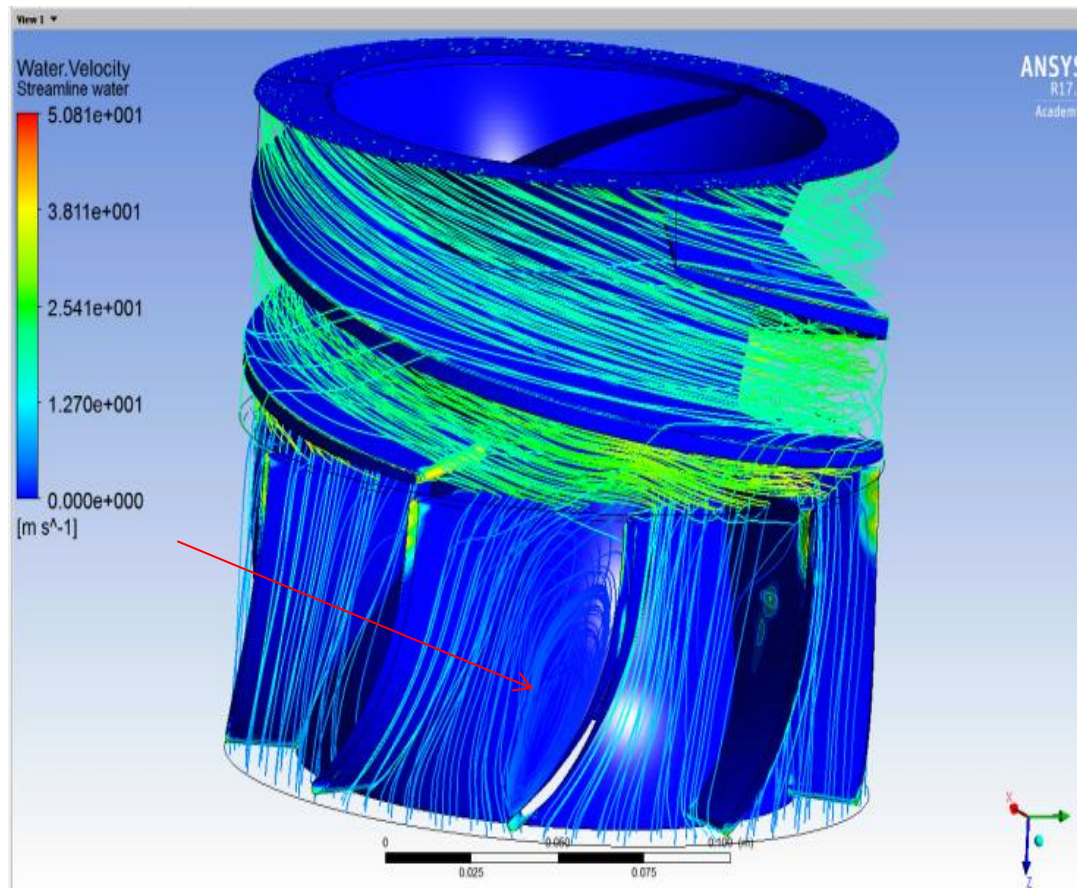


Figure 113: Water Streamline in 3-Phase Simulation without 1st Imp

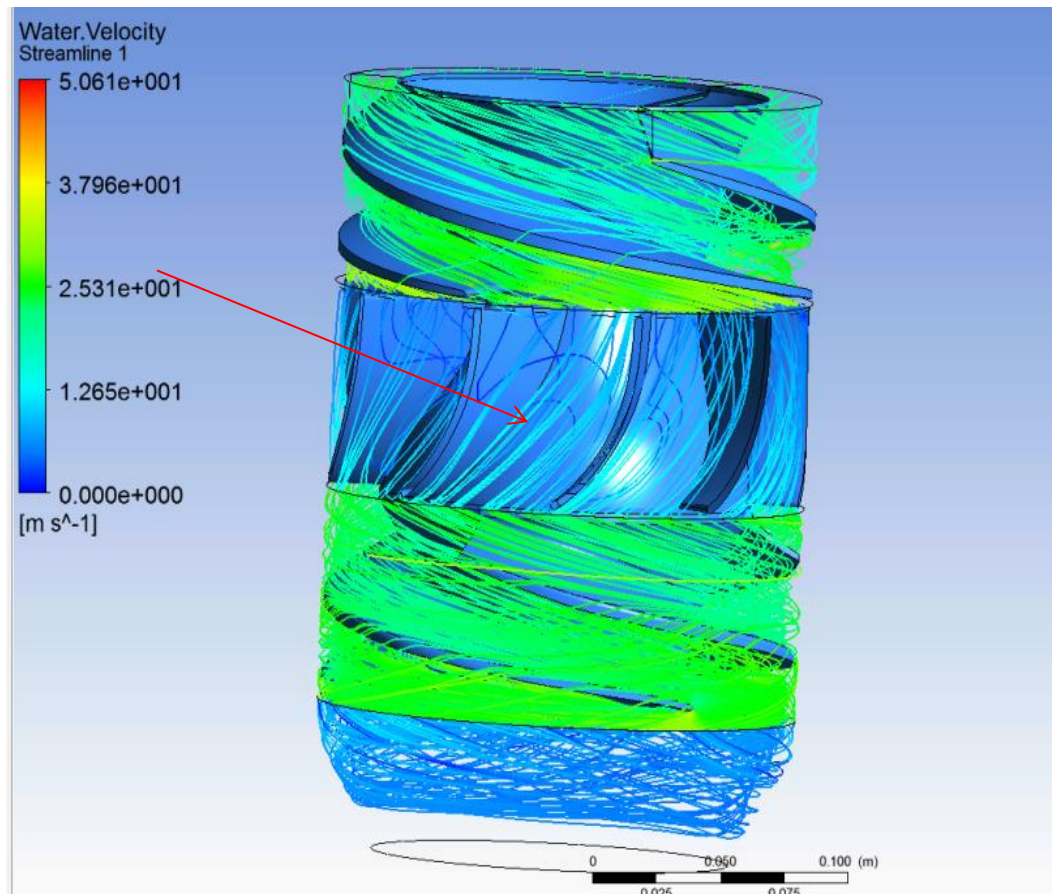


Figure 114: Water Streamline in 2-Phase Simulation with 1st Imp

Second, the velocity angles for all the three phases at the diffuser inlet are defined as 90 degree, which is not true. Moreover, the volume fraction of each phase at the diffuser inlet is actually not uniform. These two differences between the reality and simulation will affect the sand flush rate and impact angle at the leading edge of the impeller.

Figure 113 and **Figure 114** presents that the different inlet velocity angles cause different flow separation condition at the diffuser channel.

Third, the impact angle function used in this study is developed by Y. Zhang[23] based on a series of direct impact tests of Inconel 718 conducted by researchers at the E/CRC and Baker Oil Tools [47]. Therefore, it is not necessarily applicable to the pump material which is ASTM A436 Type I Ni-resist cast iron in the test.

Other assumptions might also affect the result. For example, it is assumed that all the particles have the same size and sharpness. But these are the secondary factors compared with three main factors mentioned above.

The first problem can be solved by using the erosion-MDM coupling method, which is the add-on erosion module provided by ANSYS. This method changes the shape of the mesh after each step according to the erosion function. However, this module is still under development and not feasible to use. One of its shortcomings is its ability to deal with the transient flow. Even if it works well, significant computer hours is still an issue. In this three-phase simulation, after the flow is stabilized, it takes 25 days for the impeller to rotate 40 degrees. (Simulation is run on the computer with Intel® Xeon® Processor, 256 GB RAM, 20 Cores, 40 Threads) If coupling the MDM, it will undoubtedly take even longer.

For the second problem, it is not possible to determine the exact velocity angle or sand distribution at the 1st diffuser inlet unless adding the 1st impeller to the simulation. However, it will take even longer for such a three-phase simulation.

For the third problem, designing a test, like R.D. Russell et al[47], to acquire the impact function for Ni-Resist material and frac sand might be a solution. But it costs a huge amount of time and money as well. Therefore, it is more economical to find an impact function for the material that has similar properties to the material of pump in the study.

Erosion is affected by a lot of parameters. Therefore, to quantitatively analyze all the effects of these parameters costs a lot of time and money. It also requires the development of the computer capacity. In industry, to accurately predict the wear in quantity might be not so important. Sometimes, the designers just need to know the weakest area so that they can strengthen it. Or, a quantitative estimation of the thickness loss with even 100% error will be regarded as a good prediction[23]. Weighing the balance between costs and the accuracy of the prediction, this output is acceptable. It has already improved the accuracy a lot for erosion prediction of the pump.

Table 11 compares the erosion CFD model with other studies which has already been mentioned in the literature review.

In this study, the simulation is not necessarily three-phase if the test required by the sponsor is given by two-phase. This increases the difficulties in the simulation. The axial pump will limit the radial movement of each phase. Particle model is using Lagrangian method (DPM) in a transient condition. This improves the accuracy but it also increases the computer hours. The erosion model is given with the parameters which are more

directly affecting erosion. For example, the sand concentration at the wall cannot describe how much effective particle impacts on the wall without showing impact angle. And the mixture velocity cannot directly represent the impact velocity if the drag force is much smaller than inertial force. The model is calibrated by the erosion test, which provides the verification and improves the accuracy of the prediction.

Table 11: Details of the Models for Pump Erosion in Different Studies.

	Stavros et al(2009)	Krüger et al (2010)	Pirouzpanah et al (2014)	This study(2017)
Phase	2	2	2	3
Pump type	Mixed	Centrifugal	Mixed	Axial
Particle	20-70um (CFD)	32um, quartz sand	140um, frac sand	140um, frac sand
Pump speed (rpm)	2650	NA	3600	3600
CFD-particle model	Lagrangian, steady	Eulerian	Eulerian, transient	Lagrangian, transient
Erosion test on pump	NA	150g/liter water,	117 hour, 2g/liter, 1457gpm water, 0% gvf	200hour, 2.4g/liter, 880gpm water, 20% gvf
Erosion model, and calibration	$EF = kV_p^n f(\alpha)$ K is measured, no calibration	$F_{KG} \left(\frac{c_{s,eq}}{c_{s,Ref}} \right) \left(\frac{W_{mix}}{W_{Ref}} \right)^3$ No calibration	$(c_s)^{0.08} \left(\frac{V_s}{V_{s0}} \right)^{0.07} \left(\frac{k_w}{k_{w0}} \right)^{1.25}$ $ER = A \cdot EF^2 + B \cdot EF$ A, B are calibrated	$\bar{E}_R = C \bar{m} \bar{V}_{sand}^n f(\bar{\alpha})$ C, m are calibrated
Impact angle function	Finnie	NA	NA	Zhang
Parameters considered	impact velocity, impact angle	sand concentration, mixture velocity	Sand concentration, TKE-water, sand velocity	impact velocity, impact angle, sand flush rate

4.4 Bearings and Vibration

Although the performance degradation caused by the wear of the impeller directly affects the productivity, the reliability issue of the bearings is more important to the run life of an ESP. In this section, the wear of bearings and the vibration affected by erosion will be analyzed.

4.4.1 Orbits and FFT at Operation Condition

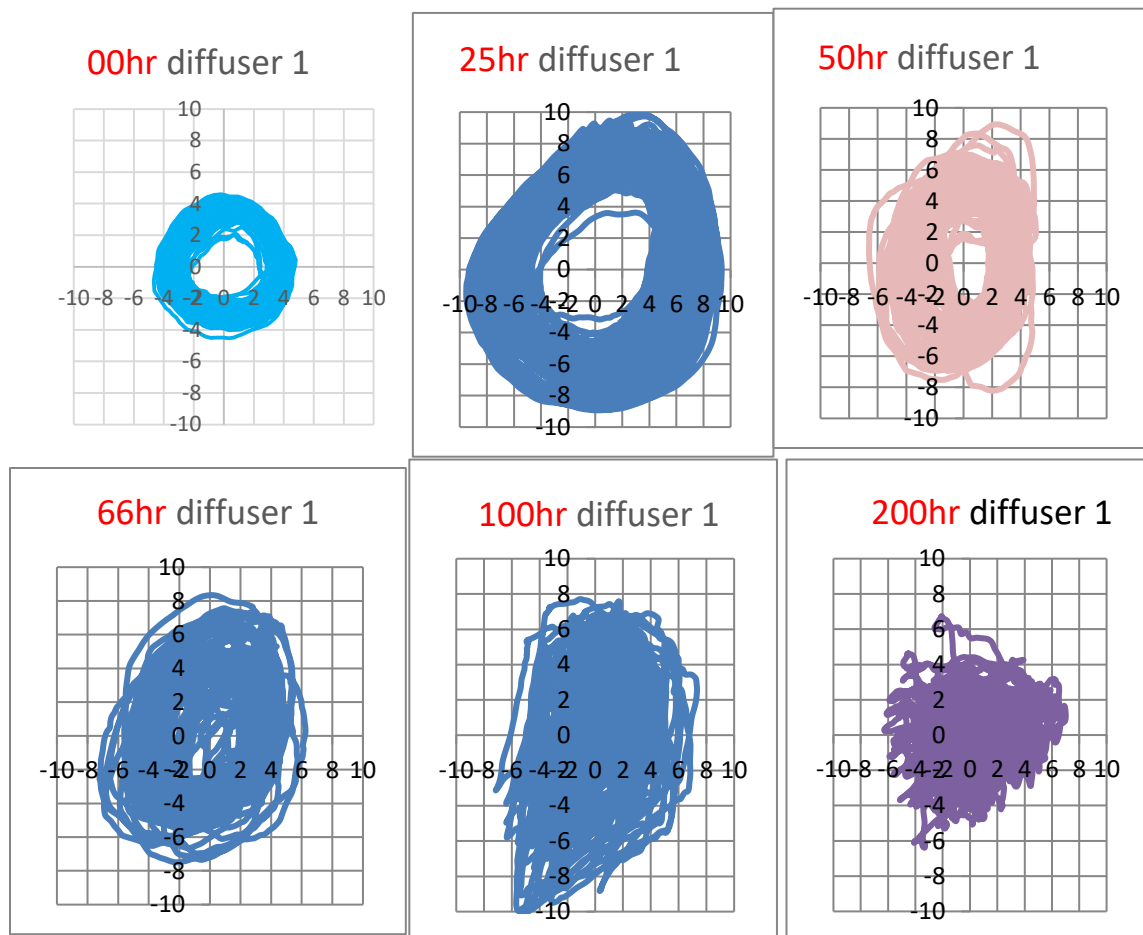


Figure 115: Orbit at the 1st Diffuser

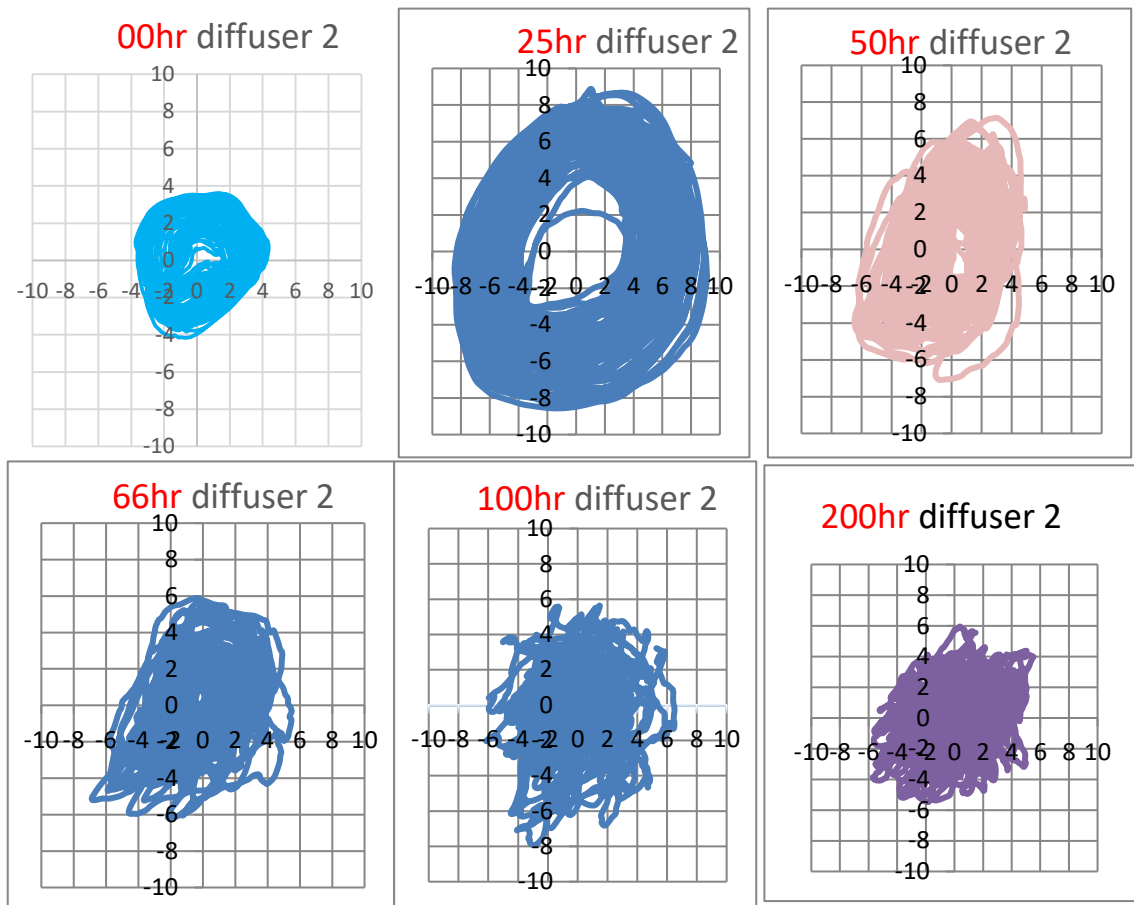


Figure 116: Orbit at the 2nd Diffuser

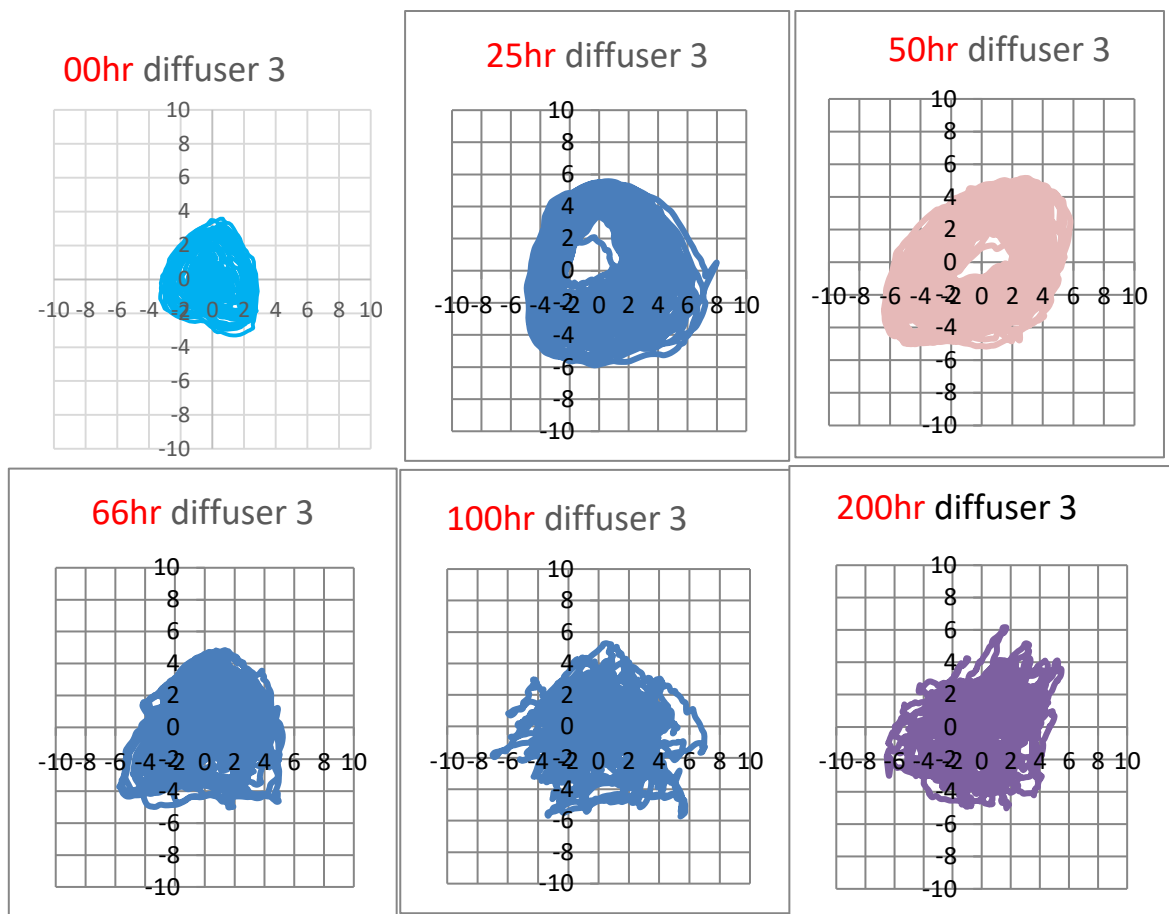


Figure 117: Orbit at the 3rd Diffuser

As is mentioned in 3.1.6, proximity probes were installed during the performance test to record the orbit. **Figure 115**, **Figure 116** and **Figure 117** present plots of the orbits at the 0th, 25th, 50th, 66th, 100th, 200th hour at certain locations when the ESP is running at operating condition (3600rpm, 20%GVF, 880GPM). Each orbit contains 5000 sample points corrected in 1 second. Coordinate transformation has been performed to acquire the orbits at an orthogonal coordinate. The magnitude of the orbit at each location increases in the 1st 25 hours due to erosion and the orbit at the 1st diffuser has the biggest

size while the 3rd one, the smallest. Because of the thrust bearing/seal located on the shaft above the pump's end stage, it eliminates shaft oscillations at its location due to the radial roller bearings inside it. Moreover, the most uneven gas void fraction at the 1st impeller has caused the biggest imbalance at the 1st stage than other stages. At 50th hour, the size does not increase but decreases, instead. The profile of the orbit at each location becomes more and more irregular in the last 150 hours. Rubbing of the journal and bushing during the first 50 hours causes the circular orbits. Once the bearings have worn, the bearings no longer help reducing orbit amplitude and the dominant circular motion. In order to analyze the frequency, the Fast Fourier Transformation(FFT) is performed on this orbit signal. The signal collected by two proximity probes are similar, so only one direction of the signal is selected at one location. **Figure 118**, **Figure 119**, and **Figure 120** present the FFT plots of three orbits in the Y direction at the 0th, 25th, 50th, 66th, 100th, 150th, 200th hour. Here, one unit(1X) of frequency ratio stands for 1X rotating frequency(at 3600 rpm, 1X stands for 60Hz; at 1800 rpm, 1X stands for 30Hz). At the beginning, at each location, the biggest peak of the signal magnitude appears at 1X and the second biggest appears at 2X. These 2 peaks are the only ones that are observed. The 1X peak achieves maximum amplitude at the 25th hour and then starts to decrease, while the 2X peak keeps increasing of all the 200 hours. Meanwhile, a peak near 0X keeps growing during the 200 hours and becomes no smaller than the 1X peak in the end. From 0X to 1X, more and more random fluctuations appear during the erosion test. In addition, the 3X and 4X peaks start to appear at a small but observable size. Generally,

the orbit at the 1st diffuser has the largest amplitude at 1X and the 3rd diffuser, the smallest. The reason has been explained when discussing the orbits.

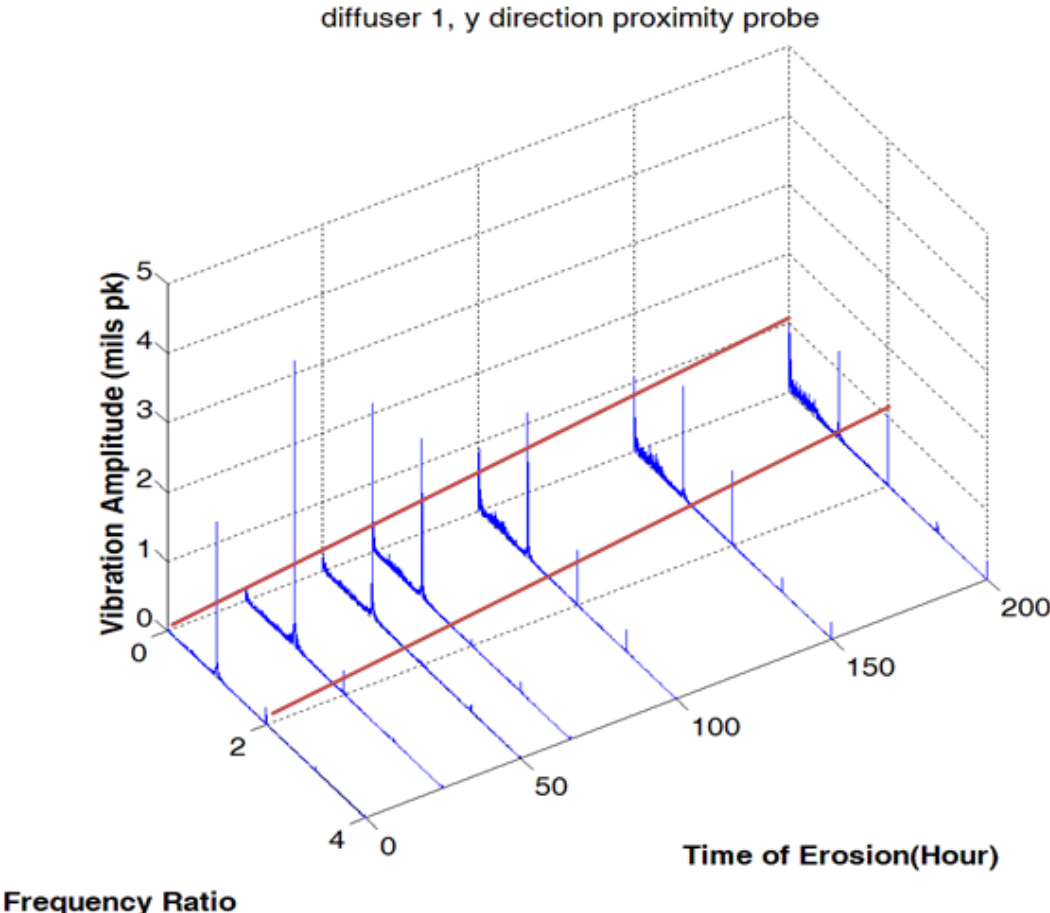


Figure 118: Orbits after FFT for the 1st Diffuser

diffuser 2, y direction proximity probe

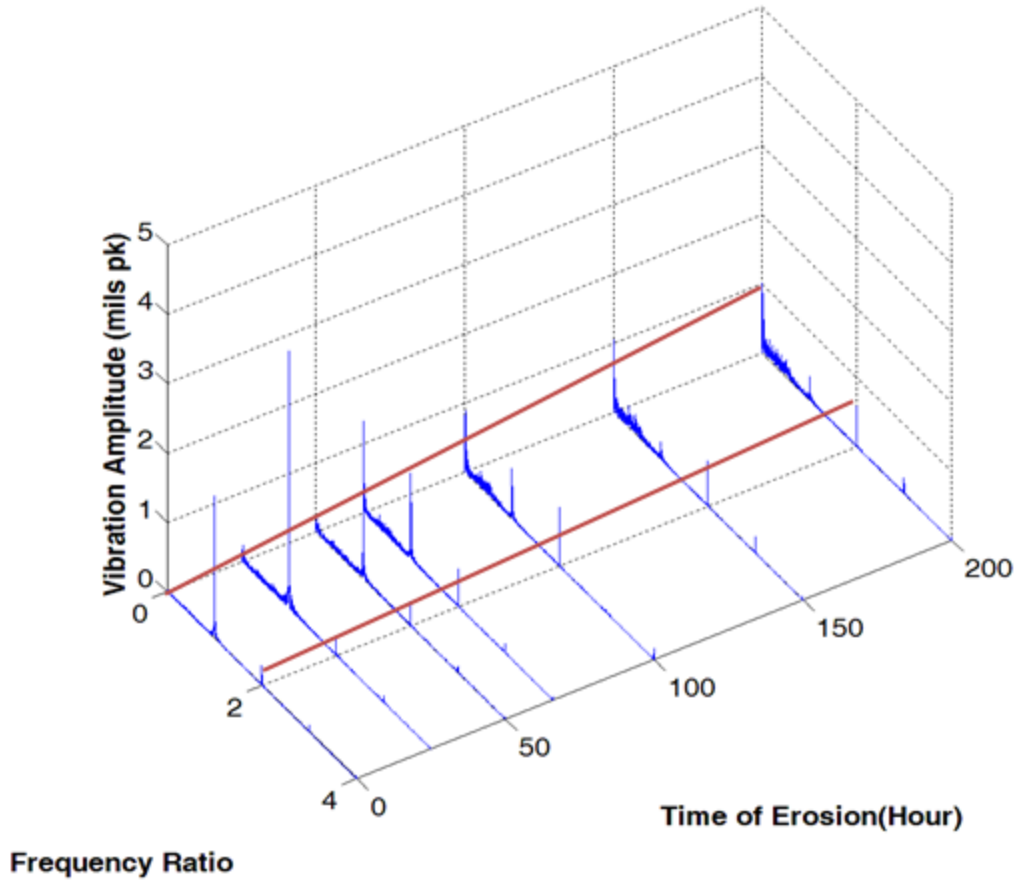


Figure 119: Orbits after FFT for the 2nd Diffuser

diffuser 3, y direction proximity probe

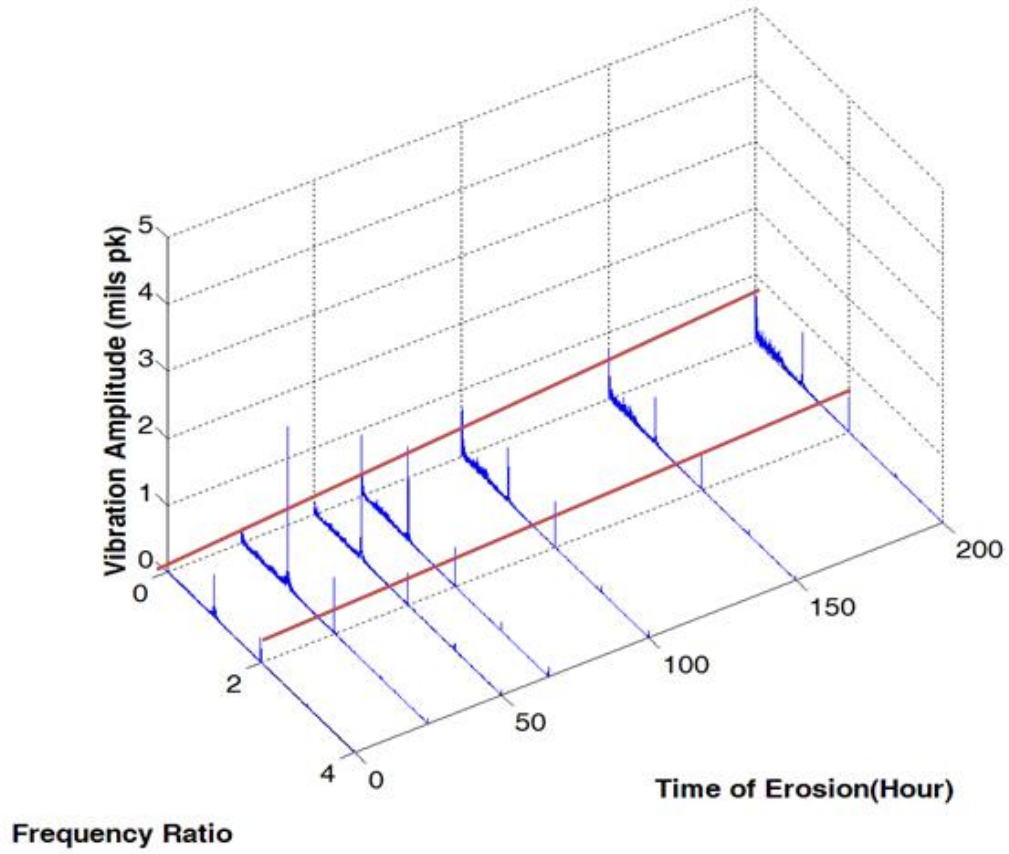


Figure 120: Orbits after FFT for the 3rd Diffuser

4.4.2 Waterfall Plots in RPM Test

The FFT plots above provide a perspective of the frequency of the shaft vibration and help to explain the irregular plots of orbits. In the RPM test (with water only, at 800, 1200, 1600, 2000, 2400, 2800, 3200, 3580 RPM), the FFT of the orbits at the different RPMs are used to assemble the waterfall plots of the shaft vibration. Considering the similar trends of the waterfall plots at 2 directions and 3 locations, only the waterfall for the 1st diffuser and y-direction are chosen (Figure 121, Figure 122, and

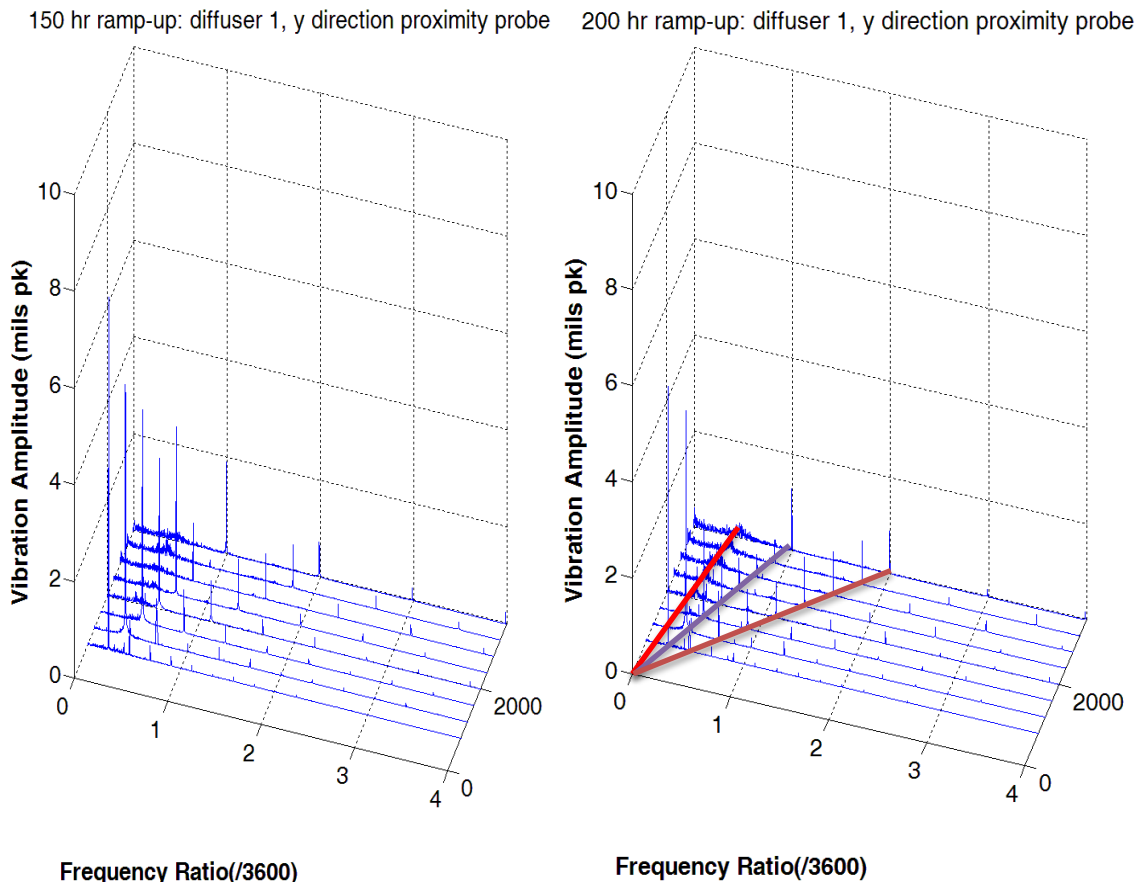


Figure 123). For the 1st 25 hours, the 1X peak increases with the erosion time and the rotating speed. This means the clearances of the bearings increase due to the wear, and the bearings are still working properly to load the centrifugal force. However, after 25

hours, as was discussed in 4.4.1, the peak at 1X starts to decrease when the rotating speed increases in the RPM test. Although at low speed, this peak increases with erosion test hours. This means the bearing clearance is getting bigger in the erosion test, and it gradually loses the normal working condition to load greater radial force on the shaft when the rotating speed increase. The abnormal working condition, rubbing, is becoming easier and easier to happen. Compared with the peaks in **Figure 118**, the peaks at 0X are not that large. Instead, there is a small blunt peak appears at 0.5X in each of the waterfalls after the 50th hour, getting larger and larger. It might be the same to the subsynchronous peak at 2/3X observed in Zheng's study[36](**Figure 19**).

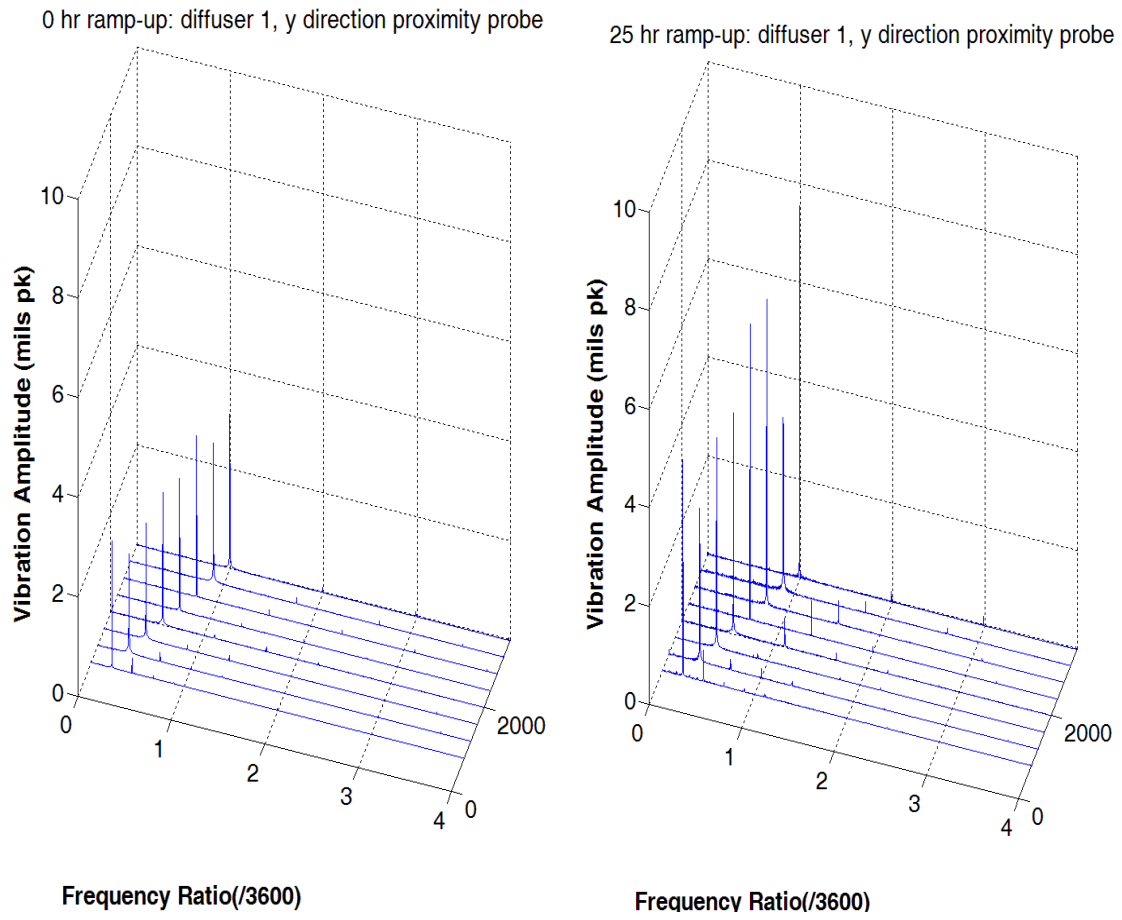
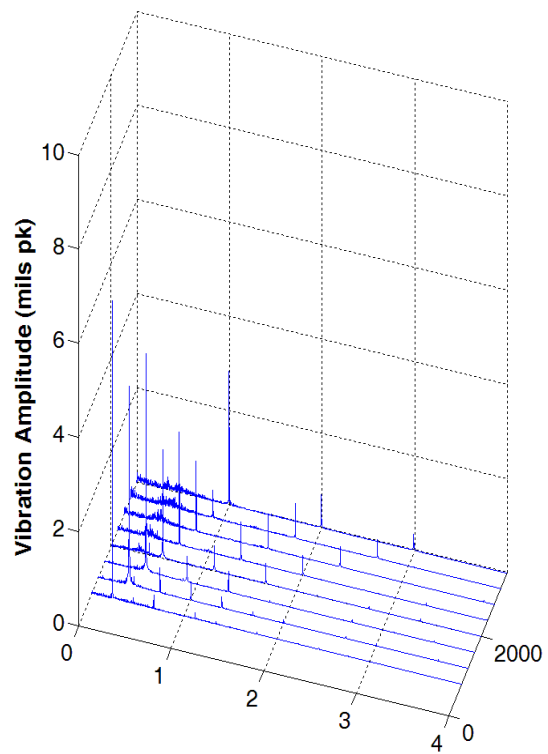
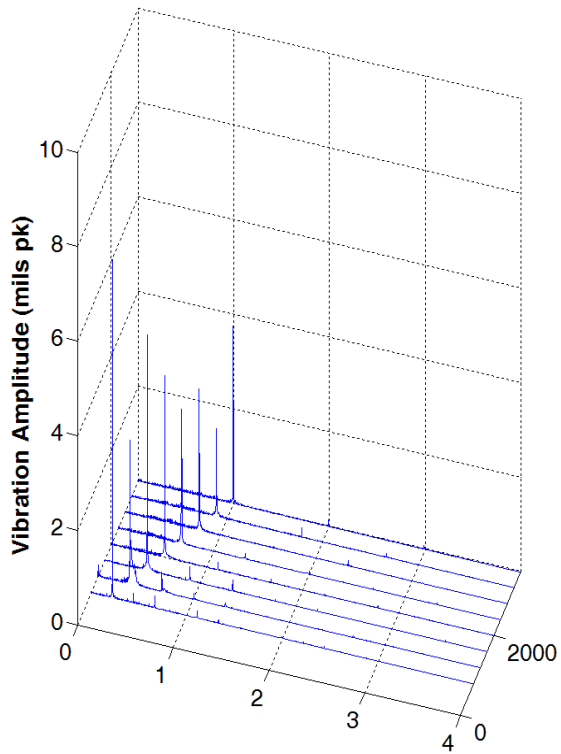


Figure 121: Waterfall of the Orbits at 1st Diffuser (0th, 25th hour)

50 hr ramp-up: diffuser 1, y direction proximity probe

100 hr ramp-up: diffuser 1, y direction proximity probe



Frequency Ratio/(3600)

Frequency Ratio/(3600)

Figure 122: Waterfall of the Orbits at 1st Diffuser (50th, 100th hour)

150 hr ramp-up: diffuser 1, y direction proximity probe

200 hr ramp-up: diffuser 1, y direction proximity probe

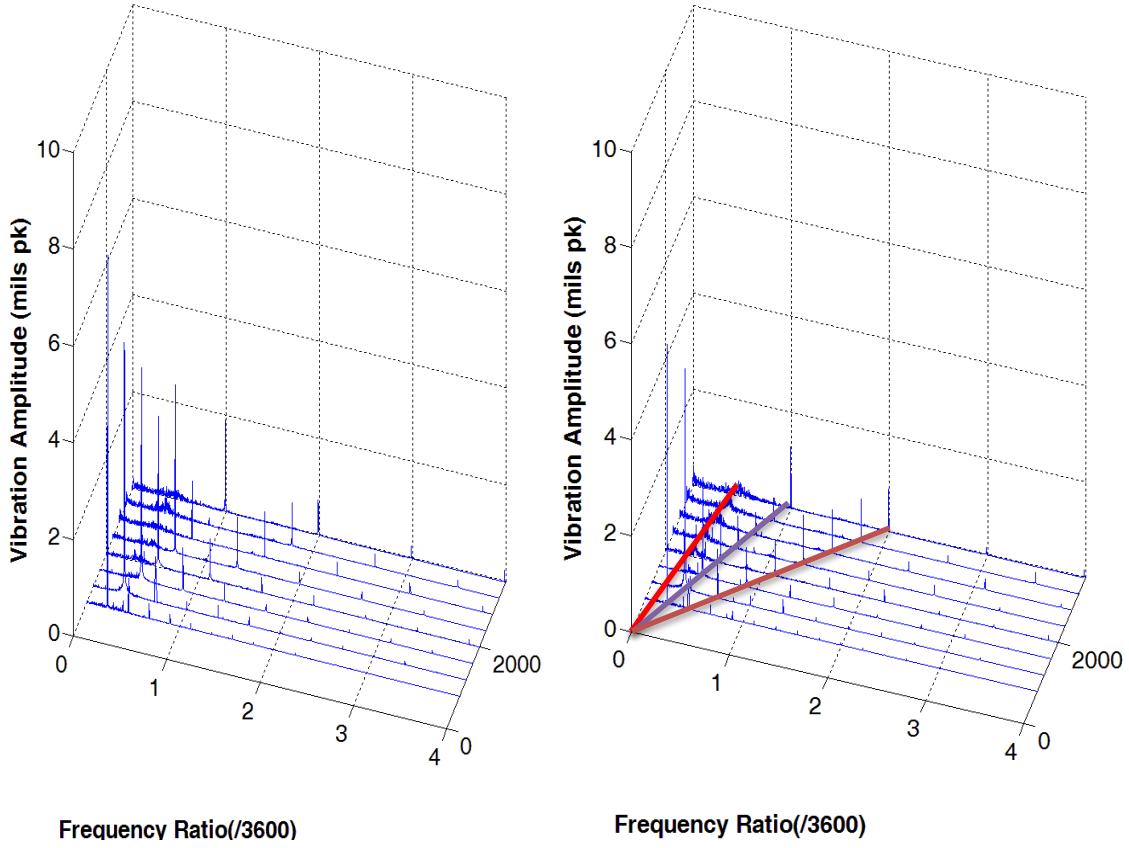


Figure 123: Waterfall of the Orbits at 1st Diffuser (150th, 200th hour)

4.4.3 Bearing Wear

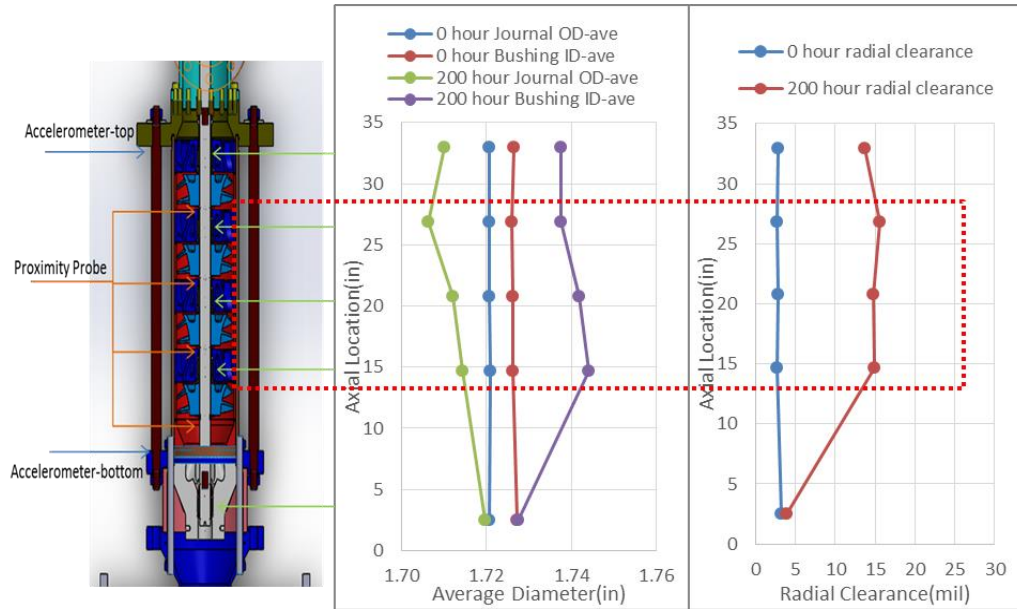


Figure 124: Measurement of the Bushing and Journal Bearing

The pressure difference between two sides of a stage pushes the water back through bearing. When the sand enters the clearance of the bearings, the journal and bushing grind the particles in the clearance, making the clearance larger. Figure 124 reveals the bearing clearances before and after erosion, which are calculated via inner diameters of the bushing and outer diameters of the journal. Due to the rotating of the 4th diffuser, some uncertainties might have affected the wear. So it is listed but not discussed in the analysis. Considering the first 3 stages, the clearance increases are close but the loss of thickness on journal and bushing are different. The average radial clearance increase of the bearing on the stages is over 10mils, which will be an issue for ESP reliability. The

orbits and FFT peaks that obtained from proximity probes cannot capture this increase at the 200th hour due to the rubbing of the shaft, although rubbing is most probably caused by the increase of bearing clearance.



Figure 125: New and Eroded Journal Bearings

Table 12: Microscopic View of the Journal Bearing at the 1st Diffuser

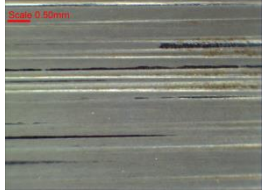
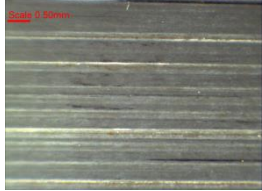
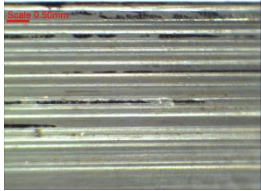
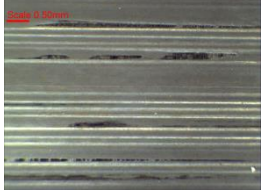
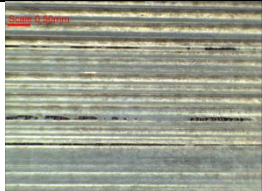
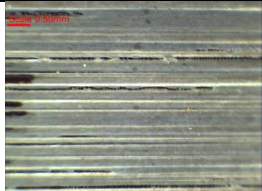
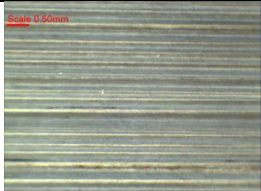
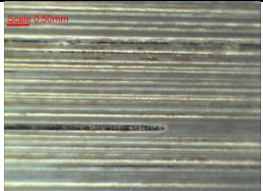
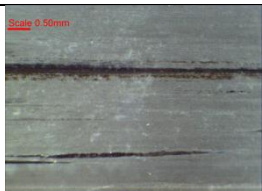
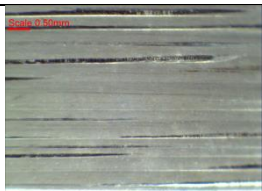
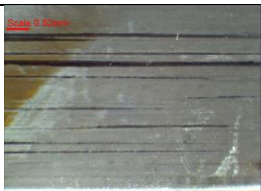
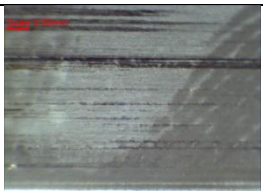
Journal 1, top, mid, bot,0 degree	Journal 1, top, mid, bot,90 degree	Journal 1, top, mid, bot,180 degree	Journal 1, top, mid, bot,270 degree
			
			
			

Figure 125 shows the five eroded journals on the shaft and a brand new journal. The grooves made by sand are observable but not clear on this picture. Pictures in **Table 12** are the microscopic views of the eroded bearing at the 1st diffuser, for 3 axial locations by 4 circumferential directions. Near the top, the big groove width (0.13-0.15mm) is close to the size of 100-mesh sand (0.15mm). In the middle, the number of grooves becomes denser, and most grooves have smaller width (<0.1mm). Near the bottom, groove number reduces. This can be explained by the crushing process of the particles

carried by the leakage flow, from top to the bottom. Similar phenomena are observed from the journal bearings at diffusers of other stage.

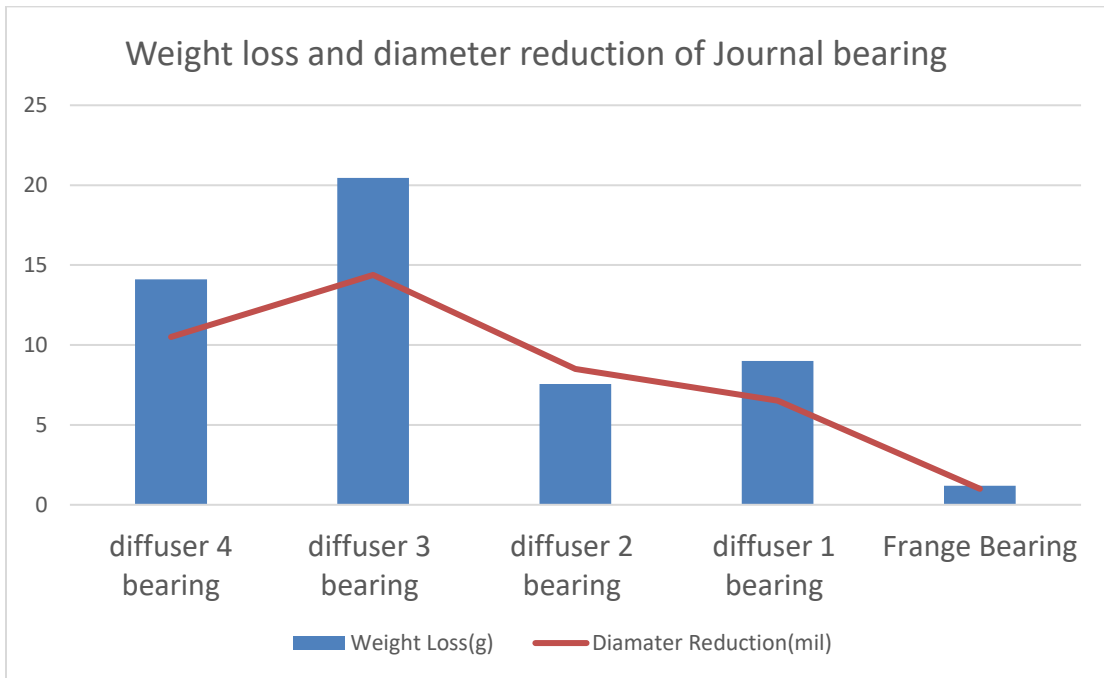


Figure 126: Weight Loss and Diameter Reduction of Journal Bearings

Since the bushing is not easy to disassemble from the diffuser, only the weight loss of the journal is measured. **Figure 126** presents the comparison of the diameter reduction and the weight loss. Generally, the weight loss shows a linear relationship with the diameter reduction.

5. CONCLUSIONS AND SUGGESTIONS

In this study, not only the traditional methods (experiment and simulation) are used, but also the novel scanning method is utilized. Although operation error and image process error are unavoidable, 3D scan technology can still provide a more accurate measurement for the material loss of the pump. In addition, by inputting the eroded geometry that scanned, the simulation can be more accurate and explain the head loss of the pump. The results from these three methods are nicely combined in the erosion analysis.

Some conclusions about the erosion study and suggestions to improve the ESP are listed below:

1. Erosion mostly appears at the impeller leading edge, tip near the leading edge, diffuser trailing edge and bearing.
2. Loss of thickness at the leading edge of the impeller, or the increase of the tip clearance, or both of them cause the performance loss of the ESP.
3. Erosion has a greater effect on the performance loss at small flow rates or low GVF.
4. GVF does not have an obvious effect on the volume of metal loss. If there is any, it should be a minor negative effect.
5. The single-phase simulation on the eroded impeller can capture the head loss of the impeller, which mainly happens in the area with the most severe material loss.

6. Considering the pressure difference between the pressure side and suction side of an impeller, the larger pressure difference near the leading edge might be the reason for the larger tip clearance caused by the leakage flow erosion.
7. By the erosion model calibrated, this pump could be improved by coating the weak points at the impeller leading edge and diffuser trailing edge.
8. Bearing wear caused the bearings to lose the ability to hold the shaft without rubbing in the first 50 hours. This might be the most important issue to the reliability of this pump. Some design to protect the bearing can prolong the run life of the pump.

Some proposals for the further study on erosion are shown below:

1. When testing the multi-stage pump, the 1st stage and last stage will not have the similar inlet or outlet flow regimes, which makes the analysis on them differ from the analysis on the stages between them. To go further in this study, a pump with more than five stages is required.
2. Only one type of erosion model is generated in this study. To have other models to compare, it is necessary to calibrate some other types of erosion models.
3. When the calculation ability of the computer is improved, it is possible to perform Erosion-MDM coupling simulation. If doing this, a great erosion model that calibrated is a “must”.

REFERENCES

- [1] Gabor Takacs, 2009, "Electrical Submersible Pumps Manual," Gulf Professional Publishing.
- [2] Schlumberger, 1999, "Gas Lift Design and Technology", [Online]. Available: <http://igs.nigc.ir/STANDS/BOOK/Gas-Lift-Technology.pdf>, [accessed 12 July 2017].
- [3] Clegg, J. D., Bucaram, S. M., & Hein, N. W. (1993, December 1). Recommendations and Comparisons for Selecting Artificial-Lift Methods(includes associated papers 28645 and 29092). Society of Petroleum Engineers.
- [4] Neely, B., Gipson, F., Clegg, J., Capps, B., & Wilson, P. (1981, January 1). Selection of Artificial Lift Method. Society of Petroleum Engineers.
- [5] K. Brown, 1977, "The Technology of Artificial Lift Methods", PennWell Publishing Company, Tulsa, OK.
- [6] Dover, 2011, "Technology Tour", [Online]. Available: <http://www.sec.gov/Archives/edgar/data/29905/000095012311055709/y91520exv99w1.htm>, [accessed 12 July 2017].
- [7] Dover, 2012, "Technology Tour", [Online]. Available: <http://www.sec.gov/Archives/edgar/data/29905/000002990512000024/form8k060412ex991.htm>, [accessed 12 July 2017].

- [8] Dover, 2013, “Technology Tour”, [Online]. Available:
<https://www.sec.gov/Archives/edgar/data/29905/000002990513000033/a201306038kexhibit991.htm>, [accessed 12 July 2017].
- [9] W.P. O'Toole, J.B. O'Brien, 1989, “Testing New Submersible Pumps for Proper Sizing and Reduced Costs” Society of Petroleum Engineers.
- [10] Divine, D.L. Lannom, R.W. and Johnson, 1992, ” Determining Pump Wear and Remaining Life from Electric Submersible Pump Test Curves”, Society of Petroleum Engineers.
- [11] E.R. Upchurch, 1990,“ Analyzing Electric Submersible Pump Failures in the East Wilmington Field of California”, Society of Petroleum Engineers.
- [12] I. FINNIE, 1958, “The mechanism of erosion of ductile metals”, Proc. 3rd U.S. Natl. Congr. Appl. Mech.
- [13] I. Finnie, 1972, “Some observations on the erosion of ductile metals” I. Finnie, Some observations on the erosion of ductile metals, *Wear*, Vol. 19, Iss. 1, pp 81-90.
- [14] I. Finnie, 1960, “Erosion of surfaces by solid particles” Iain Finnie, Erosion of surfaces by solid particles, *Wear*, Vol 3, Iss 2, pp 87-103.
- [15] J. G. A. Bitter, 1963, “A STUDY OF EROSION PHENOMENA 1”, *Wear*, Vol. 6, Iss. 1, 1963, pp 5-21.

- [16] J. G. A. Bitter, 1963, "A STUDY OF EROSION PHENOMENA 2", *Wear*, Vol. 6, Iss. 3, pp 169-190.
- [17] R. Wellinger, *Z. Metallk.*, 40 (1949) 361.
- [18] P. De Haller, 1939, "Erosion und Kavitations-erosion, in *Handbuch der Werkstoffpvufung*", Vol. 2, edited by E. Siebel, Springer Verlag, pp. 471-488.
- [19] H. Holtey, 1939, *Über den Abnutzungsvorgang in Blasversatzrohren und die Frage der Bekämpfung des Verschleisses*, *Geologie und Mijnbouw*, I, 209.
- [20] J. P. A. TILLET, 1956, "Fracture of glass by spherical indenters", *Proceedings of the Physical Society, Sec B*, Vol. 69, No. 1.
- [21] J. H. Neilson and A. Gilchrist, 1968, "Erosion by a stream of solid particles", *Wear*, Vol.11, Iss. 2, pp 111-122.
- [22] K. Haugen, O. Kvernfold, A. Ronold, R. Sandberg, 1995, "Sand erosion of wear-resistant materials: Erosion in choke valves", *Wear*, Vol 186, pp 179-188.
- [23] Y. Zhang, E.P. Reuterfors, B.S. McLaury, S.A. Shirazi, E.F. Rybicki, 2007, "Comparison of computed and measured particle velocities and erosion in water and air flows", *Wear*, Vol. 263, Iss 1, pp 330-338.
- [24] G. Grant and W. Tabakoff, 1975, "Erosion Prediction in Turbomachinery Resulting from Environmental Solid Particles" *Journal of Aircraft*, Vol. 12, No. 5, pp. 471-478.

- [25] M. F. Hussein and W. Tabakoff., 1977, "Trajectories of particles suspended in fluid flow through cascades", *Journal of Aircraft*, Vol. 8, No. 1, pp. 60-62.
- [26] Katsanis, T. and McNally, 1977, "Revised FORTRAN program for calculating velocities and streamlines on the hub-shroud midchannel stream surface of an axial, radial or mixed flow turbomachine or annular duct", Vols. 1 and 2. NASA TN D8430 and NASA TN D8431.
- [27] MJ Schuh, Humphrey, 1989, "Numerical Calculation of Particle-Laden Gas Flows Past Tubes", *AIChE J.*, 35: 466–480.
- [28] ANSYS Fluent Theory Guide, Release 15.0, 2013.
- [29] Gülich, J. , 2008, "Centrifugal Pumps", Berlin Heidelberg: Springer-Verlag.
- [30] S Krüger, N S Martin, P Dupont, 2010, "Assessment of Wear Erosion in Pump Impellers" 26th International Pump Users Symposium, Houston TX.
- [31] Martin E True, P.D. Weiner, 1976, "A Laboratory Evaluation of Sand Erosion of Oil And Gas", Annual Meeting Papers, Division of Production. American Petroleum Institute.
- [32] S. Pirouzpanah, G. Morrison, 2014, "Predictive Erosion Modeling in an ESP Pump", ASME 2014 4th Joint US-European Fluids Engineering Division Summer Meeting collocated with the ASME 2014 12th International Conference on

Nanochannels, Microchannels, and Minichannels. American Society of Mechanical Engineers.

[33] J.A.C. Humphrey, 1990, "Fundamentals of fluid motion in erosion by solid particle impact", *International Journal of Heat and Fluid Flow* 11.3: 170-195.

[34] A. Hamed, 1982, "Particle dynamics of inlet flow fields with swirling vanes", *Journal of Aircraft* 19.9: 707-712.

[35] Alister Forder, Martin Thewa, David Harrison, 1998, "A Numerical Investigation of Solid Particle Erosion Experienced Within Oilfield Control Valves", *Wear*, 216(2), 184-193.

[36] Zheng D., 2014, "Three Phase Erosion Testing and Vibration Analysis of an Electrical Submersible Pump", Texas A&M University.

[37] Diaz N., 2012, "Effects of Sand on the Components and Performance of Electric Submersible Pumps", Texas A&M University.

[38] Saleh R., 2013, "Experimental Testing of an Electrical Submersible Pump Undergoing Abrasive Slurry Erosion", Texas A&M University.

[39] Minemura, K. and Uchiyama, T., 1990, "Calculation of the Three-Dimensional Behavior of Spherical Solid Particles entrained in a Radial-Flow Impeller Pump", *Proceedings of the Institution of Mechanical Engineers, Part C: Mechanical Engineering Science*, 204(3), 159-168.

[40] Pagalthivarthi, K. V., Gupta, P. K., Tyagi, 2011, “CFD Prediction of Erosion Wear in Centrifugal Slurry Pumps for Dilute Slurry Flows”, *The Journal of Computational Multiphase Flows*, 3(4), 225-245.

[41] Stavros H., Nicolas C., Antonios T., Kristis M., 2009, “An Experimental and Computational Study of the Erosion in Submersible Pumps and the Development of A Methodology for Selecting Appropriate Protective Coatings”, *ASME Turbo Expo: Power for Land, Sea, and Air* (pp. 61-72), American Society of Mechanical Engineers.

[43] S. Reddy, 2016, “Experimental and CFD Simulation of a Helico-Axial Pump”, Texas A&M University.

[44] NDI Measurement Sciences, 3d scanner instruction, [Online]. Available: <http://www.ndigital.com/msci/products/procmm/> [accessed 12 July 2017].

[45] M. Shippen, S. Scott, 2002, “Multiphase Pumping as an Alternative to Conventional Separation, Pumping and Compression”, *PSIG Annual Meeting, Pipeline Simulation Interest Group*.

[46] Hisham A.M., Farooq A.K., Mehmet M.O, 2003, “ESP Failures Analysis and Solutions in Divided Zone-Case Study”, *Middle East Oil Show, Society of Petroleum Engineers*.

[47] R.D. Russell, S.A. Shirazi, J. Macrae, 2004, “A new computational fluid dynamics model to predict flow profiles and erosion rates in downhole completion equipment”,

Proceedings of SPE Annual Technical Conference and Exhibition, Houston, TX, pp.
3723–3749

[48] Lyczkowski, R. and J. Bouillard, 2002, “ State-of-the-art review of erosion modeling
in fluid/solids systems.” *Progress in energy and combustion science* 28(6): 543-602.

APPENDIX A

Diffuser Wear



Figure 127: 1st Diffuser Comparison, Left: New, Right: Eroded



Figure 128: 2nd Diffuser Comparison, Left: New, Right: Eroded



Figure 129: 3rd Diffuser Comparison, Left: New, Right: Eroded



Figure 130: 4th Diffuser Comparison, Left: New, Right: Eroded

APPENDIX B

More details in CFD simulations

Single-Phase Simulations for Performance Maps

k-epsilon Model: Realizable

Near-Wall Treatment: Standard wall function

Spatial discretization

Gradient: Least Square Cell Based

Pressure: Second Order

Density, Momentum, Turbulence Kinetic Energy, Turbulence dissipation rate: First order upwind

Time marching (Transient Formulation): First Order Implicit

Two-Phase Simulations for Testing the GVF

Water-air Drag: schiller-naumann

Water-air: Eulerian-Eulerian

k-epsilon Model: Realizable

Turbulence Multiphase Model: Mixture

Near-Wall Treatment: Standard wall function

Spatial discretization

Gradient: Least Square Cell Based

Pressure: Second Order

Density, Momentum, Volume Fraction, Turbulence Kinetic Energy, Turbulence

dissipation rate: First order upwind

Time marching (Transient Formulation): First Order Implicit

Air density: 4.9kg/m³

Lift: none

Three-Phase Simulations for Erosion Model Calibration

Water-air Drag: schiller-naumann

Water-air: Eulerian-Eulerian

Sand: Discrete Phase Model

Wall Discrete Phase Reflection Coefficients:

Normal

polynomial 4 0.993 -0.0307 0.000475 -2.61e-6

Tangent

polynomial 4 0.988 -0.029 0.000643 -3.56e-6

Lift: none

k-epsilon Model: Realizable

Turbulence Multiphase Model: Per Phase

Standard wall function

Scheme: Phase Coupled SIMPLE

Gradient: Least Square Cell Based

Density, Momentum, Volume Fraction, Turbulence Kinetic Energy, Turbulence

dissipation rate: First order upwind

Time marching (Transient Formulation): First Order Implicit

sand flow rate: 0.133kg/s

density: 2650kg/m³

air density: ideal gas

impeller mesh motion: 3600rpm

air bubble size: 10e-4 m

p-v coupling: Phase coupled SIMPLE

Sand is not added until the two-phase flow field is stabilized. When adding the solid phase, DPM (discrete phase model) has been applied. It takes 2 months for a 40-processor computer to complete the simulation in which the impeller rotates for 3 rounds (1080 degrees). During this time, the particle mass flow is balanced at diffuser inlet and impeller outlet. The tracked particle number is increased from 0 to 30 million, and the file size was increased from 5GB to 20 GB. After that, the flow field could be regarded as stabilized. Then the erosion model can be applied. The simulation should keep going so that the erosion on the impeller would be accumulated by the erosion module. It takes 25 days to move 40 degrees. One reason is that the particles are not moving as fast as water and some of them will stay at the clearance between the impeller tip and its housing, this will make a huge amount of the particles accumulated in the pump.

APPENDIX C

Correction and Modification

The pressure rise of the 1st stage is originally measured by the pressure sensors at the inlet of the 1st impeller and the outlet of the 1st diffuser. This is improper because the inlet suction area of the impeller will make the pressure sensor underestimate the inlet pressure. In addition, after the 100th hour, the wear at the hole for pressure sensor created a hole and caused turbulent flow which will make the pressure sensor overestimate the inlet pressure. Both of them make it necessary to correct the pressure rise of the 1st stage. Finally, the pressure sensor at the bottom tee of the ESP is used as inlet pressure. After this correction, the pressure rise of the 1st stage during the 200 hours is more reasonable (**Figure 131**). After this correction (**Figure 135**), the inlet GVF would be affected. **Figure 132** presents the actually GVF during the 200 hours. The GVF is maintained at 18%-22%, which is acceptable for the 20% GVF erosion test. In **Figure 131**, the pressure rise of the 4th stage increases from the 90th to the 130th hour, which is abnormal compared with other stages. The 4th diffuser is not assembled proximity probes when the torque generated by the fluid on the diffuser is greater than the maximum torque that the friction can provide, the diffuser will rotate. This makes the relative rotating speed of the impeller and diffuser smaller than 3600RPM and reduces the performance of the 4th stage. However, when sand enters the clearance between the diffuser and housing, the friction will increase, as well as the maximum torque. After the

90th hour, the rotating speed of the 4th diffuser decreases which makes the pressure rise increased. The 130th hour seems to be the turning point of the head rise. The head stops increasing which means the diffuser might have been stopped.

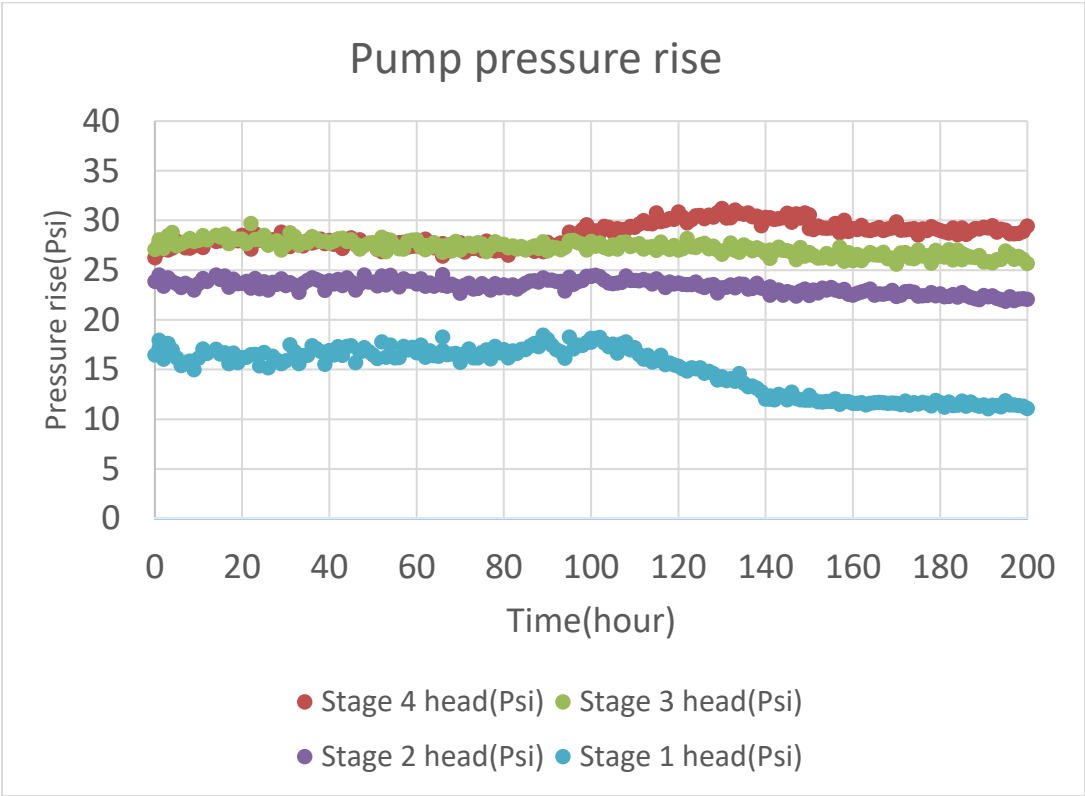


Figure 131: Pressure Rise of Each Stage without Modification or Correction

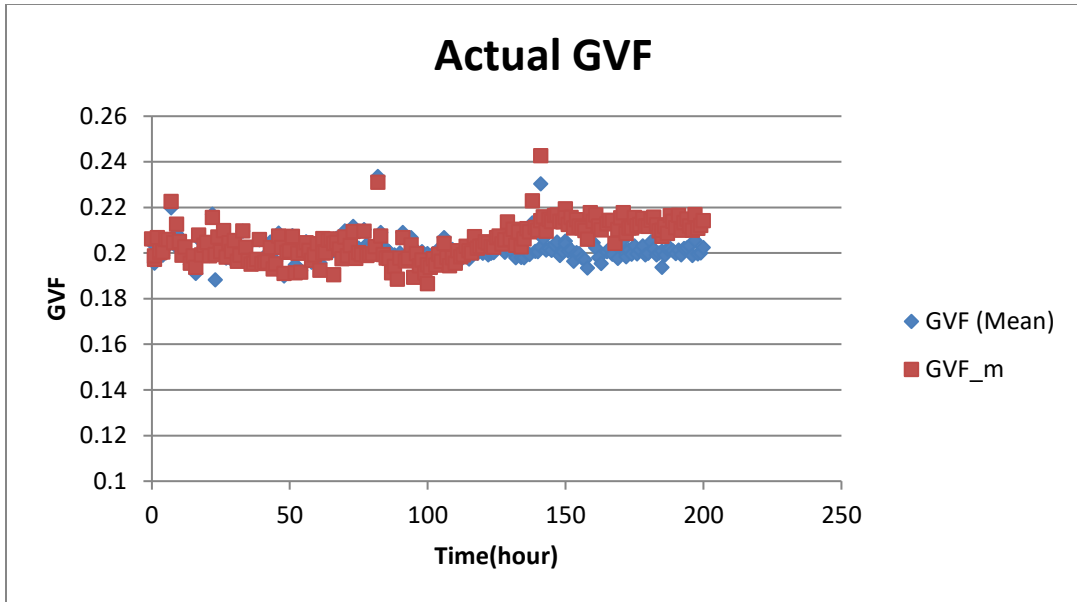


Figure 132: GVF at the Pump Inlet in 200-Hour

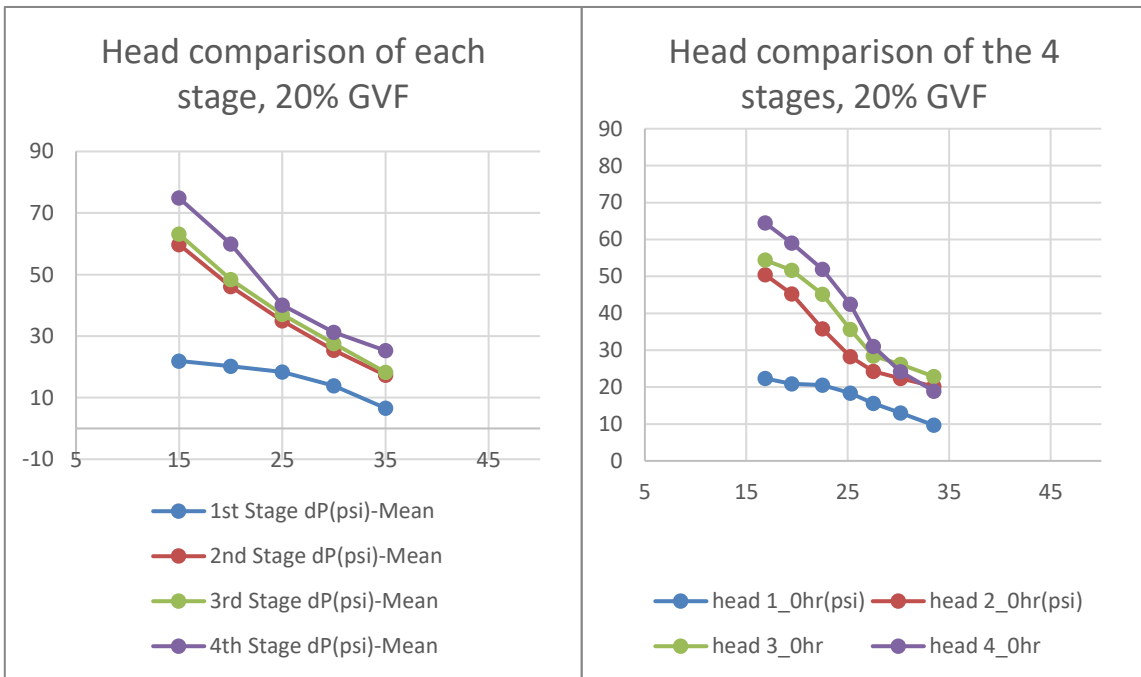


Figure 133: Performance Maps at 20%GVF Inlet (Left: Multi-Phase Test Rig; Right: Erosion Test Rig)

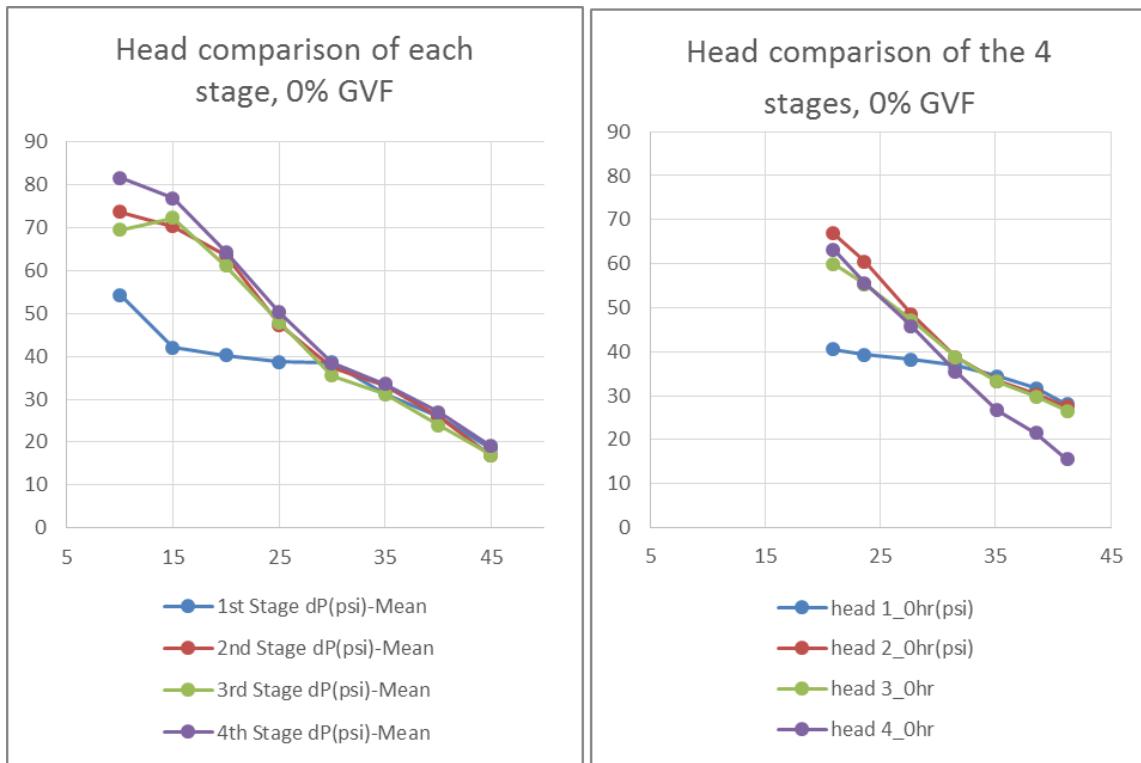


Figure 134: Performance Maps at 0%GVF Inlet (Left: Multi-Phase Test Rig; Right: Erosion Test Rig)

There is a multi-phase test rig which has the same Poseidon ESP installed to test the performance in the turbomachinery laboratory [43]. The performance maps of both ESPs at two test rigs are presented in the left of **Figure 133** and **Figure 134**. With 0% GVF inlet, the 4th stage has unreasonably lower head than the 2nd and 3rd stage. This is because of the bigger moment of momentum carried by higher mass flow rate which makes the diffuser rotating faster. To acquire the reasonable head of the 4th stage, the modification is made by referring to the performance map from the multi-phase test rig. Assuming that before the 140th hour, the head of the diffuser is decreasing linearly with

time; after the 140th hour, the diffuser stops rotating. Equations for this modification are shown below. After the modification, the pressure rise of each stage are shown in **Figure 135**.

$$dp_4^* = (dp_{4,ref} - dp_{3,ref}) + dp_3 - (dp_{3,ref} - dp_{2,ref}) + (dp_3 - dp_2)$$

$$\Delta C_p = \frac{dp_{4,measured,t=140} - dp_{4,t=140}^*}{140}$$

$$dp_4 = \Delta C_p t + dp_4^* \quad \text{for } t < 140$$

$$dp_4 = dp_{4,measured} \quad \text{for } t > 140$$

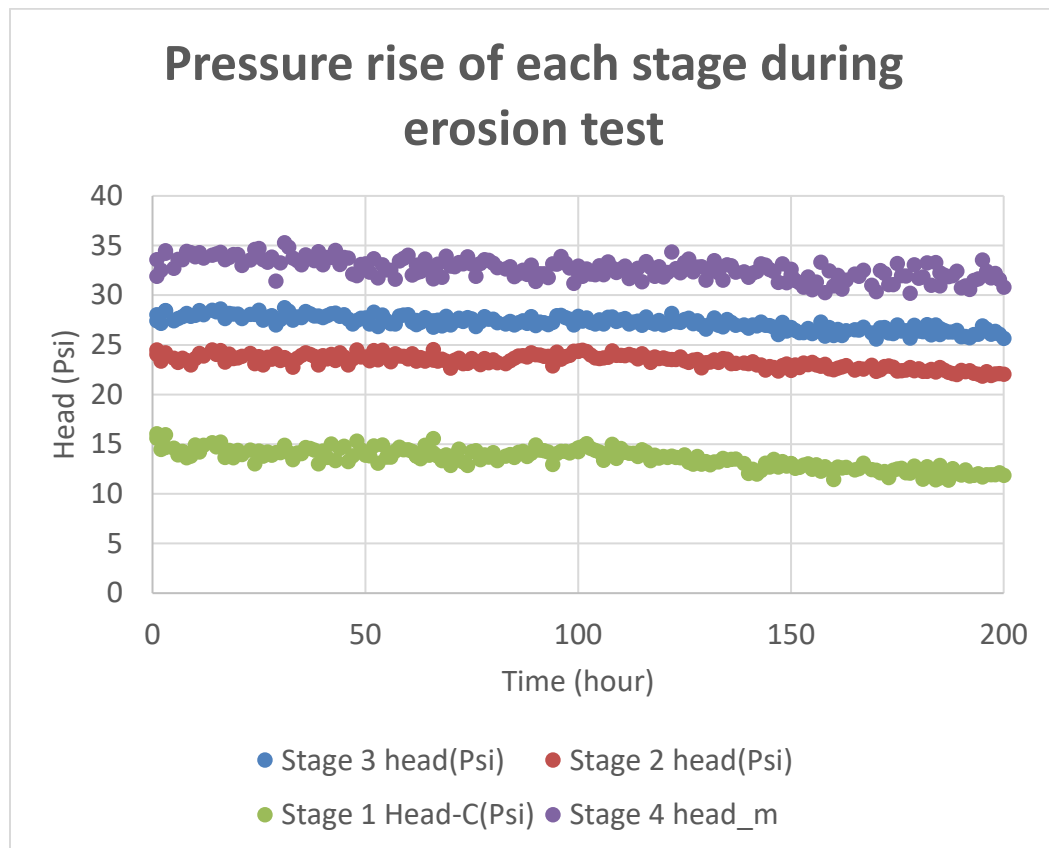


Figure 135: Pressure Rise of Each Stage after Correction and Modification